Thesis for the Degree of Doctor of Philosophy

Medium and High Resolution Spectroscopy in Near-Infrared Bands

Le Nguyen Huynh Anh

School of Space Research

Graduate School

Kyung Hee University

Seoul, Korea

February, 2016

Medium and High Resolution Spectroscopy in Near-Infrared Bands

Le Nguyen Huynh Anh

School of Space Research

Graduate School

Kyung Hee University

Seoul, Korea

February, 2016

Medium and High Resolution Spectroscopy in Near-Infrared Bands

by

Le Nguyen Huynh Anh

Advised by

Dr. Soojong Pak

Submitted to the School of Space Research
and the Faculty of the Graduate School of
Kyung Hee University in partial fulfillment
of the requirements for the degree of
Doctor of Philosophy

Dissertation Committee:

Prof. Soojong Pak, Ph.D. .....

Prof. Myungshin Im, Ph.D. .....

Prof. Jeong-Eun Lee, Ph.D. .....

Prof. Sungsoo Kim, Ph.D. .....

Prof. Young Chol Minh, Ph.D. .....

To my family and my advisor, Prof. Soojong Pak

To all who believe in their dreams

Acknowledgments

Everything is not easy for me to archive what I have now. Astronomy gives me a guideline to live, but it also brings challenges to me. When I was young, I have to work in early morning everyday to help my family. Thanks to those working days in early morning, I was fallen in love with astronomy. Looking the stars in the early morning in the countryside was marvellous for me. Stars have miraculous beauty, and make people want to understand and touch them.

At that time, The universities in Viet Nam do not have astronomy major. And, I decided to choose Physics to study. During that time, I always wished to study astronomy and come to the observatory to look at the stars. I was lucky to come to Korea. Prof. Soojong Pak gave me a chance to study astronomy. My life has changed to a new page when I came here. Studying in here was difficult for me at the first time. I have to start from the beginning to learn everything.

I deeply appreciate and thank Prof. Soojong Pak for all the helps. He is always sympathetic and generous in teaching me when I do not know how to do and have difficulties in my works. Without his encouragements and helps, I would not become what I am now.

I thank my parents, my brother, and my sister who always encourage and support my life. I also thank my best friend, Dung Pooh for all the helps during the time I study in here.

Finally, I realize that we can make our dreams come true if we believe in them. It is not easy to do what we wish to do. Sometimes, life is so hard to overcome. But, we can do if we still have "hopes". Marie Curie says that: "Life is not easy for each of us. But, we have to believe in ourself. We have to believe that we have ability in something and try to do it. Maybe, everything will be easy and progress well when we do not expect."

Medium and High Resolution Spectroscopy in Near-Infrared Bands

by

Le Nguyen Huynh Anh

Submitted to the School of Space Research
on – –, 2016, in partial fulfillment of the
requirements for the degree of
Doctor of Philosophy

Abstract

In this thesis, I present the studies of medium and high resolution spectroscopy in near-infrared (NIR) bands. In the first chapter of this thesis, I present the methods of calculating signal and noise of an NIR spectrograph. We have developed sensitivity simulation methods to measure signal and noise of IGRINS, exposure-time calculator (ETC). The ETC produces the expected signal-to-noise ratio (S/N) for each resolution element, given the exposure-time and number of exposures. IGRINS ETC is a useful tool for calculating expected S/N of the emission features. Next, by using medium resolution spectra (R $\sim$ 5000) in H band, obtained by IRCS (Infrared Camera and Spectrograph) at the Subaru telescope, I study the central region of quasars, PG $0844+349$ (z=0.064), PG $1226+023$ (z=0.158), and PG $1426+015$ (z=0.086). Based on the advantages of using adaptive optics technology, the quasar spectra can be isolated from the host galaxy spectra. The obtained spectra with medium resolution can be used to determine the stellar velocity dispersions in the bulge of the host galaxies, and to estimate the supermassive black hole masses (SMBH). By using an $M_{BH}-\sigma$ relation of elliptical galaxies, I derived the black hole (BH) masses of the quasars. Understanding the link between the supermassive black holes and their host galaxies is important to study the formation and evolution of the galaxies. In recent years, basing on the development of new instruments in Infrared bands, we have more advantages to study astronomy with higher resolution spectroscopy. IGRINS (Immersion Grating Infrared Spectrograph) is a high resolution spectrograph which has high resolving power, R $\sim$ 40,000. By using the high resolution spectroscopy, we can look into the spectra of the objects in detail and improve the understanding of the physical conditions of the targets. In this thesis, I also present the study of photodissociation regions (PDRs) by using high resolution spectra of the reflection nebulae, NGC 7023 which observed by IGRINS. We detect plentiful of H_2 emission lines in H and K bands. From the huge numbers of the observed emission lines, we can improve the understanding of the emission features of NGC 7023 in details, and figure out what the emission features can tell us. From the relative line strengths of the emission lines, I study the excitation mechanisms of molecular hydrogen H_2. We find the different distributions of density profile in the observed region within the slit-length of $15''$. The estimate ortho-to-para ratio (OPR)

indicates that the H_2 emission in the observed regions arises from UV fluorescence. We derive the hydrogen density of $\sim 10^4$ cm^{-3} by comparing the line ratio 2-1 S(1)/1-0 S(1) with that of Sternberg & Dalgarno (1989) model. Through the best-fits of observed line ratios to that Draine & Bertoldi (1996), we find the variations of density distribution in the observed regions. This results suggest that the observed regions has clumpy structure which high density clump $\sim 10^5$ cm^{-3} embedded in lower density regions, 10^3–10^4cm^{-3}. The estimate size of a clump may be ~ 0.01 pc.

Thesis Supervisor: Soojong Pak
Title: Professor

Contents

List of Figures

List of Tables

Chapter 1

Introduction

1.1 Background and Motivations

Since the discovery of infrared (IR) light by William Herschel in 1800, IR observations lead evolutions in astronomical history. By using observations in IR bands, astronomers discover information outside of the visible wavelength ranges. IR radiate in wavelengths of $0.75-300$ μm which divided into three regions as the near IR ($0.65-5.0$ μm), the mid-IR (7.5-25 μm), and the far-IR (28-450 μm). IR spectroscopy is a useful tool that astronomers utilize to explore the universe because IR observations are critical in the study of astronomical objects which are hidden in dense regions such as the star-formation regions and black holes in the central galaxies.

In recent years, the developments of IR spectrographs are important in the revolutions of astronomy. In ground based telescope, the high resolution spectrographs have been made such as IGRINS (Immersion Grating Infrared Spectrograph) in McDonald observatory and iSHELL, a high-resolution echelle spectrograph on IRTF (Infrared telescope Facility). The new developments of IR missions such as SOFIA (the stratospheric Observatory for Infrared Astronomy) and SIRTF (the Space Infrared Telescope Facility) are promising in the improvements of IR observations. The future spectrograph GMTNIRS (The Giant Magellan Telescope Near Infrared Spectrograph) will open a new horizon in

history of IR astronomy.

Through the important roles of IR observations, the preparation package of observations such as exposure time calculator (ETC) are necessary to the developments of an IR spectrometer. The ETC allows observers to calculate the expected signal and noise of the observed spectra. The sensitivities of an IR spectrograph are displayed through the ETC. In this thesis, I present the methods to calculate signal and noise of IGRINS.

IR spectroscopy gives us unique probes to clarify the central region of galaxies and the star-formation regions, which are hidden in optical observations. Nowadays, we believe that galaxies with bulges have supermassive black holes (SMBH) at the center. The bugles and BH correlate each other and evolve together. The BH masses correlate with the stellar mass and the stellar velocity dispersion of the bulges of their host galaxies. By studying the dynamics of the stars in the host bulges, we are able to estimate the BH masses (Ferrarese, Pogge, & Peterson et al., 2001; Gebhardt, Kormendy & Ho et al., 2000). This study is important to understand the BH growth.

Stars have their own story of formation and activity. By the process of gravitational collapses at free-fall time, stars are formed in cold and dense molecular gas (Evens, 1999; Kennicutt & Evans, 2012). The measurements of molecular mass are significant in the study of star-formation efficiency. The calculations of critical values of Jeans mass, considering a cloud with only thermal support, M_J and magnetic critical mass, in view of effects from magnetic field and turbulence, M_B (Li & Shu, 1996) allow us to know when and how a star will form with a time scale. To understand the process of how molecular gas collapse to form a star, the study of physical conditions in star-forming regions are very important. By integrating the column density over an area, we can measure the cloud mass within the zone. Another common method is the virial theorem, cloud mass can be estimated from the line-width (Telesco, 1988). The study of ultraviolet (UV) radiation from young hot stars are also crucial. The physical and chemical states of molecular clouds

are affected by the interaction of UV radiation and the neutral interstellar medium (ISM).

Both of the BH growth and star-formation activity play important roles in galaxy formation and evolution. The relations between the star-formation activity and the BH growth in the central region of the galaxies have been studied (Hopkins & Quataert, 2010). From the derivations of BH masses and star formation rates (SFR), Alonso-Herrero et al. (2013) determines the ratios between SFR and the BH accretion rate (BHAR) in local luminosity infrared galaxies (LIRGs). The study of the BH growth in the central region of the galaxies and the star-formation process are important in understanding galaxy evolutions.

In this thesis, I present the study of measuring the stellar velocity dispersion of the host galaxies of nearby quasars. From the measured velocity dispersions, I estimate the BH masses of the quasars. I also study the physical conditions in the photodissociation region of the reflection nebulae NGC 7023 by using ro-vibrational H_2 emission lines. The study of both subjects are important in the understanding of the BH growth and star-formation process which are useful to investigate galaxy evolutions.

1.2 Sensitivity Estimation for Instrumentations and Observations

Exposure-time calculators (ETCs) play an important role in preparing for observations by accurately simulating the expected exposure-time to achieve a required signal-to-noise ratio (S/N). In this thesis, we developed the IGRINS ETC by taking into account the telluric background emission and absorption, the thermal emission and throughput of the telescope and instrument optics, and the dark current and read noise of the infrared detector arrays (Le et al., 2015). This tool is a part of the IGRINS software which includes the IGRINS data reduction pipeline package (Sim et al., 2014). The software was written in the interactive data language Python, and the user controls specific calculation modes

and input parameters via a graphical user interface. In this paper, we present detailed calculation algorithms and the results of the IGRINS ETC. This chapter would be an interesting reference for anyone who want to study this topic.

1.3 Black Holes and Galaxies Evolutions

Understanding the link between the supermassive black holes and their host galaxies is important in studying the formation and evolution of the galaxies. We believe that nearby galaxies have bulges with supermassive black holes (SMBHs), are remnants of the cosmic evolution of distant quasars (Richstone, 1998). However, the measurement of SMBHs is difficult to measure directly (Ho, 1999; Ho & Kormendy, 2000). One of the method is reverberation mapping to estimate the virial masses, but in this method, we do not know the systematic errors (Kaspi, Smith et al., 2000; Krolik, 2001).

The relation of $M_{BH}-\sigma$ has been discovered, in which M_{BH} is the mass of supermassive black hole and σ is the stellar velocity dispersion of the bugle (e.g., Ferrarese, Pogge, & Peterson et al., 2001; Gebhardt, Kormendy & Ho et al., 2000; Gebhardt, Bender & Bower et al., 2000). So, by measuring the σ is the stellar velocity dispersion of the bugle, we can estimate the mass of SMBHs M_{BH} simply. However, the measurements of stellar velocity dispersion of the bugle of host galaxies are difficult in optical bands because the absorption lines such as Mg b at 517 nm and Ca triplet at 850 nm are diluted by continuum (Boroson & Green, 1992). Therefore, it is necessary to use stellar lines in other wavebands to measure velocity dispersion. NIR stellar lines have the potential of explaining for the relation between supermassive back holes and their host galaxies. CO bandheads in near-infrared (NIR) have been suggested to be the best way in studying the velocity dispersion of nearby galaxies (McConnell, 2011).

In this thesis, by using NIR medium resolution spectra of nearby quasars, PG $0844+349$, PG $1226+023$, and PG $1426+015$, I measure the velocity dispersion of the host

galaxies by using the relation of $M_{BH}-\sigma$ to estimate the black hole masses of the quasars.

1.4 Star Forming Regions

Photodissociation regions or photon-dominated regions (PDRs) are the transition layers between the ionized gases and the surface of molecular clouds. PDR is created in a region, where the far-UV (FUV) photons (6 eV $\leqslant h\nu \leqslant$ 13.6 eV) illuminate a surface layer of a molecular cloud. In that layer, FUV photons directly excite atoms and molecules, then significantly contribute to the physical conditions of the region such as ionization heating, chemistry, structure, and temperature (e.g., Tielens & Hollenbach, 1985a; Tielens & Hollenbach, 1985b; Black & van Dishoeck, 1987; Sternberg & Dalgarno, 1989; Burton et al., 1989; Draine & Bertoldi, 1996; Luhman et al., 1997; Hollenbach & Tielens, 1999). The penetration of the UV radiation depends on the dust absorption and scattering. The geometry and structure of the molecular cloud also affect the UV infiltration. From the surface of the cloud, at $A_V < 1$ mag, UV fluxes are absorbed by C atom and dust. Gas temperature is larger than dust temperature. When $A_V \sim 1-2$ mag, H^+/H transition layer happens. H^+ becomes H_2 at $A_V = 2$ mag. At $A_V = 4$ mag, C^+ becomes C and CO. At $A_V \sim 5 - 10$ mag, O atom is formed, and converted to O_2 (Tielens & Hollenbach, 1985a,b).

Molecular hydrogen H_2 are the major component in the ISM. They are important to trace the physical conditions of the star-formation processes in molecular clouds. In PDRs, H_2 absorb FUV photons, raising the H_2 from ground electronic state $X_1\Sigma_g^+$ to excited electronic states $B^1\Sigma_u^+$ Lyman and $C^1\Pi_u$ Werner bands. About 15% of the excited molecules will be dissociated and $\sim$ 85% of the excited molecules decay back to some ro-vibration levels of the ground electronic state, following by fluorescent emission as it cascades back to the ground vibrational state. The relative intensity of H_2 from UV excitations is sensitive to the density and the UV field strength (Black & van Dishoeck,

1987). In high density regions ($n_{H_2} > 5 \times 10^4$ cm^{-3}), the gas density is high enough to create collisional de-excitation of the UV excited gas, and heat the region to temperature of 1000 K (e.g., Sternberg & Dalgarno, 1989; Draine & Bertoldi, 1996; Luhman et al., 1997). H_2 are powerful to trace the physical conditions of PDRs such as the densities, the incident UV radiation field strengths, and the excitation mechanisms (Draine & Bertoldi, 1996 ; Luhman & Rieke, 1996).

By using IGRINS to obtain the high resolution spectra of northern filament of NGC 7023, one of the popular PDR, I probe the excitation mechanism of H_2 and study the physical conditions in this region. The study of physical conditions is important to explore the star-formation process in the PDRs and in the interstellar medium (ISM).

1.5 Organization of This Thesis

Chapter 1 (Le et al., 2015) presents the exposure-time calculator of IGRINS. We develop the IGRINS ETC to generate realistic simulations of both continuum and emission line sources. The signal and noise values are estimated by taking into account telluric background emission and absorption, the emission and transmission of the telescope and instrument optics, and the dark current and read noise of the infrared detector arrays. We estimate the atmospheric transmission using models that account for the amount of precipitable water vapor (PWV) along the line of sight to the target. From the ETC, the observers can estimate the S/N of the spectrum for each spectral resolution element given the exposure-time and number of exposures. The source-code of the IGRINS ETC version 3.10 is available to be downloaded from the website http://irlab.khu.ac.kr/∼igrins.

In chapter 2 (Le et al., 2014), I present NIR medium resolution host galaxy spectra of nearby quasars, PG $0844 + 349$, PG $1226 + 023$, and PG $1426 + 015$ in H-band, observed by the IRCS instrument and the AO of the Subaru telescope. The data analysis method of the NIR spectra is presented. The techniques of data analysis can also be seen in (Le,

Kang, & Pak et al., 2011). I derived the stellar velocity dispersion of the host galaxy. From the identified stellar absorption lines, we have obtained the velocity dispersion of PG 1426+015 to be 264 ± 215 km s^{-1} based on the measurement of Mg I (1.503 μm) and Si I (1.589 μm). In the case of PG 0844 + 349, we have measured the velocity dispersion of the host galaxy to be 132 ± 110 km s^{-1} based on the calculation of CO (6-3) (1.619 μm). By using an $M_{BH}-\sigma$ relation of elliptical galaxies, the BH masses of PG 0844 + 349 and PG 1426 + 015 are estimated to be $log(M_{BH}/M_{\odot}) = 7.7 \pm 5.5$ and $log(M_{BH}/M_{\odot}) = 9.0 \pm 7.5$, respectively. These values are consistent with the BH masses from the quasar broad emission lines.

In chapter 3 (Le et al., 2016, in preparation), I present high-resolution spectra of near-infrared H_2 emission lines from the northern filament of the reflection nebulae, NGC 7023, observed by IGRINS. We observed the region within the slit-length of $15''$. The observed region has been divided into three regions. We calculated the ortho-to-para ratios (OPR) of three regions. The values of OPR are 1.57−1.62, indicate that the observed H_2 emissions are mostly excited by UV photons. We derive the hydrogen density and find the variation of density distribution in the regions. Region A has high density of $\sim 10^5$ cm^{-3}. And, the densities of regions B and C are $10^3-10^4 cm^{-3}$. This results suggest that the observed region has clumpy structure. The variation of density within small scale structure has significant connection to the star-formation process, and indicate the local turbulence in the region.

Bibliography

Alonso-Herrero, A., Pereira-Santaella, M., Rieke, G. H., et al. 2013, ApJ, 765, 78

Black, J. H., & Van Dishoeck, E. F. 1987, Flourescent Excitation of Interstellar H_2, ApJ, 322, 412

Burton, M. G., Brand, P. W. J. L., Geballe, T. R., & Webster, A. S. 1989, MNRAS, 236, 409

Boroson, T. A., & Green, R. F., 1992, ApJS, 80, 109

Draine, B. T. & Bertoldi, F. 1996, ApJ, 468, 269

Ferrarese, L., Pogge, R. W., Peterson, B. M., Merritt, D., Wandel, A., & Joseph, C. L. 2001, Supermassive Black Holes in Active Galactic Nuclei. I. The Consistency of Black Hole Masses in Quiescent and Active Galaxies, ApJ, 555, L79

Gebhardt, K., Kormendy, J., & Ho, L. C., et al. 2000, A Relationship between Nuclear Black Hole Mass and Galaxy Velocity Dispersion, ApJL, 539, L13

Gebhardt, K., Bender, R., & Bower, G., et al. 2000, Black Hole Mass Estimates from Reverberation Mapping and from Spatially Resolved Kinematics, ApJL, 543, L5

Ho, L. C. 1999, In Observational Evidence for Black Holes in the Universe, ed. S. K. Chakrabarti (Dordrecht: Kluwer)

Ho, L. C., & Kormendy, J. 2000, in The Encyclopedia of Astronomy and Astrophysics, (Institute of Physics Publishing)

Hollenbach, D. J., & Tielens, A. G. G. M. 1999, Rev. Mod. Phys., 71, 173

Hopkins, P. F., & Quataert, E. 2010, MNRAS, 407, 1529

Jeans, J. H. 1928, Astronomy and Cosmology (UK: Cambridge Univ. Press)

Kaspi, S., Smith, P. S., Netzer, H., Maoz, D., Jannuzi, B. T., & Giveon, U. 2000, Reverberation Measurements for 17 Quasars and the Size-Mass-Luminosity Relations in Active Galactic Nuclei, ApJ, 533, 631

Kennicutt, R. C. Jr., & Evans II N. J. 2012, ARA&A, 50, 531

Krolik, J. H. 2001, Systematic Errors in the Estimation of Black Hole Masses by Reverberation Mapping, ApJ, 551, 72

Le, H. A. N., Kang, W., Pak, S., Im, M. et al. 2011, Medium Resolution Spectral Library of Late-Type Stellar Templates in Near-Infrared Band, JKAS, 44, 125

Le, H. A. N., Pak, S., Im, M., Kim, M., Sim, C. K., & Ho, L. C. 2014, Medium Resolution Near-Infrared Spectra of the Host Galaxies of Nearby Quasars, JASR, 54, 6

Le, H. A. N., Pak, S., Jaffe, D. T. et al. 2015, JASR, 55, 11

Le, H. A. N., Pak, S., Jaffe, D. T. et al. 2016, High-Resolution Spectroscopy of NGC 7023, in preparation.

Li, Z. Y. & Shu, F. H. 1996, ApJ, 472, 211

Luhman, K. L. & Rieke, G. H. 1996, ApJ, 461, 298

Luhman, M. L., Jaffe, D. T., Sternberg, A., Herrmann, F., & Poglitsch, A. 1997, ApJ, 482, 298

Martini, P., Sellgren, K., & Hora, J. L. 1997, ApJ, 484, 296

Martini, P., Sellgren, K. & Depoy D. L. 1999, ApJ, 526, 772

McConnell, N. J., et al. 2011, The Black Hole Mass in Brightest Cluster Galaxy NGC 6086, AJ, 728, 100

Richstone, D., et al. 1998, Supermassive Black Holes Then and Now, Nature, 395, A14

Sim, C. K., Le, H. A. N., Pak, S. et al. 2014, Comprehensive data reduction package for the Immersion GRating INfrared Spectrograph: IGRINS, JASR, 53, 11

Sternberg, A. & Dalgarno, A. 1989, ApJ, 338, 197

Telesco, C. M. 1988, ARA&A, 26, 343

Tielens, A. G. G. M., & Hollenbach, D. J. 1985a, ApJ, 291, 772

Tielens, A. G. G. M., & Hollenbach, D. J. 1985b, ApJ, 291, 747

Chapter 2

Exposure Time Calculator for Immersion Grating Infrared Spectrograph: IGRINS[1]

2.1 Abstract

We present an exposure-time calculator (ETC) for the Immersion Grating Infrared Spectrograph (IGRINS). The signal and noise values are calculated by taking into account the telluric background emission and absorption, the emission and transmission of the telescope and instrument optics, and the dark current and read noise of the infrared detector arrays. For the atmospheric transmission, we apply models based on the amount of precipitable water vapor along the line of sight to the target. The ETC produces the expected signal-to-noise ratio (S/N) for each resolution element, given the exposure-time and number of exposures. In this paper, we compare the simulated continuum S/N for the

[1]This work has been published in Advances in Space Research (Le, H. A. N., et al. 2015, JASR, 55, 11).

early-type star HD 124683 and the late-type star GSS 32, and the simulated emission line S/N for the H_2 rovibrational transitions from the Iris Nebula NGC 7023 with the observed IGRINS spectra. The simulated S/N from the ETC is overestimated by 40−50% for the sample continuum targets.

2.2 Introduction

The Immersion Grating Infrared Spectrograph (IGRINS) is a cross dispersed near-infrared spectrograph designed using silicon immersion echelle grating (e.g., Marsh, Mar & Jaffe, 2007; Wang, Gully-Santiago & Deen et al., 2010; Gully-Santiago, Wang & Deen et al., 2012). This instrument can cover the whole H and K bands ($1.4 - 2.5$ μm) in single exposure with a resolving power of $R = 40{,}000$. Two volume phase holographic (VPH) gratings are used as cross-dispersing elements in the H and K bands. IGRINS employed two 2048×2048 pixel Teledyne Scientific & Imaging HAWAII-2RG detectors with SIDECAR ASIC cryogenic controllers. Figure 1 shows the optical design sketch of IGRINS. This instrument has been employed on the 2.7 m Harlan J. Smith Telescope at the McDonald Observatory since 2014 March. Detailed descriptions of IGRINS can be found in Yuk et al. (2010) and Park et al. (2014).

Exposure-time calculators (ETCs) play an important role in preparing for observations by accurately simulating the expected exposure-time to achieve a required signal-to-noise ratio (S/N). Examples of ETCs include those for MOSFIRE[2], CRIRES[2], SOFI[2], KMOS[3], HSpot[4], and the Wide Field Planetary Camera 2 (WFPC2) of the Hubble Space Telescope (e.g., Bernstein et al., 2002; Li Causi, De Marchi & Paresce, 2002).

We developed the IGRINS ETC by taking into account the telluric background emission and absorption, the thermal emission and throughput of the telescope and instrument

[2]http://www2.keck.hawaii.edu/inst/mosfire/etc.html.

[3]See the ESO exposure-time calculators at http://www.eso.org/observing/etc.

[4]http://herschel.asdc.asi.it/index.php?page=proposal.html.

optics, and the dark current and read noise of the infrared detector arrays. This tool is a part of the IGRINS software which includes the IGRINS data reduction pipeline package (Sim et al., 2014). The software was written in the interactive data language Python, and the user controls specific calculation modes and input parameters via a graphical user interface. In this paper, we present detailed calculation algorithms and the results of the IGRINS ETC.

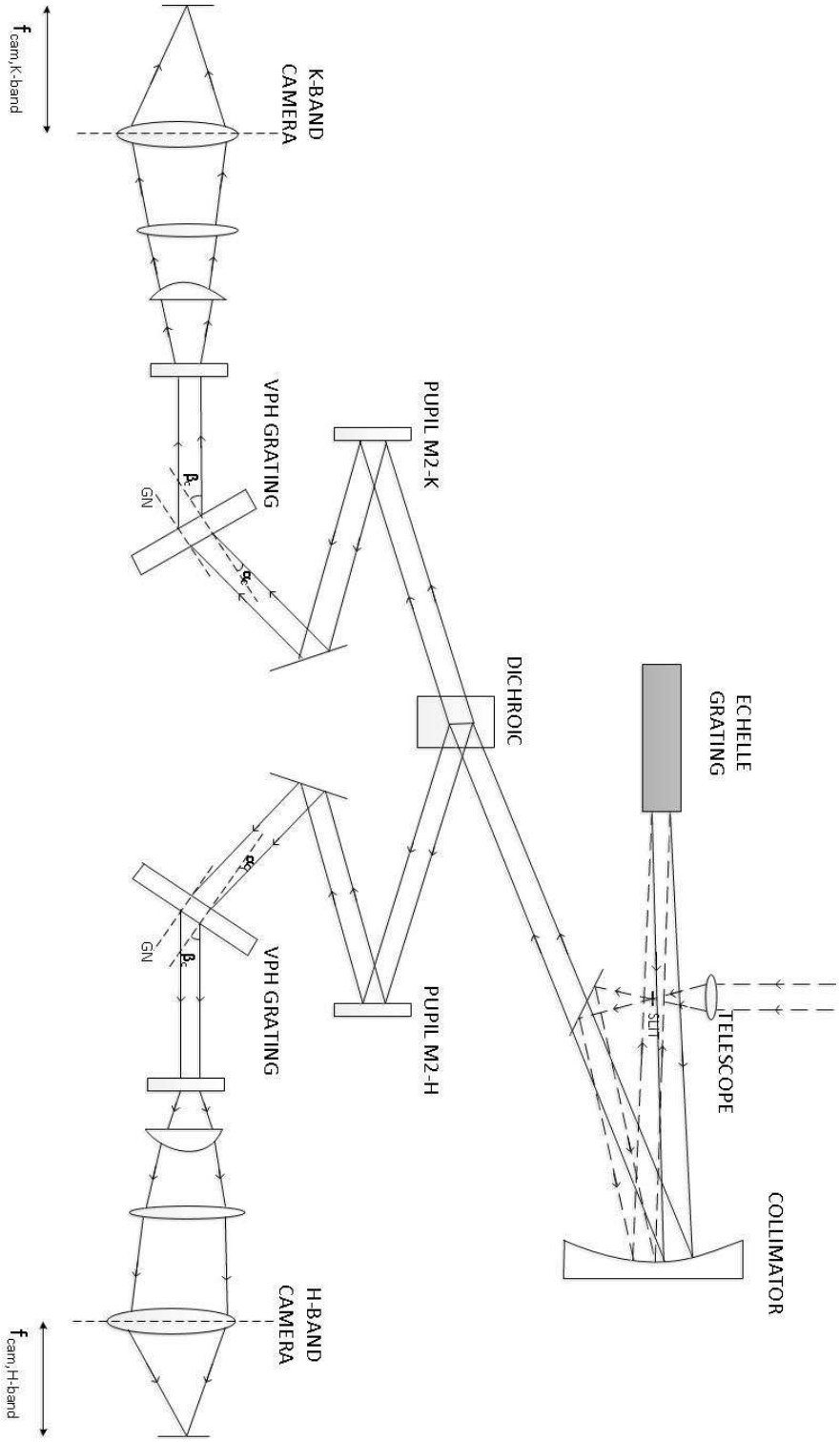

Fig. 1: IGRINS optical design sketch.

2.3 Sensitivity Simulation Methods

2.3.1 Throughput

We define the total throughput, $\tau_{\rm point}$ for point sources as

$$\tau_{\rm point} = \tau_{\rm atmo}\tau_{\rm mirror}\tau_{\rm gr}\tau_{\rm vph}\tau_{\rm optics}\tau_{\rm slit}\tau_{\rm qe} \tag{2.1}$$

$$\tau_{\rm extend} = \tau_{\rm atmo}\tau_{\rm mirror}\tau_{\rm gr}\tau_{\rm vph}\tau_{\rm optics}\tau_{\rm qe} \tag{2.2}$$

where τ terms are the throughput values of the average atmosphere ($\tau_{\rm atmo}$), telescope mirrors ($\tau_{\rm mirror}$), immersion grating ($\tau_{\rm gr}$), VPH gratings ($\tau_{\rm vph}$), other IGRINS optics ($\tau_{\rm optics}$), slit ($\tau_{\rm slit}$), and detector ($\tau_{\rm qe}$). Table 1 shows the estimated values of these parameters in equations (4.2) and (2.2). We estimate that the average throughput value of the atmosphere is 0.77 and 0.83, assuming that the precipitable water vapor (PWV) is 4 mm, at the wavelength ranges of 1.4−1.9 μm and 1.9−2.5 μm for the H and K bands, respectively. The model of the atmosphere transmission is shown in Appendix A. Since the point spread function (PSF) on the slit closely resembles a Gaussian, we can easily estimate the slit loss for a given image size. We define a slit throughput, $\tau_{\rm slit}$, as

$$\tau_{\rm slit} = \frac{F_{\rm slit}}{F_{\circ}} \tag{2.3}$$

where $F_{\circ}$ is the unobscured flux from the target, and $F_{\rm slit}$ is the flux passing through the slit (Lee & Pak, 2006). If the PSF is a circularly symmetric Gaussian function, $\tau_{\rm slit}$ can be expressed as the error function:

$$\tau_{\rm slit} = \frac{1}{\sqrt{2\pi}\sigma}\int_{-Y}^{+Y} \exp\left[-\frac{y^2}{2\sigma^2}\right] dy \tag{2.4}$$

where Y is a half of the slit width and σ is a Gaussian width, i.e., $\sigma = \Delta y_{\rm FWHM}$ / $(2\sqrt{2\ln 2})$, where $\Delta y_{\rm FWHM}$ is the measured full width at half maximum along the slit

length.

Table 1: Parameters in throughput estimation

τ	Parameter	Value
$\tau_{\rm atmo}$	Atmosphere[a] (H band)	0.77
$\tau_{\rm atmo}$	Atmosphere[a] (K band)	0.83
$\tau_{\rm mirror}$	Telescope Mirrors	0.55
$\tau_{\rm gr}$	Immersion Grating	0.88
$\tau_{\rm vph}$	VPH Grating (H band)	0.80
$\tau_{\rm vph}$	VPH Grating (K band)	0.75
$\tau_{\rm optics}$	Other IGRINS Optics[b]	0.42
$\tau_{\rm slit}$	Slit-Loss[a]	0.64
$\tau_{\rm qe}$	Q.E. of Detector	0.80

[a] See section 2.1.

[b] Window, a pupil stop, collimators, and camera lenses.

2.3.2 Background Emissions

We calculate the background emissions from the Zodiacal light, the Moon light, OH emission lines, and thermal emission from the atmosphere. Table 2 shows the parameters used in the calculations. The number of electrons s^{-1} $pixel^{-1}$ by the background emissions is given by

$$\varepsilon_{\rm Zod,Moon,OH} = A\Omega\tau_{\rm extend}\frac{\lambda_\circ}{\Delta\lambda_{\rm BW}R}\left(\Phi_{\rm Zod}+\Phi_{\rm Moon}+0.1\Phi_{\rm OH}\right) \tag{2.5}$$

where $\tau_{\rm extend}$ is the total throughput for an extended source, R is the spectral resolution (R = 40,000) for IGRINS, $\lambda_\circ$ is the central wavelength of the H or K filter, $\Delta\lambda_{\rm BW}$ is the band width of the filter, $\Phi_{\rm Zod}$, $\Phi_{\rm Moon}$, and $\Phi_{\rm OH}$ are photon fluxes from the Zodiacal scattered light, the Moon light, and OH airglow in units of photon s^{-1} m^{-2} $arcsec^{-2}$, $A\Omega$ is the aperture of the telescope multiplied by the solid angle on the sky viewed by one pixel ($A\Omega = 1.00\times10^{-11}$ m^2 sr $pixel^{-1}$).

In Table 2, we list the average values of the Zodiacal light[5] at ecliptic latitudes of 0°, 30°, 60°, and 90°. In the simulation, we assume the heliocentric ecliptic longitudes at ±90° since the Zodiacal light is not variable at different ecliptic longitudes. In the ETC, the average values of the Zodiacal light is $\Phi_{\rm Zod}$ = 55, 41 photon s^{-1} m^{-2} $arcsec^{-2}$ for H and K bands, respectively.

[5]See the Sky Model Calculator at http://www.eso.org/observing/etc.

Table 2: Parameters in sensitivity simulations

Parameter	H band	K band	Unit
Center Wavelength	1.63	2.22	μm
Zodiacal Light[a] at latitude of 0°	99	73	photon s^{-1} m^{-2} $arcsec^{-2}$
Zodiacal Light[a] at latitude of 30°	50	37	photon s^{-1} m^{-2} $arcsec^{-2}$
Zodiacal Light[a] at latitude of 60°	42	31	photon s^{-1} m^{-2} $arcsec^{-2}$
Zodiacal Light[a] at latitude of 90°	30	22	photon s^{-1} m^{-2} $arcsec^{-2}$
Half Moon light[b]	54	30	photon s^{-1} m^{-2} $arcsec^{-2}$
Full Moon light[b]	595	277	photon s^{-1} m^{-2} $arcsec^{-2}$
OH light[c]	3390	1096	photon s^{-1} m^{-2} $arcsec^{-2}$
Ambient Temperature	275	275	K
Detector Read Noise	5	5	electron
Detector Dark Current	0.02	0.02	electron s^{-1}

[a] See section 2.2. We assume the heliocentric ecliptic longitude is ±90°.

[b] See section 2.2. We assume the separation between target and Moon is 60°, and the altitude of the Moon is 45°.

[c] See section 2.2. The OH value use in equation (2.5) is total OH line intensity in H and K bands.

The Moon light is another natural source that is the major contributor to the sky background (e.g., Noll, Kausch & Barden et al., 2012; Jones, Noll & Kausch et al., 2013). We calculate the average values of the Moon light[4] at the Moon phases of the half Moon and the full Moon for the cases of the Moon and target separations at 0°, 30°, 60°, 90°, and 120° (See Figure 2). In the ETC, we assume that the target separation is 60° for the cases of the half Moon and the full Moon phases. We may consider to apply for all the cases of the Moon light in the next versions of the ETC.

We calculate the $\Phi_{\rm OH}$ value based on OH emission lines which are shown in Figure 11 in Appendix A. We sum up the OH line intensity values of whole band. The OH value, used in equation (2.5) is the summation of OH line intensity in H and K bands, $\Phi_{\rm OH}$ = 3390 + 1096 = 4486 photon s^{-1} m^{-2} arcsec^{-2}. We also consider that these is ratio of photons from OH lines that are scattered inside the IGRINS optical box and distributed as scattered light across the detector. By using Flat image which is subtracted by Dark image (See Figure 3), we calculate the average intensity of pixel values in the order regions, and the inter-order regions, then estimate the scattering ratio of photon from OH lines inside the optics (See Table 3). The calculated ratio value is 0.1 for both H and K bands.

The background thermal flux in units of electrons s^{-1} pixel^{-1} is calculated by

$$\varepsilon_{\rm thermal} = A\Omega\varepsilon\frac{B_{\nu,T}}{hR} \tag{2.6}$$

where h is the Planck constant, and $B_{\nu,T}$ is the Planck function of frequency ν and temperature T in units of W m^{-2} Hz^{-1} sr^{-1}. We define the total emissivity ε as

$$\varepsilon = \frac{(1-\tau_{\rm atmo}) + \left[\varepsilon_{\rm mirror} + (1-\tau_{\rm window})/\tau_{\rm window}\right]/\tau_{\rm mirror}}{\tau_{\rm atmo}}\tau_{\rm point}\tau_{\rm slit} \tag{2.7}$$

where $\varepsilon_{\rm mirror}$ is 0.25, $\tau_{\rm mirror}$ is 0.55, and $\tau_{\rm window}$ is 0.95.

Table 3: Average intensity values in Flat image

Detector	Order regions	Inter-order regions	Ratio
H band	4208	698	0.20[a]
K band	2345	650	0.38[a]

[a] We calculate the ratio for both H and K bands by [(698+650)/2]/[(4208+2345)-(698+650)/2] = 0.1.

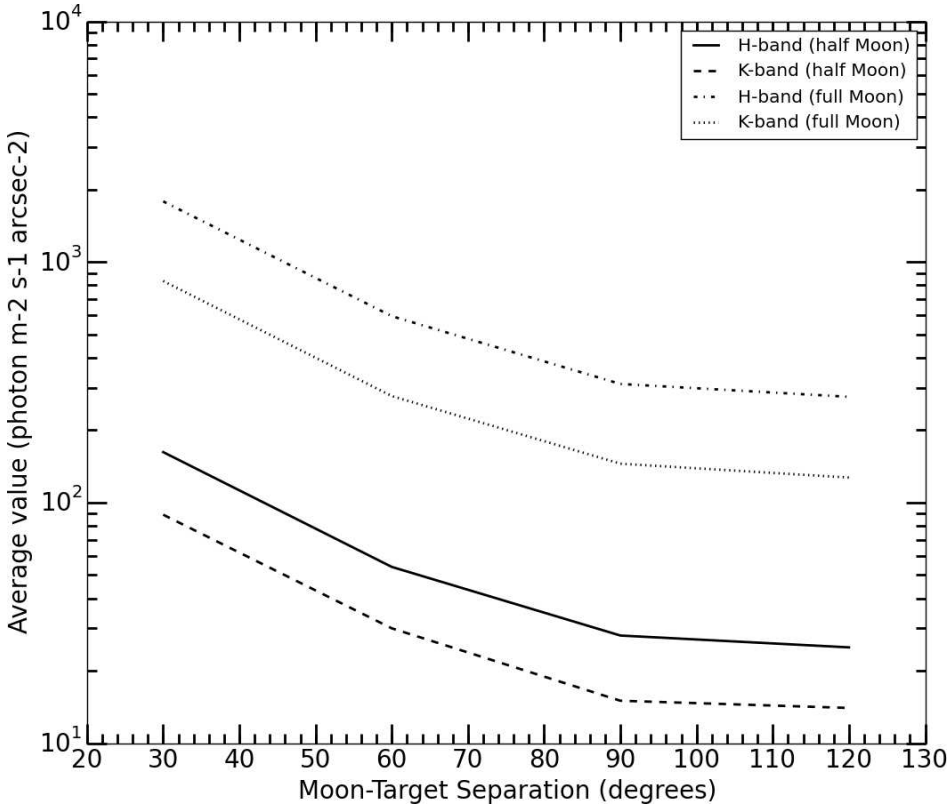

Fig. 2: Average values of the Moon light at different Moon-target separations in the case of the half Moon phase (solid and dashed lines) and in the case of the full Moon phase (dash-dot and dotted lines) in H and K bands, respectively.

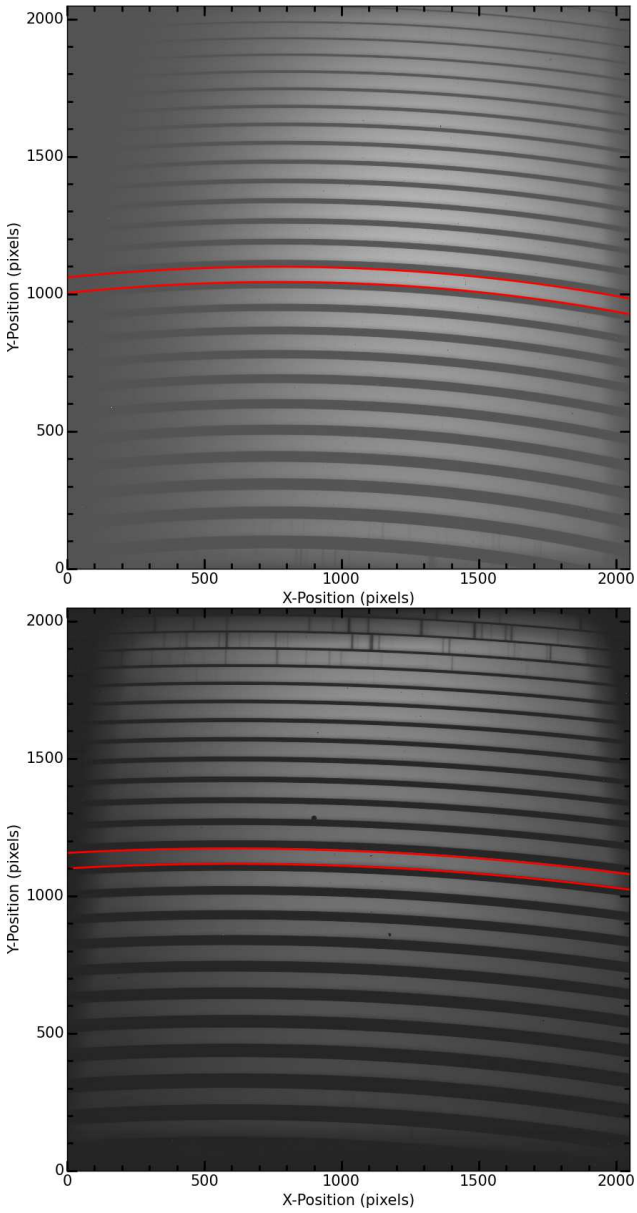

Fig. 3: Flat image in the H band (top plot) and K band (bottom plot). The red lines show the example of an order region in the echellogram. The inter-order regions are the remaining parts of the image.

2.3.3 Signal-to-Noise for Continuum

We observe point sources using the "Nod-on-Slit" mode, where we take spectra at two positions along the slit and subtract them from each other (Sim et al., 2014). This subtracts various sources of background while simultaneously gathering signal from the science target during all exposures.

The continuum signal is

$$S_{\mathrm{Cont}} = \frac{n_{\mathrm{exp}} t_{\mathrm{exp}} A \tau_{\mathrm{point}} F_{\mathrm{ZM}} 10^{-0.4m}}{hR} \tag{2.8}$$

where S_{Cont} is in units of electrons per resolution element, F_{ZM} is the zero magnitude flux density in units of W m^{-2} Hz^{-1}, m is the apparent magnitude of the continuum source, n_{exp} is the number of exposures, t_{exp} is the exposure-time, and τ_{point} is the total throughput for the point source.

The electrons collected by the detector exhibit as a Poisson distribution. The noise is calculated from the formula as

$$N_{\mathrm{Cont}} = \left[\mathrm{Q} + S_{\mathrm{Cont}}\right]^{1/2} \tag{2.9}$$

where N_{Cont} is in units of electrons per resolution element, and

$$\mathrm{Q} = 2 p_{\mathrm{slit}}^2 n_{\mathrm{exp}} \left[t_{\mathrm{exp}} \left(\varepsilon_{\mathrm{Zod,Moon,OH}} + d_{\mathrm{dark}} + \varepsilon_{\mathrm{thermal}}\right) + d_{\mathrm{read}}^2\right] \tag{2.10}$$

In this formula, p_{slit} is 3.66 pixels in the spatial and spectral resolutions, d_{dark} and d_{read} are the dark current and read noise of the infrared detector array, $\varepsilon_{\mathrm{Zod,Moon,OH}}$ and $\varepsilon_{\mathrm{thermal}}$ are given by equations in (2.5) and (2.6). For more realistic simulations, we should have considered the number of pixels in spatial and spectral resolution elements instead of p_{slit}^2 pixels. Since we always subtract a background frame, the noise term has a factor of 2 in equation (2.10).

2.3.4 Signal and Noise for Emission Lines

The ETC can simulate the IGRINS observations of emission lines given a rest wavelength, flux, doppler shift and width. We use the following definitions for the signal and noise of the emission line (Pak et al., 2004):

$$S_{\rm Line} = \Delta\lambda_{\rm pixel} \sum_{\rm i} \left(f_{\rm L,i} - \bar{f_{\rm C}}\right) \tag{2.11}$$

$$N_{\rm Line} = \Delta\lambda_{\rm pixel}\sigma(f_{\rm C,i})\sqrt{n_{\rm L}\left(1+1/n_{\rm C}\right)} \tag{2.12}$$

where $f_{\rm L,i}$ is the line flux data samples in units of W m^{-2} μm^{-1}, $\bar{f_{\rm C}}$ is the average continuum adjacent to the emission line, $\Delta\lambda_{\rm pixel}$ is the wavelength range corresponding to the pixel width at line center, $\sigma(f_{\rm C,i})$ is standard deviation of the continuum, and $n_{\rm L}$ and $n_{\rm C}$ are the sample numbers in the emission line and continuum bands, respectively.

2.4 Simulation Results

2.4.1 Photometric Mode

In the photometric mode, the ETC returns the average S/N for the H and K bands, assuming that the target is a point source. In this mode, the S/N values are computed for whole spectral H and K bands. The users can input the precipitable water vapor (PWV), the exposure-time, the number of exposures, the expected K band magnitude, the effective temperature of the source, the seeing size, and the Moon light phases.

2.4.2 Spectral Mode

The spectral mode allows the users to view plots of the calculated S/N as a function of magnitude or wavelength. Figure 4 shows the plot of S/N vs. limiting magnitude for continuum point sources in the H and K bands. Figure 5 shows the plots of S/N vs.

wavelength in the H and K bands for a blackbody source with a temperature of 6000 K, H-magnitude of 12.1, and K-magnitude of 12.0. In this spectral mode, the S/N values are variable with wavelength. In this mode, the throughput values of the atmosphere and the background signal and noise from OH emission lines are depended on wavelength. The model atmosphere is shown in Appendix A. Figures 9, 10, and 11 show the atmospheric transmission and OH emission lines in the H and K bands.

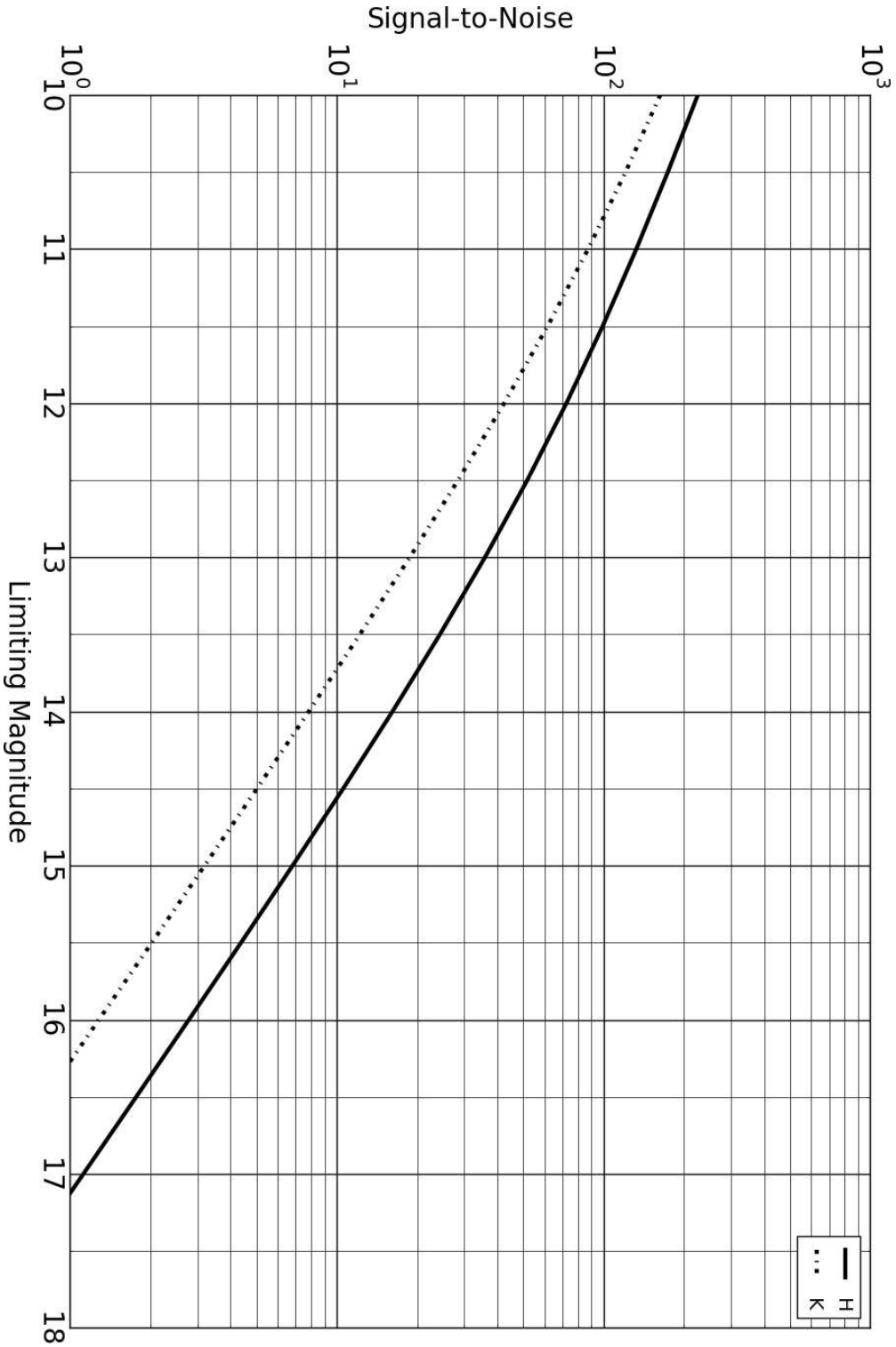

Fig. 4: Plot of S/N vs. limiting magnitude for continuum point sources in the H band and K band with exposure-time per frame, t = 600 s, and number of exposures, N = 6. The seeing is 1.2 arcsec and the PWV is 2 mm. The Moon light is not included in the calculation.

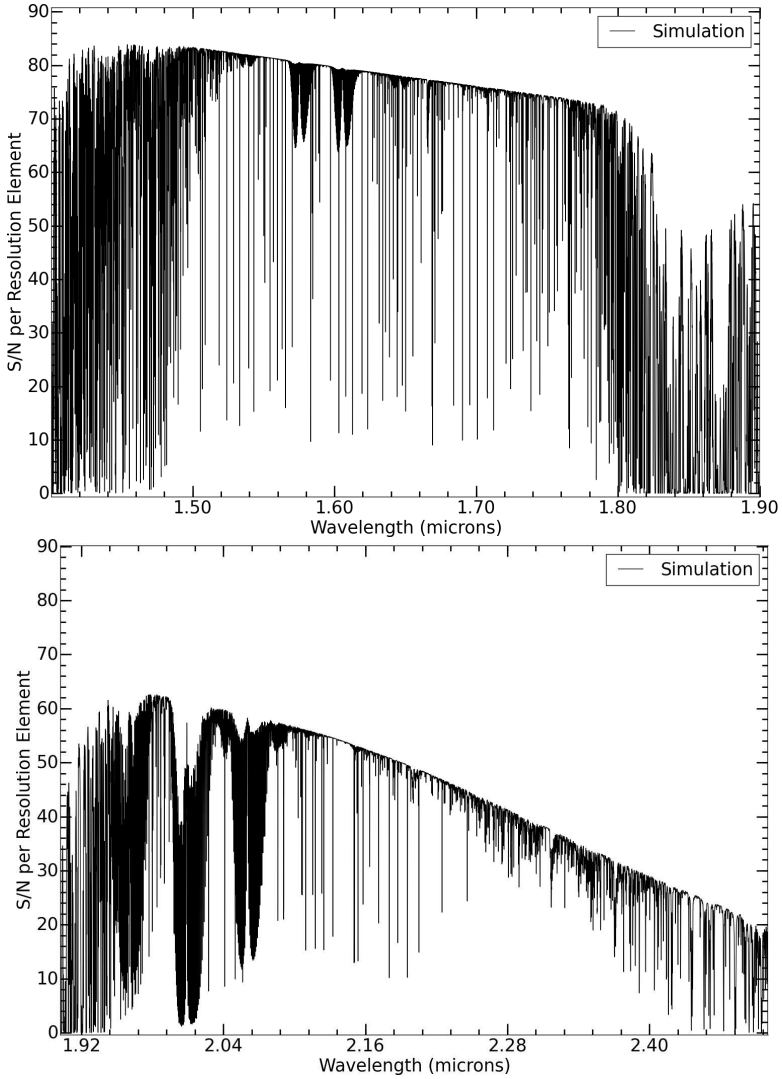

Fig. 5: Plots of S/N vs. wavelength in the H band and K band. We show a point blackbody (T = 6000 K) source with 12.1 mag in the H band and 12.0 mag in the K band. The seeing is 1.2 arcsec and the PWV is 2 mm. The exposure-time per frame is 600 s, and the number of exposures is 6. The Moon light is not included in the calculation.

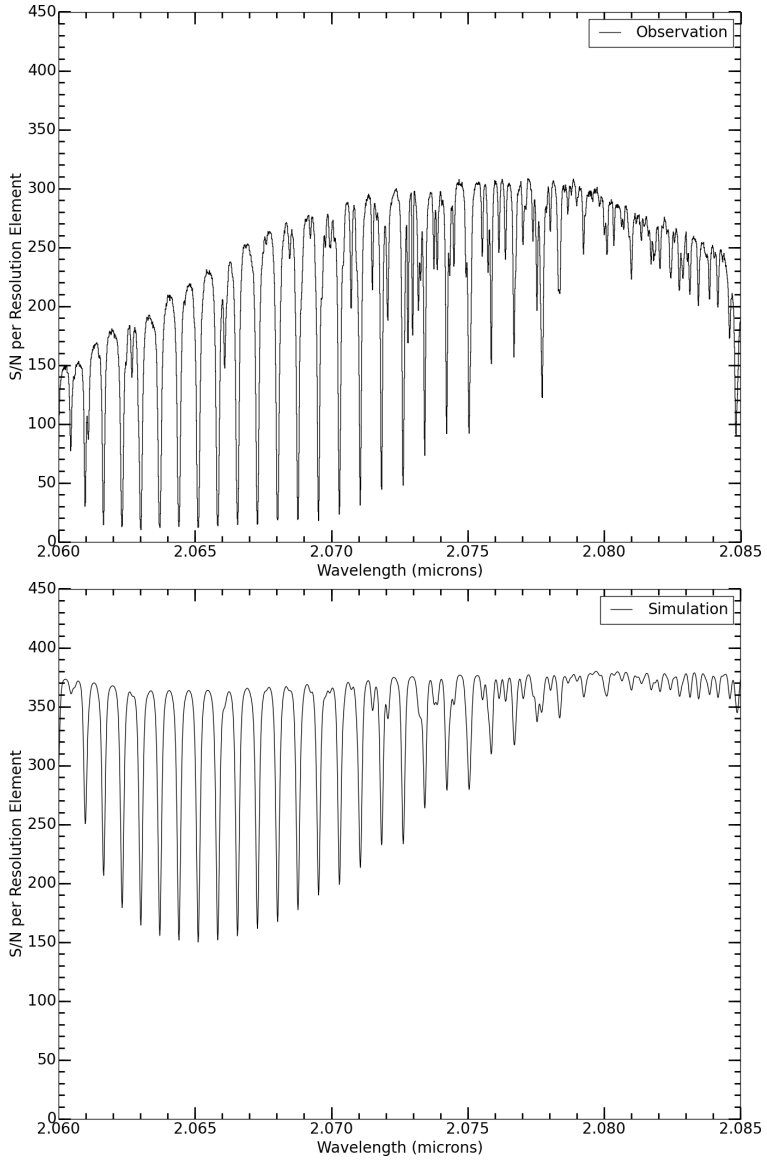

Fig. 6: Plots of S/N vs. wavelength of GSS 32 from the observational data (top plot) and simulation data from the ETC (bottom plot). The simulated data from the ETC assumes exposure times of t = 240 s, number of exposures, N = 4, the K-magnitude, $m_K = 7.324$ mag, and the effective temperature of the source, T = 1360 K. The seeing is 0.8 arcsec. The PWV is assumed to be 2 mm. The Moon light is not included in the calculation.

2.5 Test Observations

IGRINS had three commissioning runs, in 2014 March, May and July, on the 2.7 m Harlan J. Smith Telescope at McDonald Observatory. In order to compare our ETC simulation results with real observational results, we chose an early-type A0V star, HD 124683, and a late-type K5 star, GSS 32, for point source continuum targets, and a reflection nebulae, NGC 7023 for an extended line emission target. The data of HD 124683 and GSS 32 were taken by using the "Nod-on-Slit" mode on 2014 May 27. The total exposure-times are 480 s and 960 s, respectively. NGC 7023 was observed by using the "Nod-off-Slit" mode on 2014 July 13. The total exposure-time is 1200 s.

NGC 7023 is a typical example of a photodissociation region (Lemaire et al., 1996; Lemaire et al., 1999). The spectra of this target show many strong narrow emission lines from the molecular rovibrational transitions of H_2 (e.g., Martini et al., 1997; Martini et al., 1999). The observed H_2 emission lines from this target are good examples to test the simulated emission lines from the ETC. We use the A0V standard star, HD 155379, to do the absolute flux calibration for NGC 7023 (see Table 4). The flux calibration processes are based on the method of Lee & Pak (2006).

Table 4: Standard Stars

Standard star	Observing date (UT)	t_{exp} (s)	m_K[a] (mag)	Type[a]	t_{eff}[a] (K)
HD 124683	2014 May 26	120	5.552	A0V	9500 K
HD 155379	2014 Jul 12	120	6.520	A0V	9500 K

[a] http://simbad.u-strasbg.fr/simbad/sim-fbasic.

2.5.1 Signal-to-Noise for Continuum Source

We compare the S/N of an early-type A0V star, HD 124683, and a late-type K5 star, GSS 32, to the S/N calculated using the ETC. We applied the same exposure-time, the number of exposures, K-magnitude, and the effective temperature of the sources in the ETC. We also applied the measured FWHM of the point spread function in the simulations. PWV is assumed to be 2 mm. Figure 7 shows S/N of the real observational data and the simulated S/N of HD 124683. We estimate that the average S/N of the real observational data is 400, and the average value of the simulated S/N is 600. Then, the ratio of the simulated S/N and the real observational data S/N is 1.5, corresponding to 50%. Figure 6 shows the S/N values vs. wavelength of GSS 32. The average value of the simulated S/N and the real observational data S/N is 350 and 250, respectively. Then, the ratio is 1.4. The simulated S/N of GSS 32 is overestimated by 40%.

The observed spectra of the stars are curved, while the simulated spectra are flat because we did not apply the blaze function to display the grating efficiency of echelle orders in the simulations. In the simulations, we focus on the calculations of the expected average S/N values, and simply compare that to the S/N values of the real observation data. The actual numbers would be different by a factor of 1.5 depending on the blaze angles.

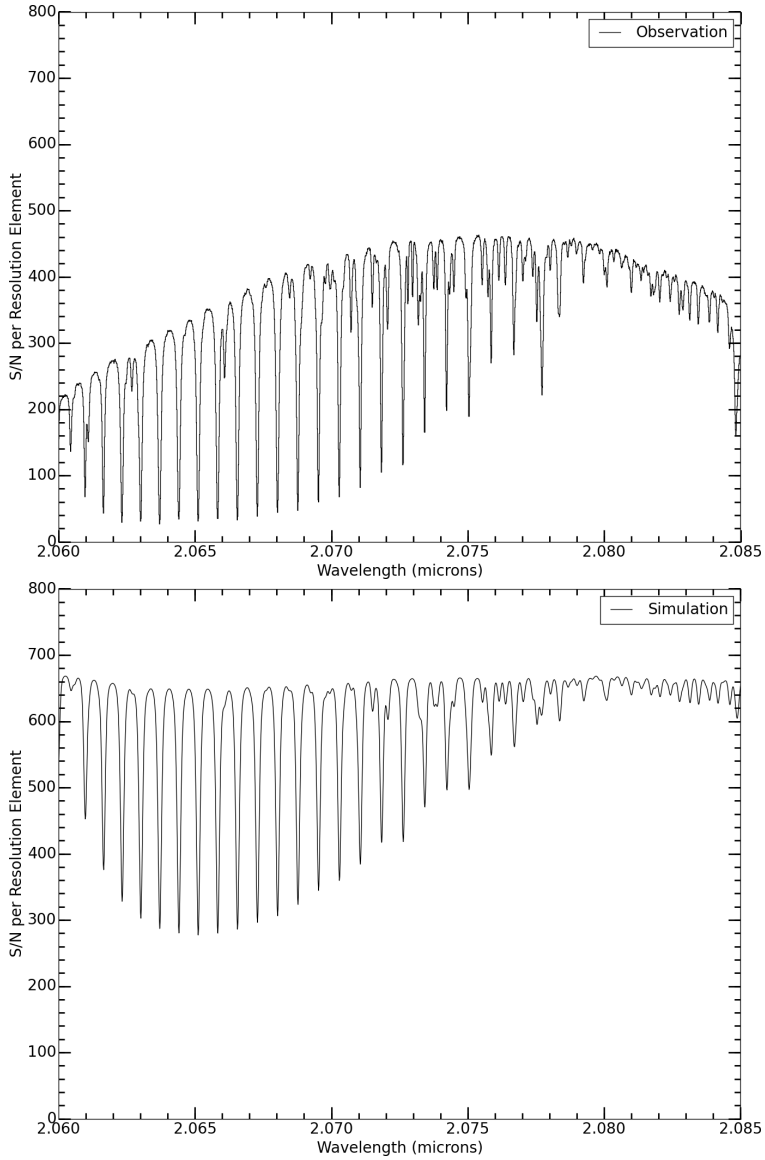

Fig. 7: Plots of S/N vs. wavelength of HD 124683 from the observational data (top plot) and simulation data from the ETC (bottom plot). The simulated data from the ETC assumes exposure times of t = 120 s, number of exposures N = 4, the K-magnitude m_K = 5.552 mag, and the effective temperature of the source T = 9500 K. The seeing is 0.9 arcsec. The PWV is assumed to be 2 mm. The Moon light is not included in the calculation.

2.5.2 Signal-to-Noise for Emission Line

We compared the simulated spectrum of NGC 7023 with those from the ETC. We applied the same exposure-time, the number of exposures, K-magnitude, and the effective temperature in the ETC. We chose a sample of the brightest emission line H_2 1-0 S(1) 2.12183 μm and the fainter emission line H_2 7-5 O(5) 2.02200 μm. In the ETC, we used the intensity values of the emission lines from Martini et al. (1997). The flux values which applied to the simulations of the IGRINS ETC are 12.8×10^{-18} and 0.81×10^{-18} W m^{-2} for H_2 1-0 S(1) and H_2 7-5 O(5), respectively. The line width value which inputted into the ETC is 9.4 km s^{-1} based fitting the shape of the line profile using a Gaussian fitting method. We applied the Doppler shift correction in the ETC of $V_{lsr} = -22.54$ km s^{-1}, this accounts for the local standard of rest radial velocity at the time of observation. Plots in Figure 8 show that the flux calibrations of the emission lines from the ETC and the observational data are approximate.

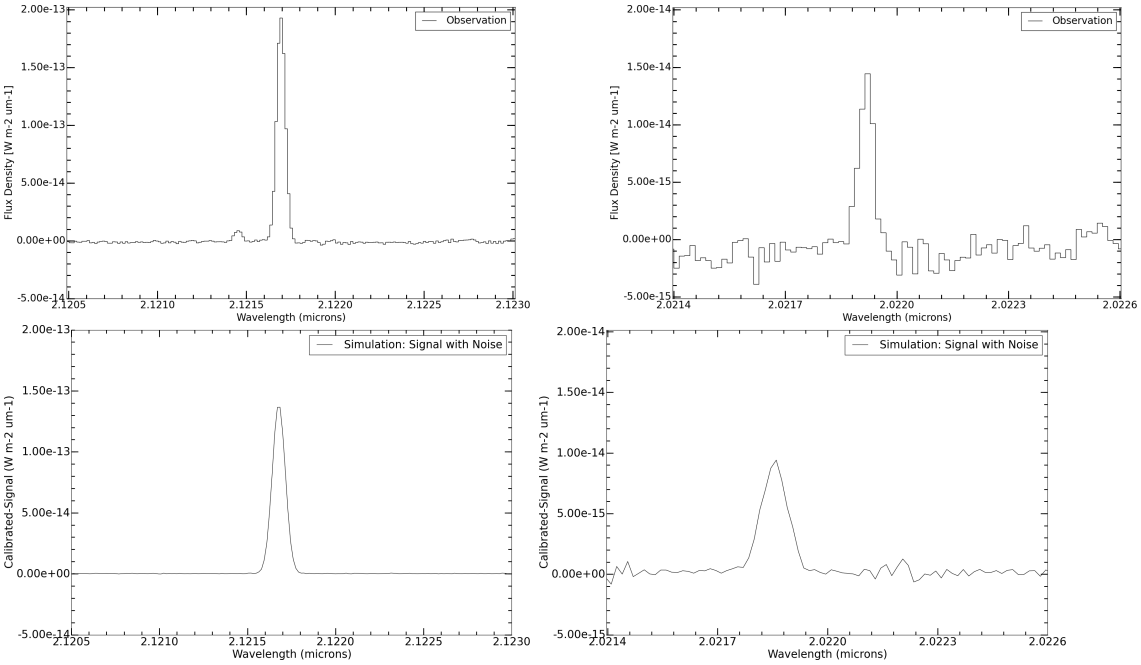

Fig. 8: Plots of observational data and the ETC simulation of NGC 7023. The left plots show the H_2 1-0 S(1) emission line, and the right plots show the H_2 7-0 O(5) emission line. We applied the Doppler shift corrections in the ETC, V_{lsr} = -22.54 km s^{-1}, the local standard of rest velocity. The flux calibration is done by comparing to the signal from HD 155379. The Moon light is not included in the calculation.

2.6 Summary

We have developed the IGRINS ETC to generate realistic simulations of both continuum and emission line sources. The signal and noise values are estimated by taking into account telluric background emission and absorption, the emission and transmission of the telescope and instrument optics, and the dark current and read noise of the infrared detector arrays. We estimate the atmospheric transmission using models that account for the amount of precipitable water vapor (PWV) along the line of sight to the target. From the ETC, the observers can estimate the S/N of the spectrum for each spectral resolution element given the exposure-time and number of exposures.

The comparisons of the S/N vs. wavelength of HD 124683 and GSS 32 show that the simulated S/N values from the ETC are overestimated by 40−50%. Note that the adopted throughput values in Table 1 are mostly from rough estimates in ideal cases. In this paper, the comparisons of the simulated S/N values with that from the observed IGRINS data test the throughput dependent aspects of the ETC.

The source-code of the IGRINS ETC version 3.10 is available to be downloaded from the website http://irlab.khu.ac.kr/∼igrins.

2.7 Model Atmosphere

We consider telluric absorption and emission lines in the IGRINS ETC using a model to calculate synthetic telluric spectra (Seifahrt, Kufl & Zngl et al., 2010). The model spectra cover from 1.4−2.5 μm with precipitable water vapor (PWV) of 2, 4, and 8 mm for the weather conditions at McDonald Observatory. The original transmission atmosphere spectra are convolved to be the same spectral resolution as IGRINS, $R = 40{,}000$ in the H and K bands. Figure 9 and 10 show the atmospheric transmission in the H and K bands.

We compiled lists of 249 bright OH emission lines from the literatures (Rousselot, Lidman & Moreels et al., 2000; Oliva & Origlia, 1992). The original OH emission line data are convolved to be the resolution of $R = 40{,}000$. Figure 11 shows the spectra of OH emission lines in the H band and K band.

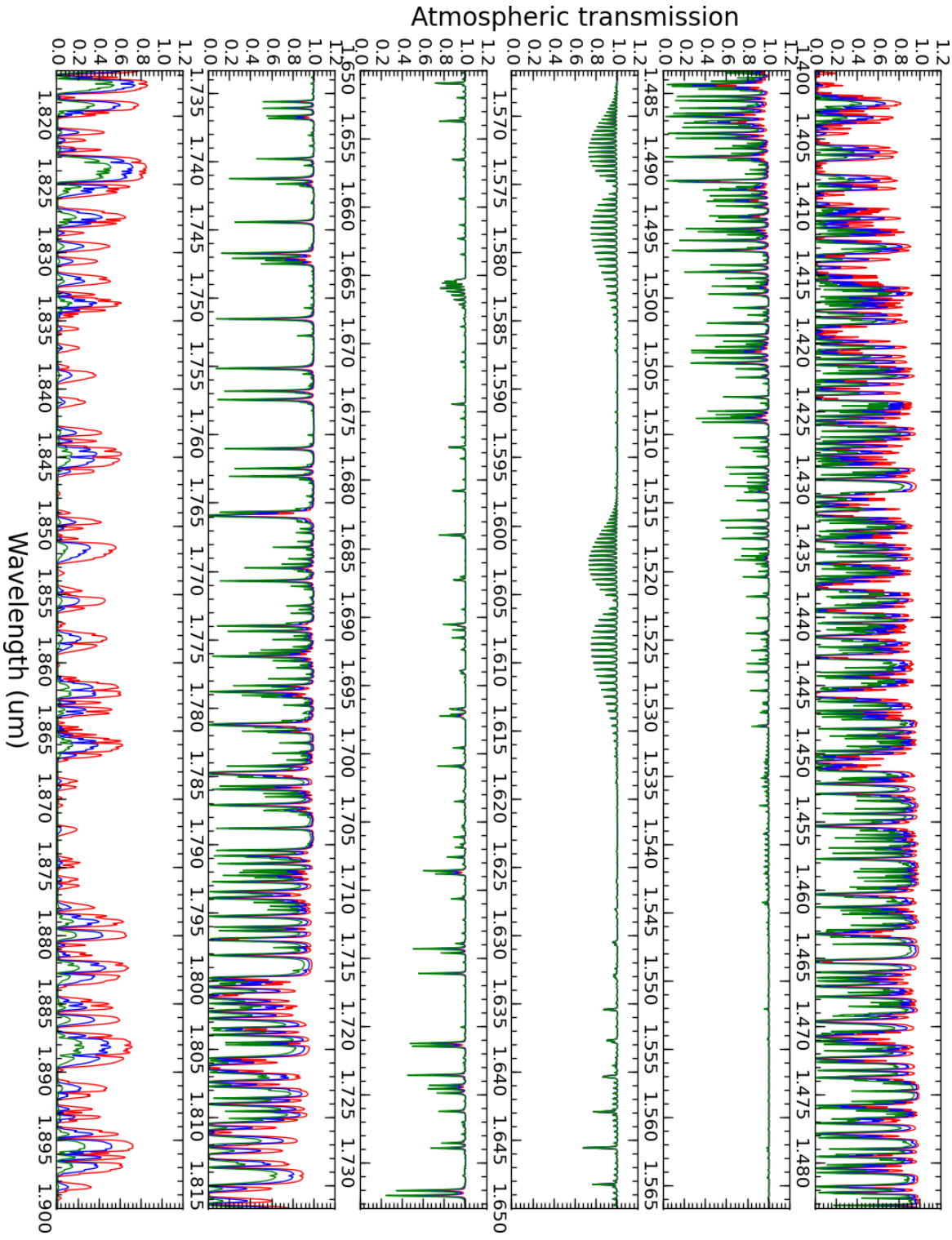

Fig. 9: Plots of atmospheric transmission in the H band. Precipitable water vapor (PWV) of 2 mm (red lines), 4 mm (blue lines), and 8 mm (green lines) for the weather conditions in the McDonald Observatory.

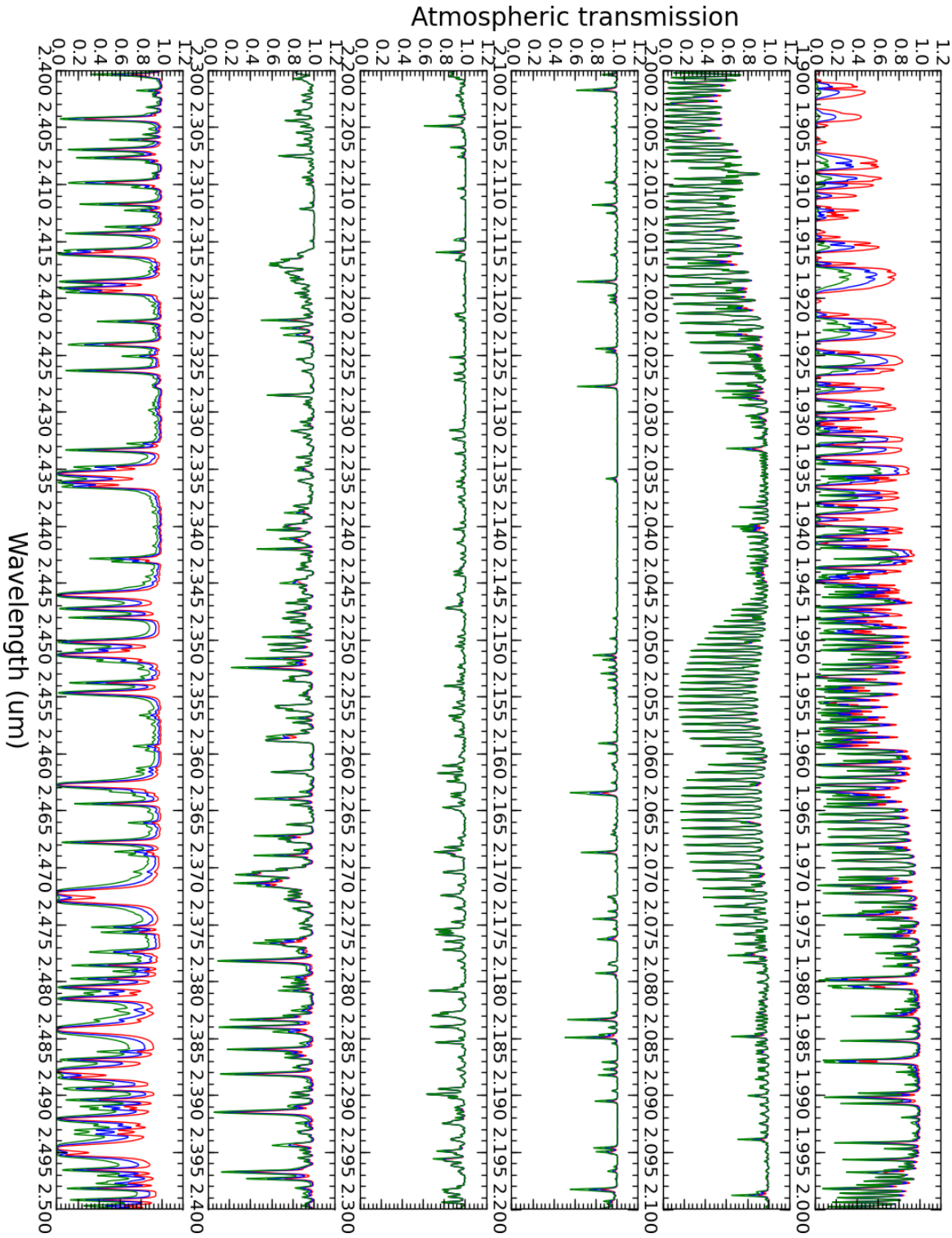

Fig. 10: Atmospheric transmission in the K band. Precipitable water vapor (PWV) of 2 mm (red lines), 4 mm (blue lines), and 8 mm (green lines) for the weather conditions in the McDonald Observatory.

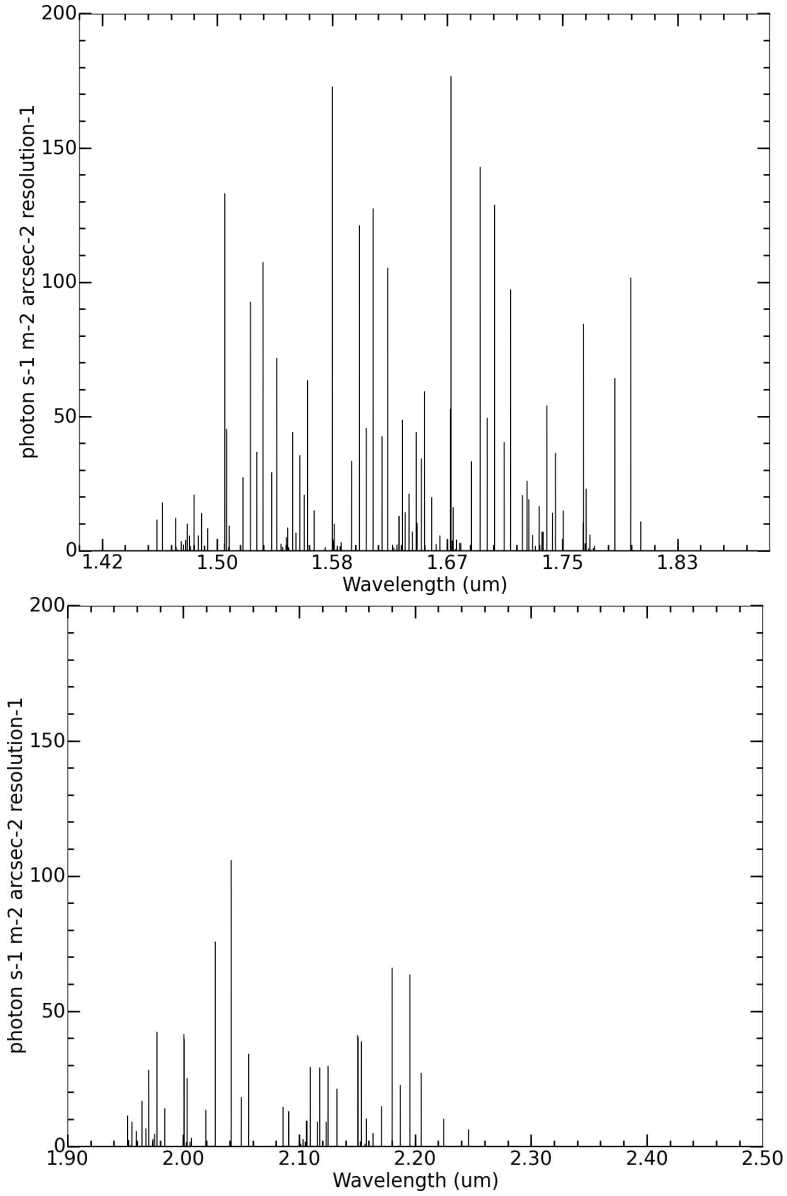

Fig. 11: Plots of OH emission lines in the H band (top plot) and K band (bottom plot).

Bibliography

Bernstein, G. 2002, Advance Exposuretime Caculations: Undersampling, Dithering, Cosmic Rays, Astrometry, and Ellipticities, PASP, 114, 98

Gully-Santiago, M., Wang, W., Deen, C., & Jaffe, D. T. 2012, Near-infrared metrology of high-performance silicon immersion gratings, Proc. SPIE, 8450

Jones, A., Noll, S., Kausch, W., Szyszka, C., & Kimeswenger, S. 2013, An advanced scattered moonlight model for Cerro Paranal, A&A, 560, A91

Li Causi, L., De Marchi, G., & Paresce, F. 2002, On the Accuracy of the Signal-to-Noise Estimates Obtained with the Exposure-Time Calculator of the Wide Field Planetary Camera 2 on Board the Hubble Space Telescope, PASP, 114, 770

Lee, S. & Pak, S. 2006, Flux Calibration Method of Slit Spectrometer for Extended Sources, JKAS, 39, 151

Lemaire, J. L., Field, D., Gerin, M., Leach, S., Pinneau des Forets, G., Falgarone, E., Rostas, F., & Rouan, D. 1996, High Spatial Resolution Observations of H_2 Vibration Emission in NGC 7023, A & A, 308, 895

Lemaire, J. L., Field, D., Maillard, J. P., Pinneau des Forets, G., Falgarone, E., Pijpers, F. P., Gerin, M., & Rostas, F. 1999, High Resolution Fourier Transform Spectroscopy of H_2 IR Emission in NGC 7023, A & A, 349, 253

Marsh, J. P., Mar, D. J., & Jaffe, D. T. 2007, Production and evaluation of silicon immersion gratings for infrared astronomy, Appl. Opt. 46, 3400-3416

Martini, P. & Sellgren, K. 1997, Near-Infrared Spectroscopy of Molecular Filaments in the Reflection Nebula NGC 7023, ApJ, 484, 296

Martini P., Sellgren, K. & Depoy, D. L. 1999, Near-Infrared Spectroscopy of Molecular Hydrogen Emission in Four Reflection Nebulae: NGC 1333, NGC 2023, NGC 2068, and NGC 7023, ApJ, 526, 772

Noll, S., Kausch, W. & Barden, M. et al. 2012, An atmospheric radiation model for Cerro Paranal I. The optical spectral range, A&A, 543, A92

Oliva, E. & Origlia, L. 1992, The OH Airglow Spectrum: A Calibration Source for Infrared Spectrometers, A&A, 254, 466

Pak, S., Jaffe, D. T., Stacey, G. J., Bradford, C. M., Klumpe, E. W., & Keller, L. D. 2004, Near-Infrared Molecular Hydrogen Emission from the Central Regions of Galaxies: Regulated Physical Conditions in the Interstellar Medium, ApJ, 609, 692-709

Park, C., Jaffe, D. T., Yuk, I.-S. et al. 2014, Design and early performance of IGRINS (Immersion Grating Infrared Spectrometer), Proc SPIE, 9147, 91471D-1

Rousselot, P., Lidman, C., Moreels, G., & Monnet, G. 2000, Night-sky Spectral Atlas of OH Emission Lines in the Near-Infrared, A&A, 354, 1134

Seifahrt A., Kufl, H. U., Zngl, G., Bean, J. L., Richter, M. J., & Siebenmorgen, R. 2010, Synthesising, using, and correcting for telluric features in high-resolution astronomical spectra, A&A 524, A11

Sim, C. K., Le, H. A. N., Pak, S. et al. 2014, Comprehensive data reduction package for the Immersion GRating INfrared Spectrograph: IGRINS, JASR, 53, 11

Wang, W., Gully-Santiago, M., Deen, C., Mar, D. J., & Jaffe, D. T. 2010, Manufacturing of silicon immersion gratings for infrared spectrometers, Proc. SPIE, 7739

Yuk, I.-S., Jaffe, D. T., Barns, S., Chun, M.-Y., Park, C., Lee, S., Lee, H., Wang, W., Park, K.-J., Pak, S., Strubhar, J., Deen, C. P., Oh, H., Seo, H., Pyo, T.-S., Park, W.-K., Lacy, J. H., Goertz, J. A., Rand. J. & Gully-Santiago, M. 2010, Preliminary design of IGRINS (immersion grating infrared spectrometer), Proc SPIE, 7735, 77351M-9

Chapter 3

Medium Resolution Near-Infrared Spectra of the Host Galaxies of Nearby Quasars[1]

3.1 Abstract

We present medium resolution near-infrared host galaxy spectra of low redshift quasars, PG $0844+349$ (z=0.064), PG $1226+023$ (z=0.158), and PG $1426+015$ (z=0.086). The observations were done by using the Infrared Camera and Spectrograph (IRCS) at the Subaru 8.2 m telescope. The full width at half maximum of the point spread function was about 0.3 arcsec by operations of an adaptive optics system, which can effectively resolve the quasar spectra from the host galaxy spectra. We spent up to several hours per target and developed data reduction methods to reduce the systematic noises of the telluric emissions and absorptions. From the obtained spectra, we identified absorption features of Mg I (1.503 μm), Si I (1.589 μm) and CO (6-3) (1.619 μm), and measured the

[1]This work has been published in Advances in Space Research (Le, H. A. N., et al. 2014, JASR, 54, 6).

velocity dispersions of PG $0844+349$ to be 132 ± 110 km s^{-1} and PG $1426+015$ to be 264 ± 215 km s^{-1}. By using an $M_{BH}-\sigma$ relation of elliptical galaxies, we derived the black hole (BH) mass of PG $0844+349$, $log(M_{BH}/M_{\odot}) = 7.7 \pm 5.5$ and PG $1426+015$, $log(M_{BH}/M_{\odot}) = 9.0 \pm 7.5$. These values are consistent with the BH mass values from broad emission lines with an assumption of a virial factor of 5.5.

3.2 Introduction

Nearby galaxies have bulge with supermassive black holes (Richstone, 1998). Understanding the link between the supermassive black holes and their host galaxies is important in studying the formation and evolution of the galaxies. The relation of $M_{BH}-\sigma$ has been discovered, in which M_{BH} is the mass of supermassive black hole and σ is the stellar velocity dispersion of the bugle (e.g., Ferrarese, Pogge, & Peterson et al., 2001; Gebhardt, Kormendy & Ho et al., 2000; Gebhardt, Bender & Bower et al., 2000).

Nevertheless, the measurements of stellar velocity dispersion of host galaxy are difficult in optical bands because of the presence of young stars in the host galaxy. Absorption lines in optical bands such as Mg b at 517 nm and Ca triplet at 850 nm are diluted by continuum. Therefore, it is necessary to use stellar lines in other wavebands in measuring velocity dispersion. CO bandheads in near-infrared (NIR) have been suggested to be the best in studying the velocity dispersion of nearby galaxies (McConnell, 2011). In addition, NIR stellar lines have the potential of explaining for the relation between supermassive back holes and their host galaxies.

In this paper, we present the medium resolution host galaxy spectra of nearby quasars in H-band obtained at the Subaru telescope. Thanks to the advantages of using adaptive optics technology, we can isolate the quasar spectra from the host galaxy spectra. The obtained spectra with medium resolution can be used to determine the stellar velocity dispersions in the bulge of the host galaxies, and to estimate the supermassive black hole

masses.

Section 2 of this paper shows the observation processes. The detailed data reduction processes of NIR quasar spectra are presented in section 3. Results and discussions are shown in section 4. Section 5 is the conclusion.

3.3 Observations

The observations were performed at the Subaru 8.2 m telescope using the IRCS (Kobayashi et al., 2000) operated with the Adaptive Optics (AO), AO36 (Hayano, Takami, & Guyon et al., 2008), on 2003 February 11 and 2004 April 3 and 4. The average AO-assisted point spread function was 0.3 arcsec.

3.3.1 Observation of Quasars

We observed three nearby quasars, PG $0844+349$, PG $1226+023$, and PG $1426+015$. Table 5 shows the log of the observations. In 2003, we observed PG $0844+349$ only. The slit width was 0.3 arcsec with R = 10^4, and the position angle of the slit was 0 deg. The echelle setting of the spectrograph was in $H+$ setting ($1.47-1.82$ μm), and the total integration time was about two hours with each exposure of 180 sec. The observations were done in an *Nod-off-slit* mode. We first observed the target and then moved the telescope to the nearby background sky. The sequences of the observations were $object \rightarrow sky \rightarrow sky \rightarrow object$.

In 2004, we observed three targets: PG $0844+349$, PG $1226+023$, and PG $1426+015$. The slit width was 0.6 arcsec with R = 5×10^3. The echelle settings of the spectrograph were in $H-$ setting ($1.46-1.83$ μm) and $H+$ setting, and the total integration time was one hour for each target. Other instrument settings and the observation modes were the same as in 2003.

Table 5: Observation log

Date (UT)	Quasars	z	R	EchelleSetting	Slit Width (arcsec)	Total Exposure (sec)
2003 Feb 11	PG $0844+349$	0.064	10000	$H+$	0.3	37×180
2004 April 3	PG $0844+349$	0.064	5000	$H-$	0.6	10×300
2004 April 3	PG $1226+023$	0.158	5000	$H-$	0.6	8×300
2004 April 3	PG $1226+023$	0.158	5000	$H+$	0.6	8×300
2004 April 3	PG $1426+015$	0.086	5000	$H-$	0.6	5×300
2004 April 3	PG $1426+015$	0.086	5000	$H+$	0.6	5×300
2004 April 4	PG $0844+349$	0.064	5000	$H+$	0.6	8×300
2004 April 4	PG $1426+015$	0.086	5000	$H-$	0.6	12×300
2004 April 4	PG $1426+015$	0.086	5000	$H+$	0.6	15×300

3.3.2 Standard Stars and Template Stars

We observed A0 V type standard stars to correct the telluric absorption lines in the target spectra. In addition, bright template stars (H $<$ 5 mag) in spectral classes of G, K, and M with the luminosity class of III are used to measure the velocity dispersions of the host galaxies.

3.4 Data Reduction

Data reduction was done by using *IRAF* [2] tasks following the methods described in Pyo (2002). The details of the data reduction for standard stars and template stars can be found in Le, Kang, & Pak et al. (2011). The host galaxy spectra were reduced by using similar procedures as that of the template stars. Fig. 12 shows the detailed data reduction processes.

The host galaxy spectra within the radius from 0.24 to 1.89 arcsec are extracted for PG 0844 + 039, and from 0.24 to 2.34 arcsec for PG 1226 + 023 and PG 1426 + 015. We chose the minimum radius to be 0.24 arcsec to ensure that the extracted host galaxy spectra are not affected by emission from QSOs. We confined the maximum radius to extract the host galaxy spectra within the effective radii (Peng, Ho, & Impey et al., 2002) of the targets. In the case of PG 0844 + 349, the maximum radius is equal to the effective radius, R_e = 1.89 arcsec. The slit length[3] of Subaru/IRCS, L = 5.17 arcsec, however, is shorter than the diameters of PG 1226 + 023 (D = 12.56 arcsec) and of PG 1426 + 015 (D = 8.22 arcsec). Therefore, the maximum radius to be extracted should be smaller than half of the slit length, L = 2.59 arcsec.

The effects of the residual OH sky-lines could cause one of the problems of our obtained

[2] *IRAF* (Image Reduction and Analysis Facility) is distributed by the National Optical Astronomy Observatories (NOAO).

[3] http://www.naoj.org/Observing/Instruments

spectra. The emission lines of OH cannot be completely corrected by the sky-background subtraction processes. We masked out the data points which contain noises from the OH sky-lines.

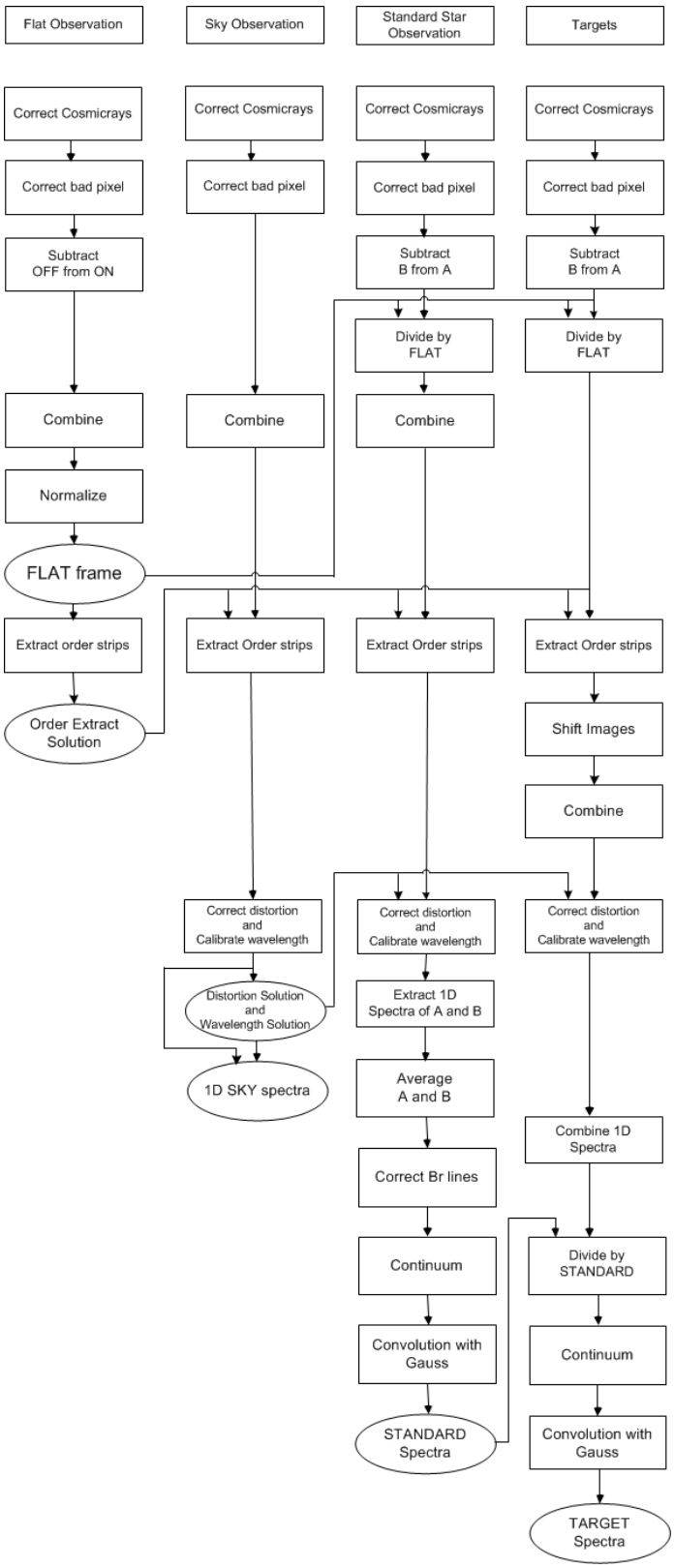

Fig. 12: Data reduction processes.

3.5 Results and Discussion

3.5.1 The Host Galaxy Spectra

Fig. 13 shows the reduced spectra of PG $0844+349$, PG $1226+023$, and PG $1426+015$. In the figure, the spectrum of K2 III (HD52071) is also plotted to be compared with the observed host galaxy spectra. In addition, the spectra of PG $1426+015$ in Watson, Martini, & Dasyra et al. (2008) and Dasyra, Taconi, & Davies et al. (2007) are shown in the figure for comparisons.

From Fig. 13, we identify prominent features, e.g., Mg I (1.488 μm), Mg I (1.503 μm), Si I (1.589 μm), and CO (6-3) (1.619 μm) in the spectrum of PG $0844+349$. But the absorption features such as CO (3-0) (1.558 μm) and CO (4-1) (1.578 μm) cannot be seen due to the effects of the remaining OH sky-lines.

After the redshift correction, the host galaxy spectrum of PG $1226+023$ in Fig. 13 has a limited wavelength coverage to be compared with the molecular lines of the stellar template spectrum. Unfortunately, these are not stellar spectra in the literature that overlap with the observed spectrum of PG $1226+023$ to identify the molecular lines.

In the case of PG $1426+015$ spectrum, we could detect Mg I (1.503 μm), Si I (1.589 μm) and CO (6-3) (1.619 μm) lines comparing the K2 III stellar template spectrum and the host galaxy spectra of Watson, Martini, & Dasyra et al. (2008) and Dasyra, Taconi, & Davies et al. (2007). But the CO (3-0) (1.558 μm) and CO (4-1) (1.578 μm) lines are hard to confirm because of the effects of the remaining OH sky-lines. The signal-to-noise (S/N) ratios of Mg I and Si I absorption lines are 3. The S/N ratio of CO (6-3) absorption line is 5.

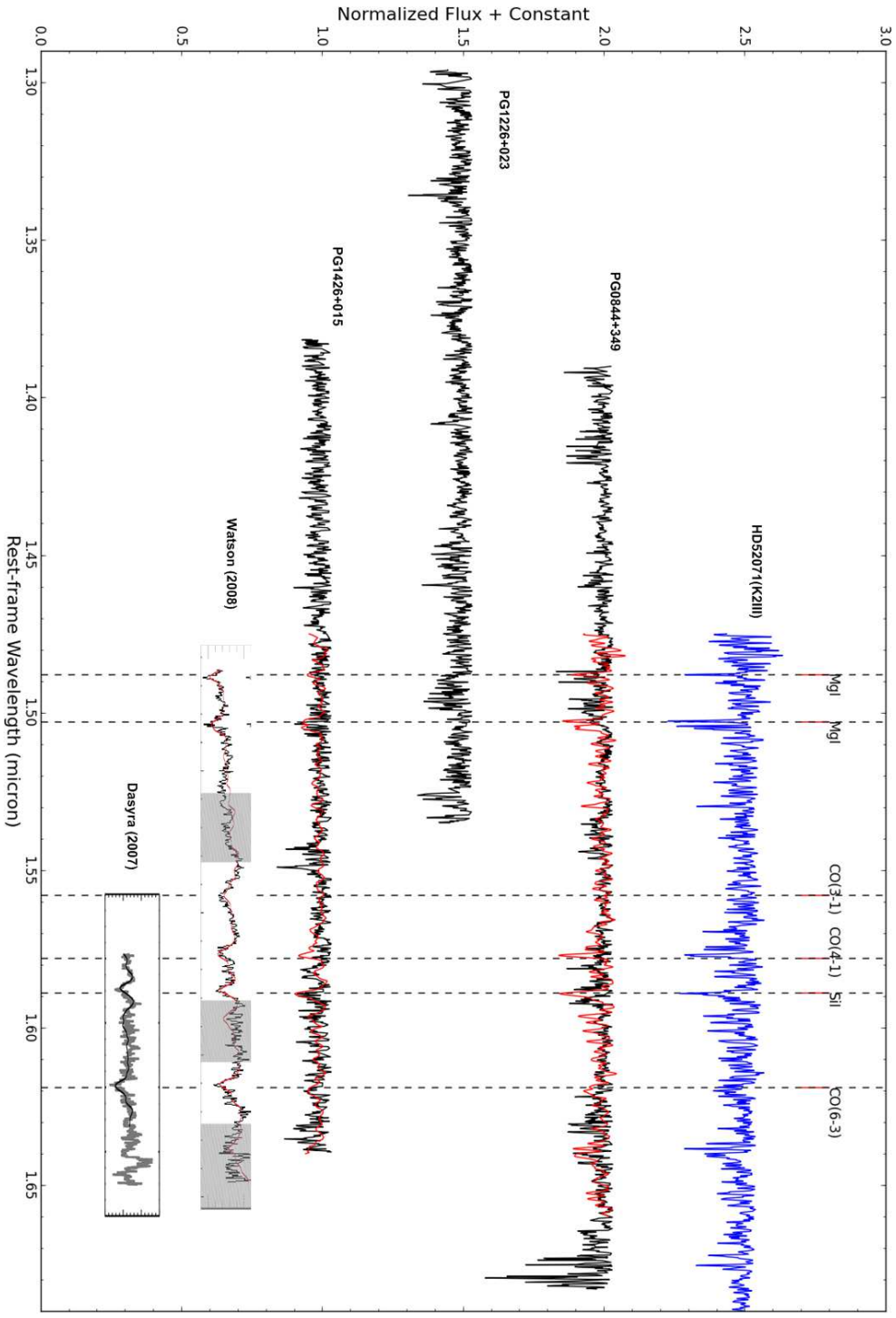

Fig. 13: Spectra of host galaxy PG $0844+349$ (shifted with $z = 0.064$), PG $1226+023$ (shifted with $z = 0.158$), PG $1426+015$ (shifted with $z = 0.086$), and spectrum of K2 III (HD52071, blue-line). The red-lines show the best fit stellar spectra of K2 III (HD52071). Two spectra at the bottom show the spectra of PG $1426+015$ from Watson, Martini, & Dasyra et al. (2008) and Dasyra, Taconi, & Davies et al. (2007).

3.5.2 Velocity Dispersion

From the obtained spectra, we identified a few stellar absorption lines of the host galaxy and measured the velocity dispersion of the host galaxy using the direct fitting method of Barth, Ho, & Sargent (2002).

We assume that the host galaxy spectrum follows that of K2 III type stars. We define the model of host galaxy spectrum from the equation as

$$M(\lambda) = A + T_G\,(\lambda, \sigma) \tag{3.1}$$

where A is arbitrary constant value from the unknown contribution from the quasar continuum; T_G is convolution of the stellar spectrum with the line-of-sight velocity distribution; σ is the velocity dispersion; and λ is the rest wavelength. The best-fit convolved stellar spectrum to the host galaxy spectrum is found based on the minimum of chi-square values. The chi-square value is calculated by

$$\chi^2 = \sum_{\lambda} \left(\frac{M_\lambda - O_\lambda}{\epsilon_\lambda} \right)^2 \tag{3.2}$$

where M_λ is the model spectrum from the equation (1); O_λ is the observed host galaxy spectrum; and ϵ_λ is the error of the host galaxy spectrum which has typical value of 0.037 and is determined by adding the standard deviation of the spectrum to the root-mean-square of each data point.

From Fig. 13, due to the redshift correction, we could not measure the velocity dispersion of host galaxy spectrum of PG $1226+023$. In case of PG$0844+349$, we identified some prominent features since the effects of the remaining OH sky-lines make it hard to calculate the velocity dispersion of the host galaxy. We have corrected the remaining OH sly-lines effects by removing those data points of the host galaxy spectra which are affected by sky-lines. We have calculated the velocity dispersion of the host galaxy PG $1426+015$ to be $\sigma = 264 \pm 215$ km s^{-1} from the fitting with K2 III stellar spectrum at Mg I (1.503

μm) line (Fig. 14) and Si I (1.589 μm) line (Fig. 15). The reduced chi-square value is 0.8. In Fig. 16, from the measurement of CO (6-3) (1.619 μm), the velocity dispersion of PG $0844+349$ is 132 ± 110 km s^{-1} with the reduced chi-square of 0.4. Due to the low S/N ratio of the data, the errors of velocity dispersions are very large. But the best-fit sigma values which are calculated from our method are consistent with others. From the measurements of Watson, Martini, & Dasyra et al. (2008) and Dasyra, Taconi, & Davies et al. (2007), the velocity dispersions of host galaxy of PG $1426+015$ are 217 ± 15 km s^{-1} and 185 ± 67 km s^{-1}, respectively, which are similar to our results. The data obtained by ISAAC long-slit spectrometer on the 8m Antu unit of the Very Large Telescope (Dasyra, Taconi, & Davies et al., 2007) has higher S/N ratio compared to our data obtained by IRCS, Subaru telescope.

From the velocity dispersion measurements, we derived the black hole masses using the $M_{BH}-\sigma$ relation of elliptical galaxies (Kormendy & Ho, 2013). Table 6 shows the measured values of velocity dispersion and black hole mass estimates of these quasars. The obtained black hole masses of PG $0844+349$ and PG $1426+015$ are $log(M_{BH}/M_{\odot})$ $= 7.7 \pm 5.5$ and $log(M_{BH}/M_{\odot}) = 9.0 \pm 7.5$, respectively.

Independently, the BH mass can be determined by using the velocity width of a broad emission line and the broad line region size from the reverberation mapping method (Kaspi, Smith et al., 2000), or the continuum/line luminosity (Kim, Im, & Kim, 2010). Assuming a virial factor of $f = 5.5$ in Onken, Ferrarese, & Merritt et al. (2004) and Woo, Schulze, & Park et al. (2013), Peterson, Ferrarese, & Gilbert et al. (2004) find that the BH masses are $log(M_{BH}/M_{\odot}) = 8.0 \pm 0.2$ for PG $0844+349$ and $log(M_{BH}/M_{\odot}) = 9.1 \pm 0.2$ for PG $1426+015$.

Table 6: Velocity dispersion measurements and black hole masses

Quasars	σ^a (km s^{-1})	σ^b (km s^{-1})	$log(M_{BH}/M_\odot)^c$	$log(M_{BH}/M_\odot)^d$
PG $0844+349$	132 ± 110^e		7.7 ± 5.5	8.0 ± 0.2
PG $1426+015$	264 ± 215^f	217 ± 15	9.0 ± 7.5	9.1 ± 0.2

[a] This work.

[b] Velocity dispersion values from Watson, Martini, & Dasyra et al. (2008).

[c] This work. Black hole mass values are derived by using the formula (7) of Kormendy & Ho (2013).

[d] Black hole mass values from Peterson, Ferrarese, & Gilbert et al. (2004).

[e] Velocity dispersion value based on the measurement of CO (6-3) (1.619 μm) line.

[f] Velocity dispersion value based on the measurements of Mg I (1.508 μm) and Si I (1.589 μm) lines.

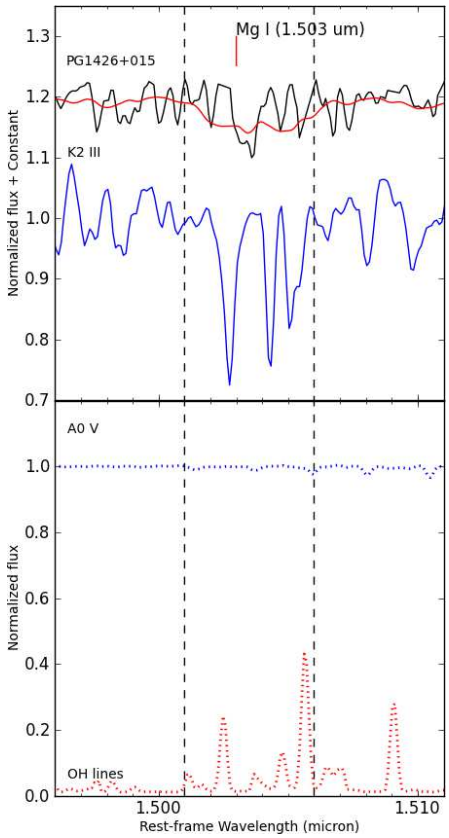

Fig. 14: Spectra of K2 III (HD52071) (blue-line) and host galaxy PG $1426+015$ (shifted with $z = 0.086$) (black-line). The best fit of the velocity convolved K2 III spectrum is shown in red-line. The dashed lines show the regions used for measurements of velocity dispersions. The A0 V and OH sky-lines spectra are shown in the lower plot.

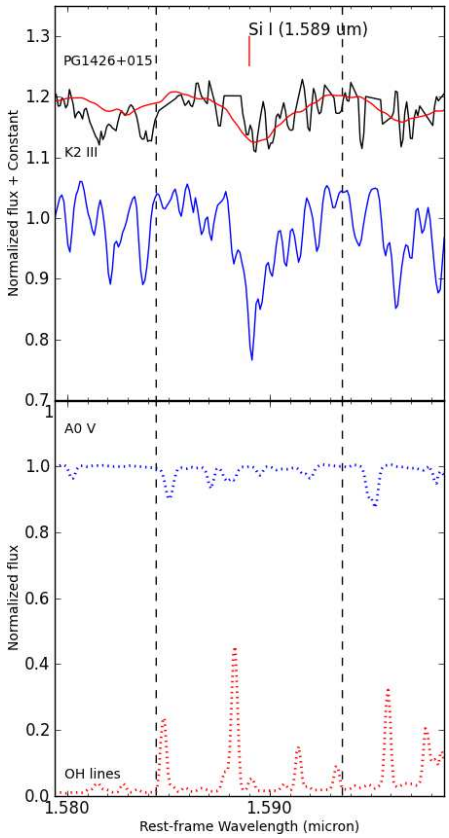

Fig. 15: Spectra of K2 III (HD52071) (blue-line) and host galaxy PG $1426+015$ (shifted with $z = 0.086$) (black-line). The best fit of the velocity convolved K2 III spectrum is shown in red-line. The dashed lines show the regions used for measurements of velocity dispersions. The A0 V and OH sky-lines spectra are shown in the lower plot.

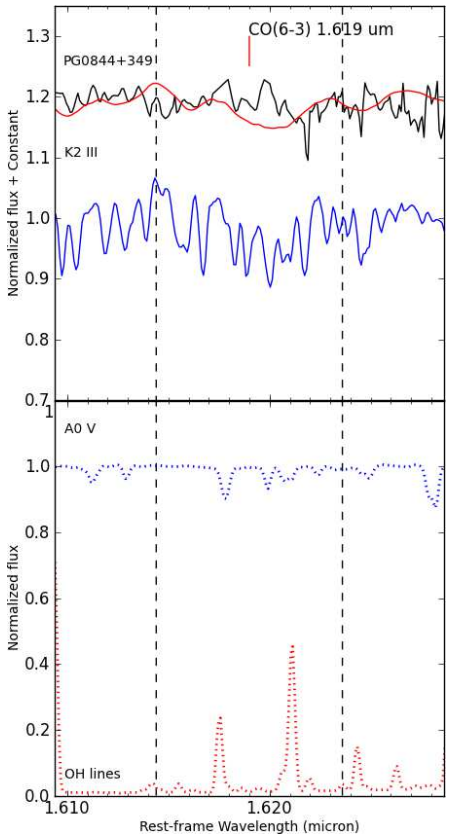

Fig. 16: Spectra of K2 III (HD52071) (blue-line) and spectra of host galaxy PG 0844+349 (shifted with $z = 0.064$). The best fit of the velocity convolved K2 III spectrum is shown in red-line. The dashed lines show the regions used for measurements of velocity dispersions. The A0 V and OH sky-lines spectra are shown in the lower plot.

3.6 Conclusions

We obtained NIR medium resolution host galaxy spectra of nearby quasars, PG 0844+349, PG $1226+023$, and PG $1426+015$ in H-band, using the IRCS instrument and the AO of the Subaru telescope. The data analysis method of the NIR spectra is presented.

From the spectra, we derived the stellar velocity dispersion of the host galaxy and its relation to the central super-massive BH. From the identified stellar absorption lines, we have obtained the velocity dispersion of PG $1426+015$ to be 264 ± 215 km s^{-1} based on the measurement of Mg I (1.503 μm) and Si I (1.589 μm). In the case of PG $0844+349$, we have measured the velocity dispersion of the host galaxy to be 132 ± 110 km s^{-1} based on the calculation of CO (6-3) (1.619 μm).

By using an $M_{BH}-\sigma$ relation of elliptical galaxies, the BH masses of PG $0844+349$ and PG $1426+015$ are estimated to be $log(M_{BH}/M_{\odot}) = 7.7 \pm 5.5$ and $log(M_{BH}/M_{\odot}) = 9.0 \pm 7.5$, respectively. These values are consistent with the BH masses from the quasar broad emission lines.

Bibliography

Barth, A. J. , Ho, L. C., & Sargent, W. L. W. 2002, A Study of the Direct Fitting Method for Measurement of Galaxy Velocity Dispersions, AJ, 124, 2607

Dasyra, K. M., Taconi, L. J., Davies, I. R., Genzel, R., Lutz D., Peterson, B. M., Veilleux, S., Baker, A. J., Schweitzer, M., & Sturm, E. 2007, Host Dynamics and Origin of Palomar-Green QSOs, ApJ, 657, 102

Ferrarese, L., Pogge, R. W., Peterson, B. M., Merritt, D., Wandel, A., & Joseph, C. L. 2001, Supermassive Black Holes in Active Galactic Nuclei. I. The Consistency of Black Hole Masses in Quiescent and Active Galaxies, ApJ, 555, L79

Gebhardt, K., Kormendy, J., & Ho, L. C., et al. 2000, A Relationship between Nuclear Black Hole Mass and Galaxy Velocity Dispersion, ApJL, 539, L13

Gebhardt, K., Bender, R., & Bower, G., et al. 2000, Black Hole Mass Estimates from Reverberation Mapping and from Spatially Resolved Kinematics, ApJL, 543, L5

Hayano, Y., Takami, H., Guyon, O., Oya, S., Hattori, M., Saito, Y., Watanabe, M., Murakami, N., Minowa, Y., Ito, M., Colley, S., Eldred, M., Golota, G., Dinkins, M., Kashikawa, N., & Iye, M. 2008, "Current status of the laser guide star adaptive optics system for Subaru Telescope," Proc. SPIE 7015, 701510

Kaspi, S., Smith, P. S., Netzer, H., Maoz, D., Jannuzi, B. T., & Giveon, U. 2000, Reverberation Measurements for 17 Quasars and the Size-Mass-Luminosity Relations in Active Galactic Nuclei, ApJ, 533, 631

Kim, D., Im, M., & Kim, M. 2010, New Estimators of Black Hole Mass in Active Galactic Nuclei with Hydrogen Paschen Lines, ApJ, 724, 386

Kobayashi, N., et al. 2000, IRCS: Infrared Camera and Spectrograph for the Subaru Telescope, SPIE, 4008, 1056

Kormendy, J., & Ho, L. C. 2013, Coevolution (Or Not) of Supermassive Black Holes and Host Galaxies, ARAA, 51, 511

Le, H. A. N., Kang, W., Pak, S., Im, M., Lee, J. E., Ho, L. C., Pyo, T. S., & Jaffe, D. T. 2011, Medium Resolution Spectral Library of Late-Type Stellar Templates in Near-Infrared Band, JKAS, 44, 125

McConnell, N. J., et al. 2011, The Black Hole Mass in Brightest Cluster Galaxy NGC 6086, AJ, 728, 100

Onken, C. A., Ferrarese, L., Merritt, D., Peterson, B. M., Pogge, R. W., Vestergaard, M., & Wandel, A. 2004, Supermassive Black Holes in Active Galactic Nuclei. II. Calibration of the Black Hole Mass-Velocity Dispersion Relationship for Active Galactic Nuclei, ApJ, 615, 645

Peng, C. Y., Ho, L. C., Impey, C. D., & Rix, H. W. 2002, Detailed Structural Decomposition of Galaxy Images, AJ, 124, 266

Peterson, B. M., Ferrarese, L., & Gilbert, K. M., et al. 2004, Central Masses and Broad-Line Region Sizes of Active Galactic Nuclei. II. A Homogeneous Analysis of a Large Reverberation-Mapping Database, ApJ, 613, 682

Pyo, T. S. 2002, Near Infrared [Fe II] Spectroscopy of Jets and Winds Emanating from Young Stellar Objects, Ph.D. thesis, Tokyo Univ.

Richstone, D., et al. 1998, Supermassive Black Holes Then and Now, Nature, 395, A14

Watson, L. C., Martini, P., Dasyra, K. M., Bentz, M. C., Ferrarese, L., Peterson, B. M., Pogge, R. W., & Tacconi, L. J. 2008, First Stellar Velocity Dispersion Measurement of a Luminous QSO Host with Gemini North Laser Guide Star Adaptive Optics, ApJ, 682, L21

Woo, J. H., Schulze, A., Park, D., Kang, W. R., Kim, S. C., & Riechers, D. A. 2013, Do Quiescent and Active Galaxies Have Different $M_{BH} - \sigma_*$ Relations?, ApJ, 772, 49

Chapter 4

Molecular Hydrogen in NGC 7023: Observations with Near-Infrared High-Resolution Spectroscopy of IGRINS

4.1 Abstract

The high-resolution spectra of near-infrared H_2 emission lines from the northern filament of the reflection nebulae, NGC 7023, are presented. The observed region is within the slit-length of $15''$. We divided the observed region into three parts based on the 1-0 S(1) line strengths. We obtain $46-66$ H_2 emission lines, vibrational states in ν=$1-13$ in each region. The column density of each ro-vibrational state from the measured H_2 emission lines is calculated. The estimate ortho-to-para ratios (OPR) are $1.57-1.62$. The OPR indicates that the H_2 emission in the observed regions arises from UV fluorescence. We see the variations of OPR in all regions. The region which has higher OPR value may has more

contribution from thermal excitation than that of other regions. We derive the hydrogen density of $\sim 10^4$ cm^{-3} by comparing the line ratio 2-1 S(1)/1-0 S(1) with that of Sternberg & Dalgarno (1989) model. Through the best-fits of observed line ratios to that Draine & Bertoldi (1996), we find the variations of density distribution in the observed regions. This results suggest that the observed regions has clumpy structure which high density clump $\sim 10^5$ cm^{-3} embedded in lower density regions, 10^3−10^4cm^{-3}. The estimate size of a clump may be ~ 0.01 pc.

4.2 Introduction

Molecular hydrogen is the major component in the interstellar medium (ISM). H_2 emission lines are formed in photodissociation regions or photon-dominated regions (PDRs), the transition layers between the ionized gases and the surface of molecular clouds, where the far-UV (FUV) photons (6 eV $\leqslant$ hν $\leqslant$ 13.6 eV) illuminate. In that layer, FUV photons directly excite atoms and molecules, then contribute significantly to the physical conditions of the region such as chemistry, structure, and temperature (e.g., Tielens & Hollenbach, 1985a; Tielens & Hollenbach, 1985b; Black & van Dishoeck, 1987; Sternberg & Dalgarno, 1989; Burton et al., 1989; Draine & Bertoldi, 1996; Luhman et al., 1997; Hollenbach & Tielens, 1999). The relative intensity of the excited H_2 is sensitive to the density and the UV field strength (Black & van Dishoeck, 1987). In high density regions ($n_H > 5 \times 10^4$ cm^{-3}), the gas density is high enough to create collisional de-excitation of the UV excited gas, and heat the region to temperature of 1000 K (e.g., Sternberg & Dalgarno, 1989; Draine & Bertoldi, 1996; Luhman et al., 1997; Luhman & Rieke, 1996).

The observations of molecular hydrogen in PDRs have been widely studied such as the reflection nebulae, NGC 2023 (Gatley, 1987; Sellgren, 1986; Hasegawa et al., 1987; Burton et al., 1998; Martini et al., 1999; McCartney et al., 1999; Habart et al., 2004, 2011; Sheffer et al., 2011; Fleming et al., 2010), the Orion (Hayashi et al., 1985; Luhman

& Rieke, 1996; Luhman, Engelbracht, & Luhman, 1998; Bertoldi et al., 1999; Rosenthal et al., 2000; Allers, Jaffe, & Lacy, 2005; Habart et al., 2004), the Omega nebulae, M17 (Chrysostomou et al., 1992, 1993; Sheffer & Wolfire, 2011), the planetary nebulae, Hublle 12 (Ramsay et al., 1993; Hora & Latter, 1996; Chrysostomou et al., 1998; Marquez-Lugo et al., 2015).

NGC 7023, the Iris nebulae, is illuminated by the Herbig B3Ve−B5 star HD 200775 (Witt et al., 2006; Alecian et al., 2008, 2013), with an effective temperature of 17,000 K (Baschek et al., 1982), at distance of 430^{+160}_{-90} pc (van den Ancker et al., 1997). Observations in mid- and far-IR bands shows various gas density structures in the nebulae (e.g., Chokshi et al., 1988; Fuente et al., 1996; Fuente et al., 2000; Fleming et al., 2010; Habart et al., 2011; Kohler et al., 2014; Pilleri et al., 2012, 2015). The low density cavity has n_H = 10^2−10^3 cm^{-3}. At the wall of the cavity, PDRs lie at $\sim$42″ northwest (n_H = 10^5−10^6 cm^{-3}), $\sim$55″ southwest, and $\sim$155″ east (n_H = 10^4−10^5 cm^{-3}) of the central illuminating star which have the FUV field intensity of G = 2600, 1500, and 250 in the units of G_0 = 1.6×10^{-3} erg cm^{-2} s^{-1} (Habing, 1968).

Observations of NGC 7023 in near-IR (NIR) bands have been studied by many authors (Sellgren, Weiner, & Dinerstein, 1992; Lemaire et al., 1996; Takami et al., 2000; An & Sellgren, 2003; Martini et al., 1997 and Martini et al., 1999). They also suggested a combination of different densities in the PDR, including dense clumps ($n \simeq 10^6$ cm^{-3}) embedded in lower density gas ($n = 10^4$−10^5 cm^{-3}).

In this paper, we present high resolution NIR spectra ($R \simeq$ 40,000) in NIR bands of the northern-west (NW) filament of NGC 7023 observed by IGRINS (Immersion Grating Infrared Spectrograph). Section 4.3 describes the observations and data reduction. Section 4.4 shows the observed H_2 emission lines. By comparing the observed emission line ratios to that of the PDR models, we derive the gas density in the observed region. The discussions and conclusions are shown in Sections 4.5 and 4.6.

4.3 Observations and Data Reduction

The NGC 7023 data was observed during the commissioning run of IGRINS on the 2.7 m Harlan J. Smith Telescope at the McDonald Observatory, on 2014 July 12. This instrument can cover the whole H and K bands (1.4−2.5 μm) in single exposure with a resolving power of $R \simeq$ 40,000. Detailed descriptions of IGRINS can be found in Yuk et al. (2010) and Park et al. (2014).

The slit center position observed in the nebula is located at 29.0″ west, 32.7″ north of the central illuminating star, HD 200775 lies at $\alpha(2000) = 21^h01^m36.9^s$ and $\delta(2000) = 68°09'47.8''$. The observation was used by the "Nod-off-Slit" mode with the sky background at 120″ north of the slit center position of the target. The slit position angle was 45° and the slit size is 1.0″ × 14.8″. From the full width at half maximum (FWHM) of the bright star in the slit-view camera image of NGC 7023, the seeing conditions during the observation was ∼ 1.0″. Figure 17 shows the slit-position of the image of H_2 emission at 2.121 μm from NGC 7023 in Lemaire et al. (1996). The total on-source exposure-time is 600 s.

The data reduction was done based on the IGRINS data reduction pipeline package[1] (Sim et al., 2014). Figure 18 shows the radial velocity diagram of 1-0 S(1) line. The peak intensity profile of 1-0 S(1) line is also displayed. We divide the observational data along the slit-length from north-east (NE) to south-west (SW) into regions of A (3-20 pixels), B (21-40 pixels), and C (41-56 pixels). The average pixel values in the regions A, B, and C are ∼ 500 ADU, ∼300 ADU and ∼100 ADU, respectively.

The spectra of A0V standard star, HD 155379, was obtained for use in atmospheric correction and absolute flux calibration. We divide the one dimensional spectra of NGC 7023 by that of HD 155379 to correct the telluric absorption lines.

[1]See also the IGRINS pipeline package at https://github.com/igrins/plp.

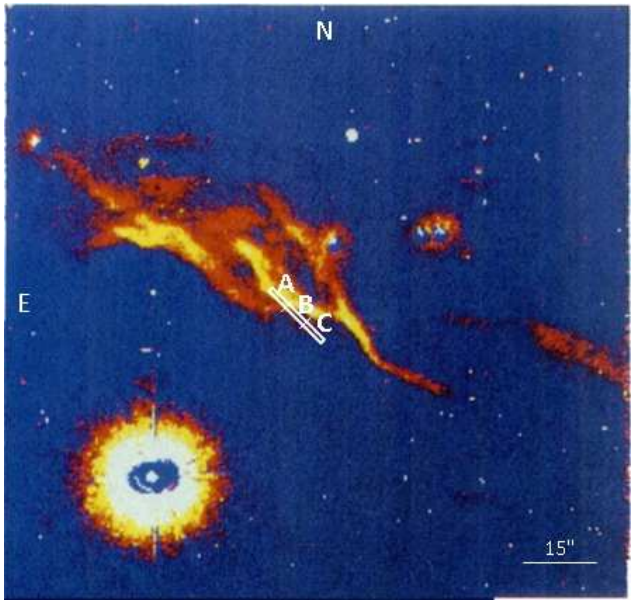

Fig. 17: Image of the H_2 emission at 2.121 μm from the north filament of NGC 7023 recorded in Lemaire et al. (1996). In the image, the central illuminating star, HD 200775 lies at $\alpha(2000) = 21^h01^m36^s.9$ and $\delta(2000) = 68°09'47''.8$. The slit-position in the image is located at $29.0''$ west, $32.7''$ north of the star. The positions of region A, B, and C are shown as text in the image.

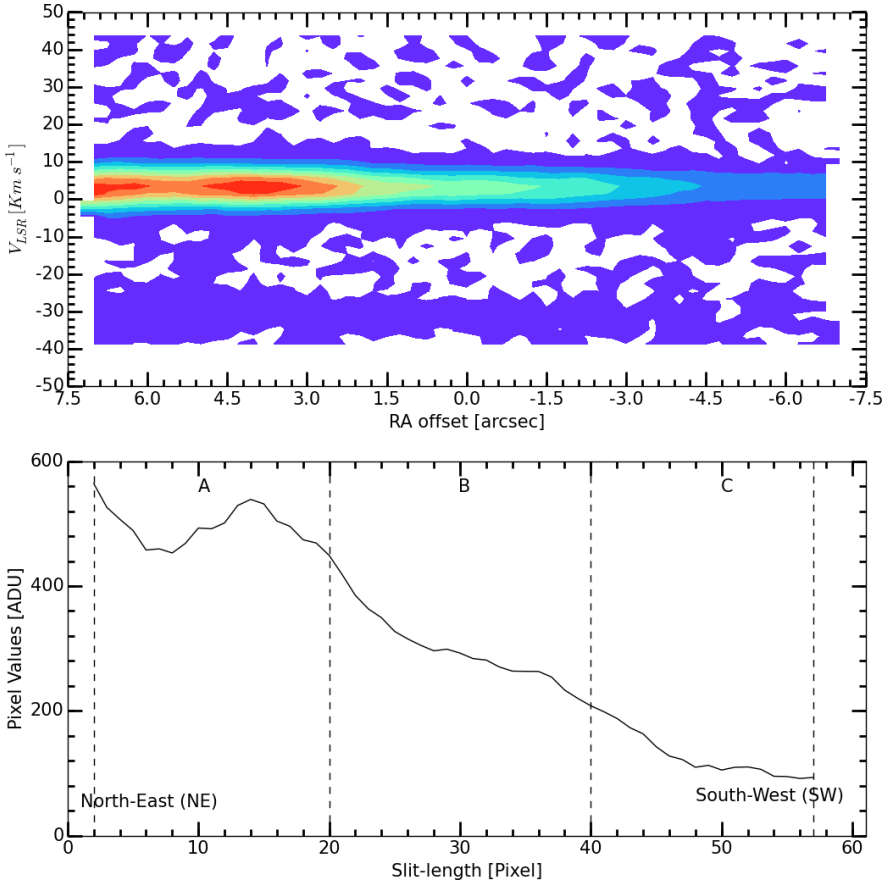

Fig. 18: Radial velocity diagram of 1-0 S(1) line (top plot). In the diagram, $1'' = 3.66$ pixels. The bottom plot shows the intensity profile at the peak of the 1-0 S(1) line. The black-dash lines show the separated regions, A, B, and C along the slit-length.

4.4 Results

4.4.1 Flux Calibration

We derive the intensity signal, I, based on the methods in (Pak et al., 2004) and (Le et al., 2015). The typical full width at half maximum (FWHM) of the detected H_2 lines are $\sim$ 8 km s^{-1}. We integrate the source signals within $\pm$12 km s^{-1} bands. The noises, σ_I, are calculated as follows:

$$\sigma_I = \sqrt{\sigma_{\rm s}^2 + \sigma_{\rm b}^2} \tag{4.1}$$

where, $\sigma_{\rm s}$ is the source-noise which is determined from the source signal, and $\sigma_{\rm b}$ is the background-noise which is derived from the variations of the adjacent continuum signals.

The flux calibration converting detector pixel value in ADU units into specific intensity units is based on the methods of Lee & Pak (2006). Note that there is a typo of the equation (8) in Lee & Pak (2006). The slit obscuration factor, $\tau_{\rm slit}$, should be

$$\tau_{\rm slit} = \frac{1}{erf(\frac{Y}{\sqrt{2}\sigma})} \tag{4.2}$$

where, Y is half of the slit-width, Y = 0.5$''$, and σ is the Gaussian width of the point spread function (PSF) along the slit-length, σ = 0.84$''$.

4.4.2 H_2 Spectra

Many H_2 emission lines were measured at the expected wavelengths from various H_2 ro-vibration transitions. From the regions A, B, and C, we extracted 66, 51, and 46 H_2 lines, respectively. The upper states are within vibration levels of ν=1$-$13 and the energy levels of E/k = 6100$-$50000 K. Figures 19$-$24 show H and K band spectra from the region A in NGC 7023. In the spectra, the intensity has been normalized by the peak of 1-0 S(1) intensity. We discarded non-reliable data whose S/N values are smaller than 5.

The measured intensity values of H_2 emission lines need to be corrected by dust extinction. We have adopted a visual extinction of $A_V = 2.2$ mag, derived from $R_V = 5$ (Mathis, 1990) and E(B-V) = 0.44 (Witt & Cottrell, 1980) as discussed in Martini et al. (1997, 1999). Note that the extinction by the local dusts around the emission regions would be altered in different line-of-sight directions. We will discuss the effects of this extinction value to our results in the discussion section.

We use IR extinction law (Cox, 2011 and references therein) to correct all line ratios.

$$A(\lambda) = 0.412 A_V \lambda^{-1.75} \tag{4.3}$$

where 0.9 μm $< \lambda <$ 6 μm.

We correct the measured intensity for extinction to obtain the intrinsic intensity.

$$I(\nu, J \rightarrow \nu', J') = I_{\rm obs} 10^{0.4 A(\lambda)} \tag{4.4}$$

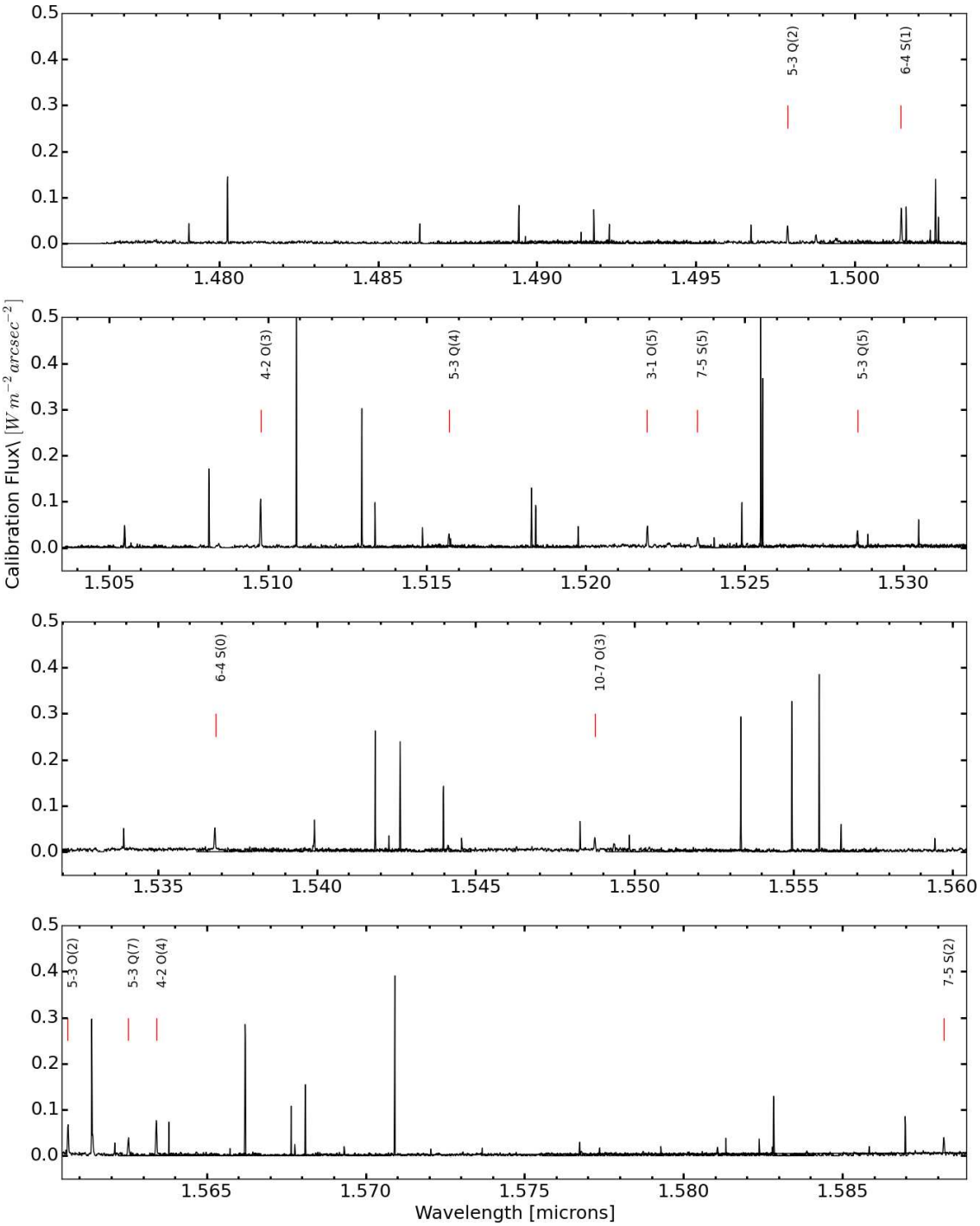

Fig. 19: *H* band spectrum (1.475−1.589 μm) of NGC 7023 (Region A). The slit-position is located at 29.0″ west, 32.7″ north of the central star, HD 200775 lies at $\alpha(2000) = 21^h01^m36^s.9$ and $\delta(2000) = 68°09'47''.8$. The intensity has been normalized by the peak of 1-0 S(1) line.

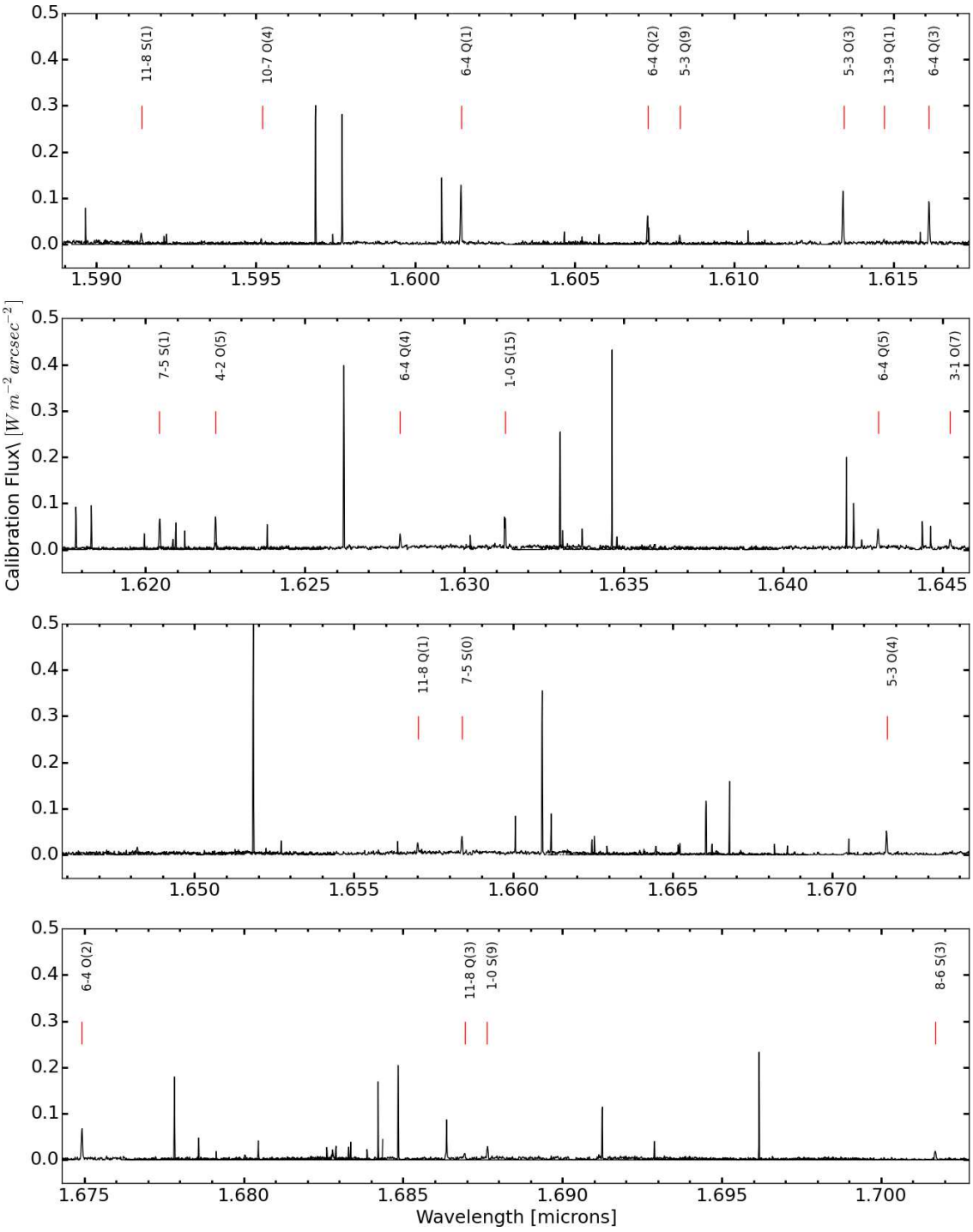

Fig. 20: Same as Figure 19, except for the wavelength is in 1.589−1.703 μm.

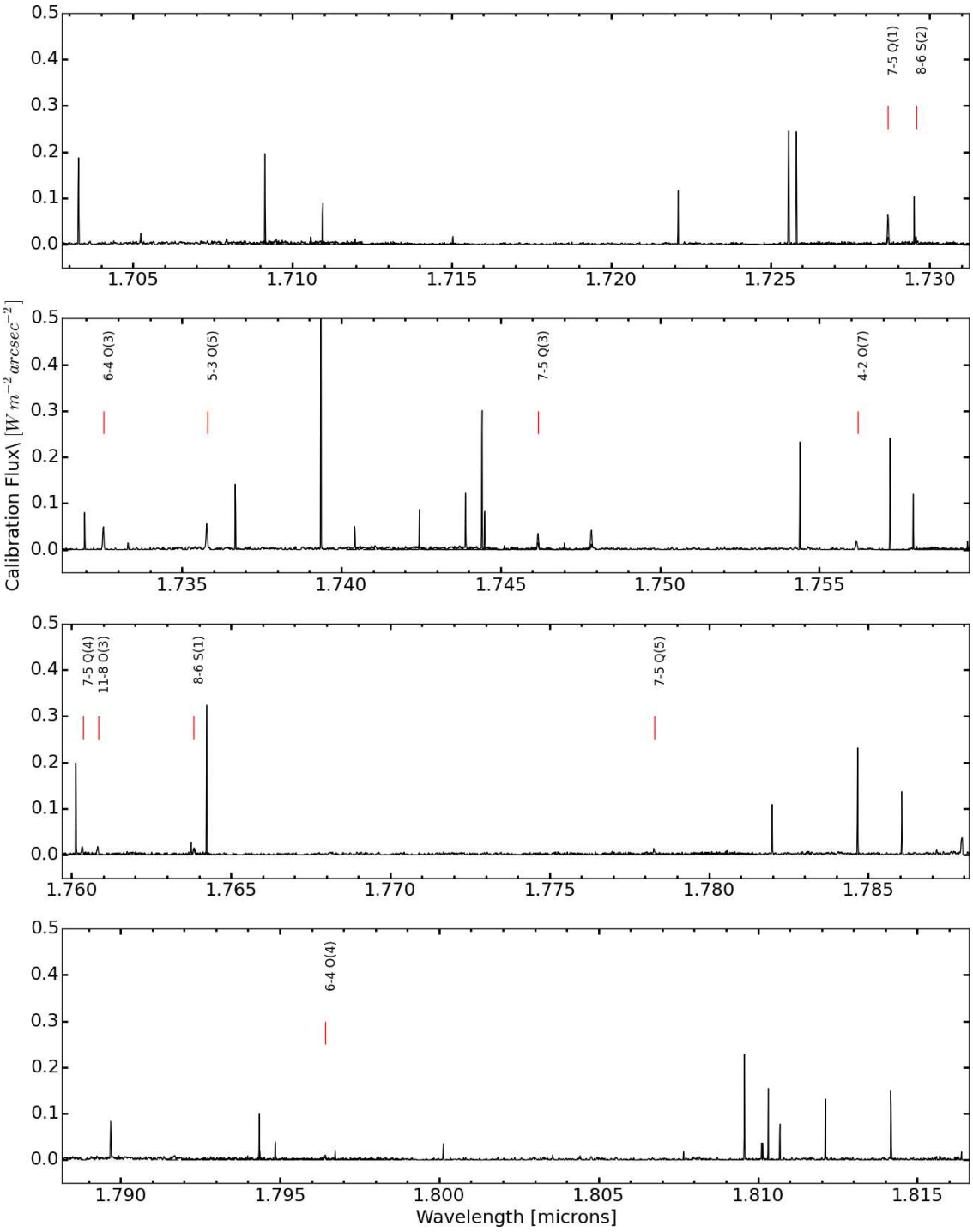

Fig. 21: Same as Figure 19, except for the wavelength is in 1.703−1.817 μm.

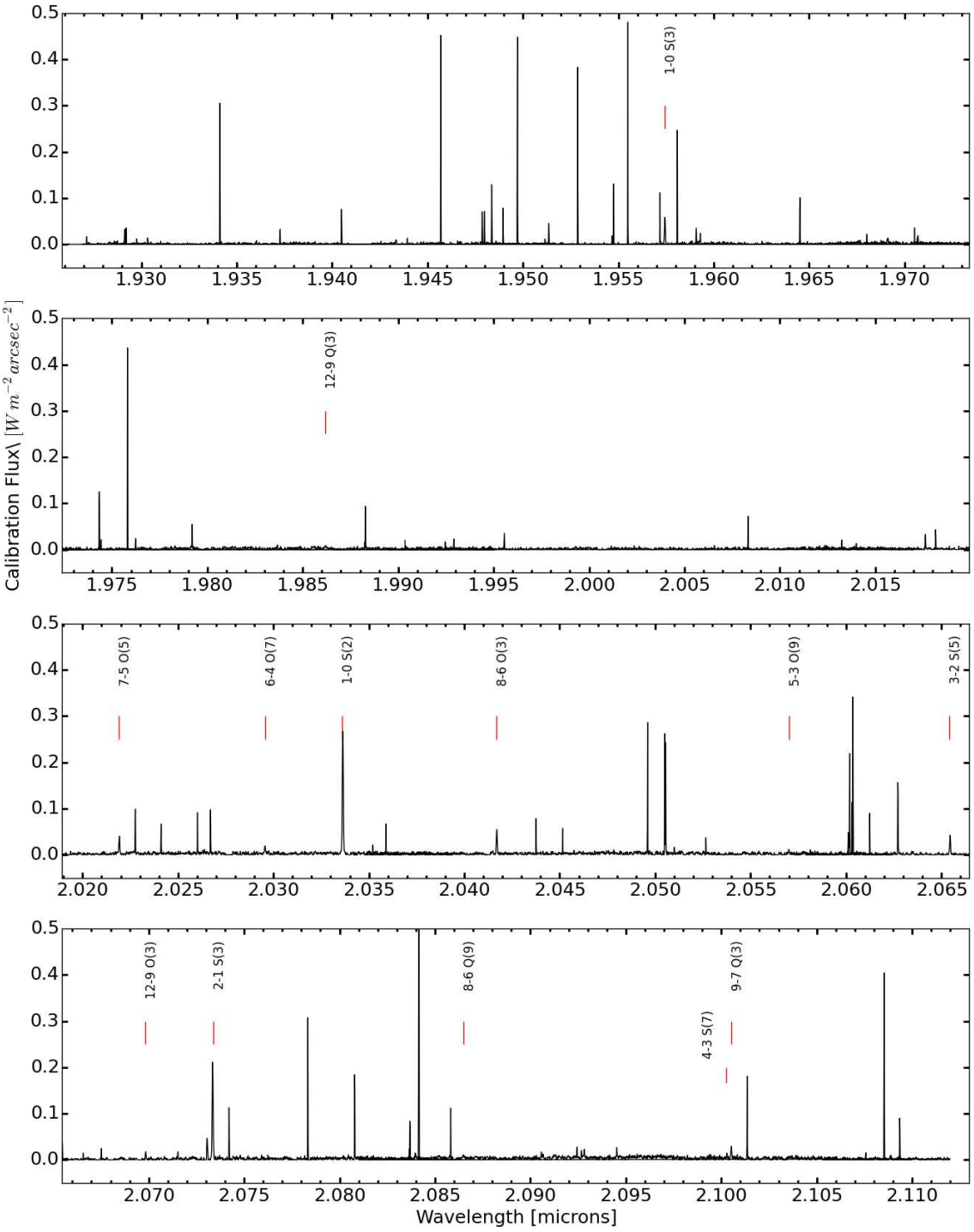

Fig. 22: Same as Figure 19, except for the wavelength is in K band, 1.926−2.114 μm.

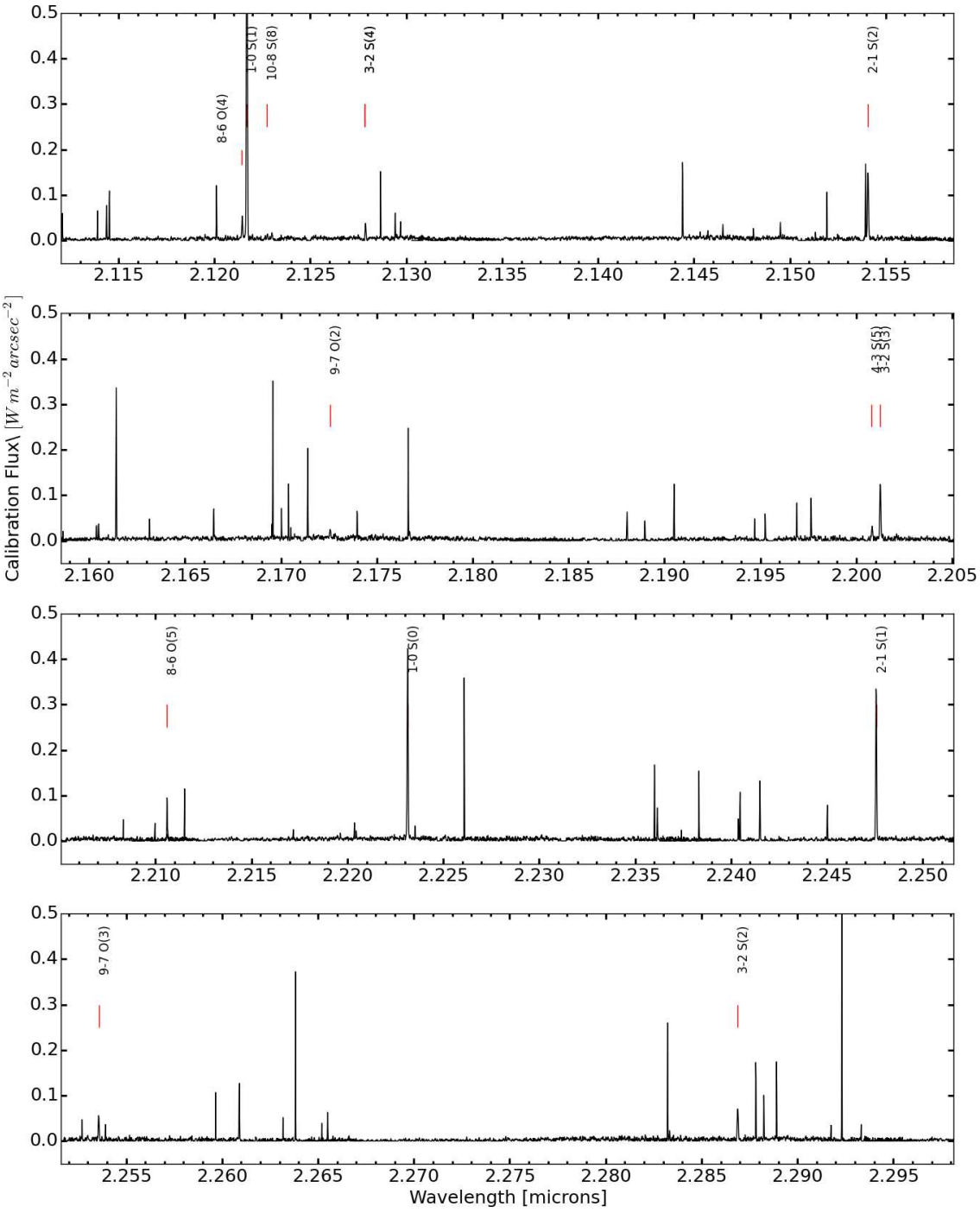

Fig. 23: Same as Figure 19, except for the wavelength is in K band, 2.114−2.298 μm.

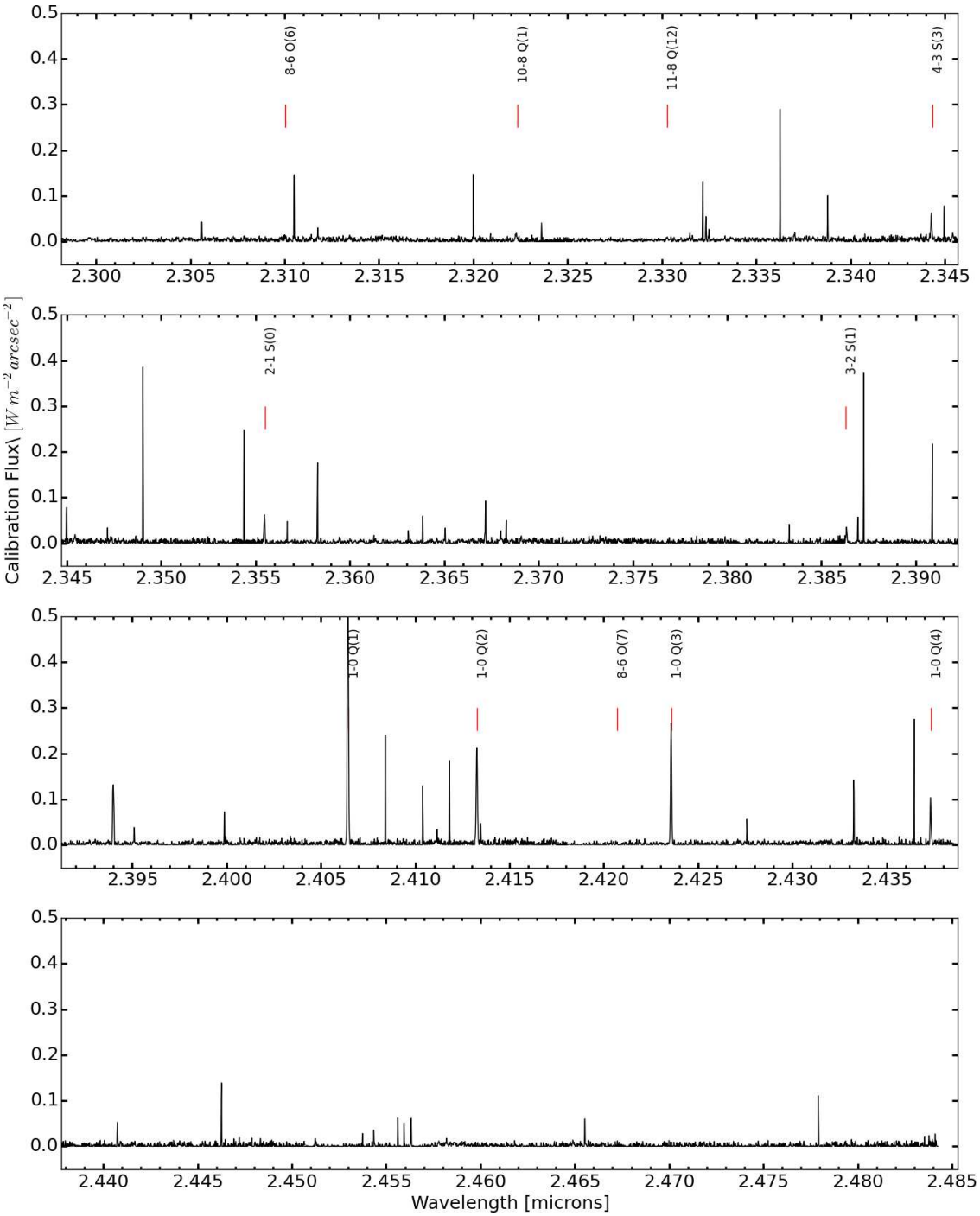

Fig. 24: Same as Figure 19, except for the wavelength is in K band, 2.298−2.485 μm.

4.5 Discussion

4.5.1 H_2 Line Ratios

The ratio of line intensity, 2-1 S(1)/1-0 S(1), is commonly used to discriminate between the thermal excitation and the non-thermal excitation from FUV photons of molecular hydrogen (e.g., Hayashi et al., 1985; Black & van Dishoeck, 1987; Burton, 1992; Pak et al., 1998; Pak et al., 2004; Lee et al., 2005). In case of fluorescent excitation in a low-density PDR ($n_{H_2} < 5 \times 10^4$ cm^{-3}), the 2-1 S(1)/1-0 S(1) ratio is ~ 0.6. In denser PDR regions or shocked regions (e.g., bipolar outflows), where collision excitations populate the levels, the ratio is ~ 0.1, which is much lower than that of the pure fluorescent case. From our data, the ratio of 2-1 S(1)/1-0 S(1) are 0.39 $\pm$ 0.01, 0.49 $\pm$ 0.02, and 0.54 $\pm$ 0.03 in the regions A, B and C, respectively. The excitation mechanism in the region C is very close to the fluorescent case while that in the region A is partially thermalized.

4.5.2 Excitation Diagram of H_2

Molecular H_2 emission lines are optically thin. Therefore, the observed upper level column density can be directly calculated from the intrinsic line intensity by,

$$N(\nu, J) = \frac{4\pi\lambda}{hc} \frac{I(\nu, J \rightarrow \nu', J')}{A(\nu, J \rightarrow \nu', J')} \tag{4.5}$$

where h is the Planck's constant, c is the speed of light, λ is the wavelength, $N(\nu, J \rightarrow \nu', J')$ is the upper level column density, $I(\nu, J \rightarrow \nu', J')$ and $A(\nu, J \rightarrow \nu', J')$ are the intrinsic intensity and the Einstein A$-$ coefficient of the transition $(\nu, J \rightarrow \nu', J')$, respectively.

We divide the level column densities by the level degeneracy g_J, and plot them against the upper level energy $E_u(\nu, J)/k$, where k is the Boltzmann's constant. The degeneracy, g_J, is $g_s(2J+1)$, where $g_s = 3$ for ortho H_2 (odd J), $g_s = 1$ for para H_2 (even J). Table

7 shows the H_2 intensities and column densities from the obtained data. Figures 25, 26, and 27 shows the excitation diagrams of molecular H_2 emission lines in regions A, B, and C, respectively. The excitation mechanism of molecular H_2 emission lines also can be delineated by these diagrams. In case of thermally excited H_2, the excitation diagram would show a single smooth function of $N(\nu, J)$ against $E_{\rm u}(\nu, J)$. In case of fluorescent excitation, the plot shows characteristic jigsaw distribution, i.e., sequences of the same vibration level curves (e.g., Hasegawa et al., 1987; Tanaka et al., 1989; Burton, 1992; Chrysostomou et al., 1993; Ramsay et al., 1993; Draine & Bertoldi, 1996; Rosenthal et al., 2000). Figures 25, 26, and 27 show jigsaw distributions which clearly indicate the H_2 emission lines are mostly UV excited.

Table 7: NGC 7023 H_2 line observation

		Region A		Region B		Region C	
Line	λ^a	I^b	$\ln(N_u/g)^c$	I^b	$\ln(N_u/g)^c$	I^b	$\ln(N_u/g)^c$
4-2 Q(9)	1.498884	0.978(0.109)	27.992(0.111)	...	...	...	...
4-2 O(3)	1.509865	4.817(0.239)	30.974(0.050)	...	...	2.200(0.164)	30.190(0.074)
5-3 Q(4)	1.515792	1.749(0.256)	30.008(0.146)	...	...	0.590(0.111)	28.921(0.188)
3-1 O(5)	1.522026	2.268(0.142)	30.738(0.062)	1.580(0.131)	30.376(0.083)	1.256(0.115)	30.147(0.091)
5-3 Q(5)	1.528641	1.739(0.128)	28.738(0.074)	1.541(0.119)	28.617(0.077)	0.598(0.080)	27.671(0.134)
6-4 S(0)	1.536908	1.389(0.104)	30.264(0.075)	1.370(0.102)	30.250(0.075)	0.620(0.061)	29.457(0.098)
10-7 O(3)	1.548851	0.747(0.068)	28.816(0.091)	0.578(0.059)	28.559(0.102)	0.172(0.027)	27.350(0.154)
5-3 O(2)	1.560730	2.023(0.131)	31.259(0.065)	1.503(0.107)	30.963(0.071)	0.858(0.081)	30.402(0.094)
5-3 Q(7)	1.562627	1.259(0.098)	28.176(0.078)	...	...	0.453(0.044)	27.153(0.097)
4-2 O(4)	1.563516	2.086(0.122)	31.156(0.058)	1.808(0.110)	31.013(0.061)	1.036(0.085)	30.456(0.082)
7-5 S(2)	1.588290	0.924(0.081)	28.829(0.088)	0.655(0.064)	28.486(0.097)	...	...
6-4 Q(1)	1.601535	3.344(0.151)	30.071(0.045)	2.747(0.136)	29.874(0.049)	1.650(0.100)	29.364(0.060)
6-4 Q(2)	1.607386	2.892(0.174)	30.860(0.060)	1.666(0.142)	30.309(0.085)	1.093(0.187)	29.887(0.171)
5-3 Q(9)	1.608395	3.131(0.329)	28.937(0.105)	2.782(0.321)	28.819(0.115)	...	...
5-3 O(3)	1.613536	4.312(0.194)	30.562(0.045)	3.462(0.171)	30.343(0.049)	2.047(0.129)	29.817(0.063)
13-9 Q(1)	1.614812	0.169(0.036)	28.006(0.212)	...	...	...	...
6-4 Q(3)	1.616211	2.330(0.119)	29.294(0.051)	1.980(0.108)	29.131(0.054)	1.192(0.086)	28.623(0.072)
7-5 S(1)	1.620530	2.086(0.127)	28.941(0.061)	1.703(0.120)	28.739(0.071)	0.835(0.079)	28.025(0.094)
4-2 O(5)	1.622292	2.346(0.156)	30.217(0.066)	1.895(0.120)	30.004(0.063)	1.792(0.129)	29.948(0.072)
6-4 Q(4)	1.628084	0.638(0.063)	28.893(0.098)	0.545(0.061)	28.736(0.113)	0.380(0.050)	28.374(0.132)
6-4 Q(5)	1.643080	1.425(0.094)	28.438(0.066)	1.056(0.081)	28.138(0.077)	0.351(0.037)	27.036(0.105)
3-1 O(7)	1.645324	0.445(0.047)	29.465(0.105)	0.414(0.045)	29.392(0.110)	0.167(0.030)	28.486(0.178)
11-8 Q(1)	1.657105	0.525(0.064)	28.521(0.121)	0.349(0.042)	28.112(0.121)	0.366(0.044)	28.159(0.120)
7-5 S(0)	1.658482	0.837(0.069)	29.789(0.083)	0.663(0.078)	29.557(0.117)	...	...

		Region A		Region B		Region C	
Line	λ^a	I^b	$\ln(N_u/g)^c$	I^b	$\ln(N_u/g)^c$	I^b	$\ln(N_u/g)^c$
5-3 O(4)	1.671821	1.706(0.114)	30.635(0.067)	1.157(0.096)	30.247(0.083)	1.084(0.086)	30.181(0.079)
6-4 O(2)	1.675019	1.770(0.101)	30.983(0.057)	1.176(0.083)	30.574(0.070)	...	...
11-8 Q(3)	1.687032	0.349(0.050)	27.730(0.144)	0.237(0.036)	27.345(0.153)	...	...
1-0 S(9)	1.687721	0.797(0.077)	28.772(0.096)	0.485(0.064)	28.274(0.133)	0.074(0.017)	26.394(0.226)
8-6 S(3)	1.701797	0.927(0.089)	27.726(0.096)	0.669(0.076)	27.399(0.114)	0.341(0.057)	26.724(0.167)
7-5 Q(1)	1.728779	2.339(0.143)	29.715(0.061)	2.183(0.145)	29.646(0.066)	...	...
8-6 S(2)	1.729667	0.924(0.083)	29.044(0.089)	...	...	0.583(0.080)	28.582(0.137)
7-5 Q(2)	1.735734	2.387(0.133)	30.673(0.056)	...	...	...	...
5-3 O(5)	1.735888	2.452(0.137)	29.921(0.056)	1.866(0.125)	29.648(0.067)	...	...
7-5 Q(3)	1.746261	6.379(0.425)	30.310(0.067)	...	...	...	...
1-0 S(7)	1.748035	3.293(0.197)	29.841(0.060)	2.147(0.163)	29.413(0.076)	...	...
4-2 O(7)	1.756296	0.746(0.076)	29.370(0.103)	0.522(0.059)	29.013(0.113)	0.236(0.034)	28.221(0.145)
7-5 Q(4)	1.760449	3.981(0.586)	30.739(0.147)	...	...	...	...
8-6 S(1)	1.763930	2.715(0.225)	29.387(0.083)	...	...	0.546(0.102)	27.783(0.187)
1-0 S(23)	1.780151	2.463(0.176)	27.236(0.072)	...	...	...	...
7-5 O(5)	2.022040	1.106(0.082)	28.853(0.074)	0.981(0.074)	28.733(0.075)	0.264(0.031)	27.421(0.116)
6-4 O(7)	2.029694	0.522(0.047)	28.390(0.090)	0.382(0.036)	28.078(0.093)	0.255(0.028)	27.672(0.110)
1-0 S(2)	2.033756	9.635(0.230)	32.623(0.024)	5.975(0.179)	32.145(0.030)	2.904(0.121)	31.423(0.042)
8-6 O(3)	2.041816	1.718(0.117)	29.512(0.068)	1.418(0.103)	29.320(0.073)	0.798(0.077)	28.745(0.097)
3-2 S(5)	2.065557	1.414(0.101)	28.981(0.072)	1.043(0.083)	28.677(0.080)	0.451(0.044)	27.840(0.098)
12-9 O(3)	2.069969	0.334(0.038)	28.463(0.114)	...	...	...	...
2-1 S(3)	2.073510	7.756(0.186)	30.755(0.024)	4.800(0.143)	30.275(0.030)	2.188(0.107)	29.489(0.049)
9-7 Q(3)	2.100659	0.382(0.034)	27.902(0.089)	0.247(0.030)	27.468(0.122)	...	...
8-6 O(4)	2.121570	0.682(0.046)	29.539(0.068)	0.549(0.045)	29.323(0.082)	0.105(0.014)	27.669(0.131)
1-0 S(1)	2.121831	21.963(0.299)	32.779(0.014)	11.800(0.218)	32.158(0.018)	5.188(0.143)	31.336(0.027)
2-1 S(2)	2.154225	4.417(0.141)	31.560(0.032)	2.810(0.114)	31.108(0.041)	1.418(0.078)	30.423(0.055)
9-7 O(2)	2.172704	0.295(0.031)	29.483(0.105)	0.245(0.025)	29.299(0.101)	0.097(0.015)	28.367(0.154)
4-3 S(5)	2.200951	0.818(0.052)	28.833(0.063)	0.374(0.035)	28.050(0.092)	...	...

		Region A		Region B		Region C	
Line	λ^a	I^b	$\ln(N_u/g)^c$	I^b	$\ln(N_u/g)^c$	I^b	$\ln(N_u/g)^c$
3-2 S(3)	2.201397	2.921(0.109)	29.859(0.037)	2.108(0.093)	29.533(0.044)	0.851(0.059)	28.626(0.070)
8-4 O(22)	2.213687	0.124(0.038)	...	...	...	...	...
1-0 S(0)	2.223299	9.170(0.203)	33.705(0.022)	5.221(0.152)	33.142(0.029)	2.543(0.103)	32.422(0.041)
2-1 S(1)	2.247721	8.644(0.214)	31.544(0.025)	5.754(0.174)	31.137(0.030)	2.813(0.119)	30.421(0.042)
9-7 O(3)	2.253719	1.079(0.072)	29.258(0.067)	0.782(0.057)	28.936(0.074)	0.477(0.051)	28.442(0.108)
3-2 S(2)	2.287026	1.825(0.096)	30.726(0.053)	1.418(0.082)	30.473(0.058)	0.785(0.061)	29.882(0.078)
8-6 O(6)	2.310178	0.546(0.092)	29.345(0.169)	...	...	...	...
10-8 Q(2)	2.337306	0.231(0.030)	29.189(0.131)	...	...	...	...
4-3 S(3)	2.344479	1.285(0.077)	29.307(0.060)	0.793(0.054)	28.824(0.068)	0.269(0.031)	27.744(0.117)
2-1 S(0)	2.355629	3.698(0.237)	32.478(0.064)	2.442(0.187)	32.063(0.076)	1.339(0.142)	31.462(0.106)
1-0 Q(1)	2.406594	34.887(0.463)	34.003(0.013)	16.204(0.310)	33.236(0.019)	7.000(0.211)	32.397(0.030)
1-0 Q(2)	2.413436	11.248(0.300)	33.809(0.027)	6.927(0.228)	33.325(0.033)	3.124(0.151)	32.528(0.048)
1-0 Q(3)	2.423731	17.835(0.455)	32.925(0.026)	9.108(0.321)	32.253(0.035)	4.251(0.222)	31.491(0.052)
1-0 Q(4)	2.437491	5.949(0.205)	32.728(0.034)	4.625(0.178)	32.476(0.038)	3.614(0.176)	32.230(0.049)

[a]The wavelengths are in vacuum. The unit is in μ.

[b]The intensity has been corrected for extinction. The unit is in 10^{-19} W m^{-2} arcsec^{-2}. Uncertainties are written in parentheses.

[c]Extinction corrected upper level column density. The unit is in ln(cm^{-2}).

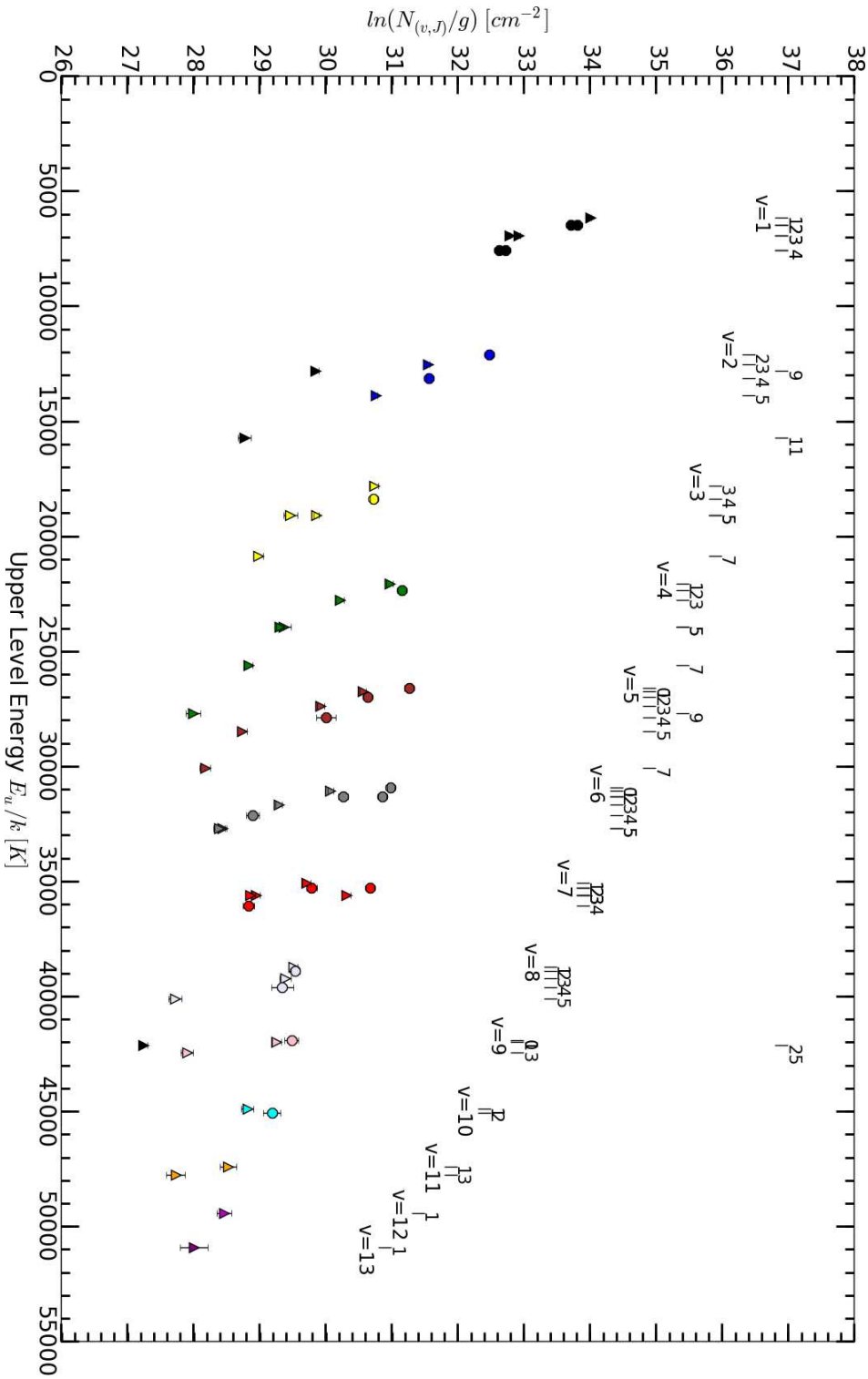

Fig. 25: Excitation diagram of the H_2 level column density distribution for region A. The observed column densities have been corrected for extinction, $A_V = 2.2$ mag. The column densities have been divided by the level degeneracies, assuming ortho-to-para ratio is 3. The circles and triangles present ortho and para H_2, respectively.

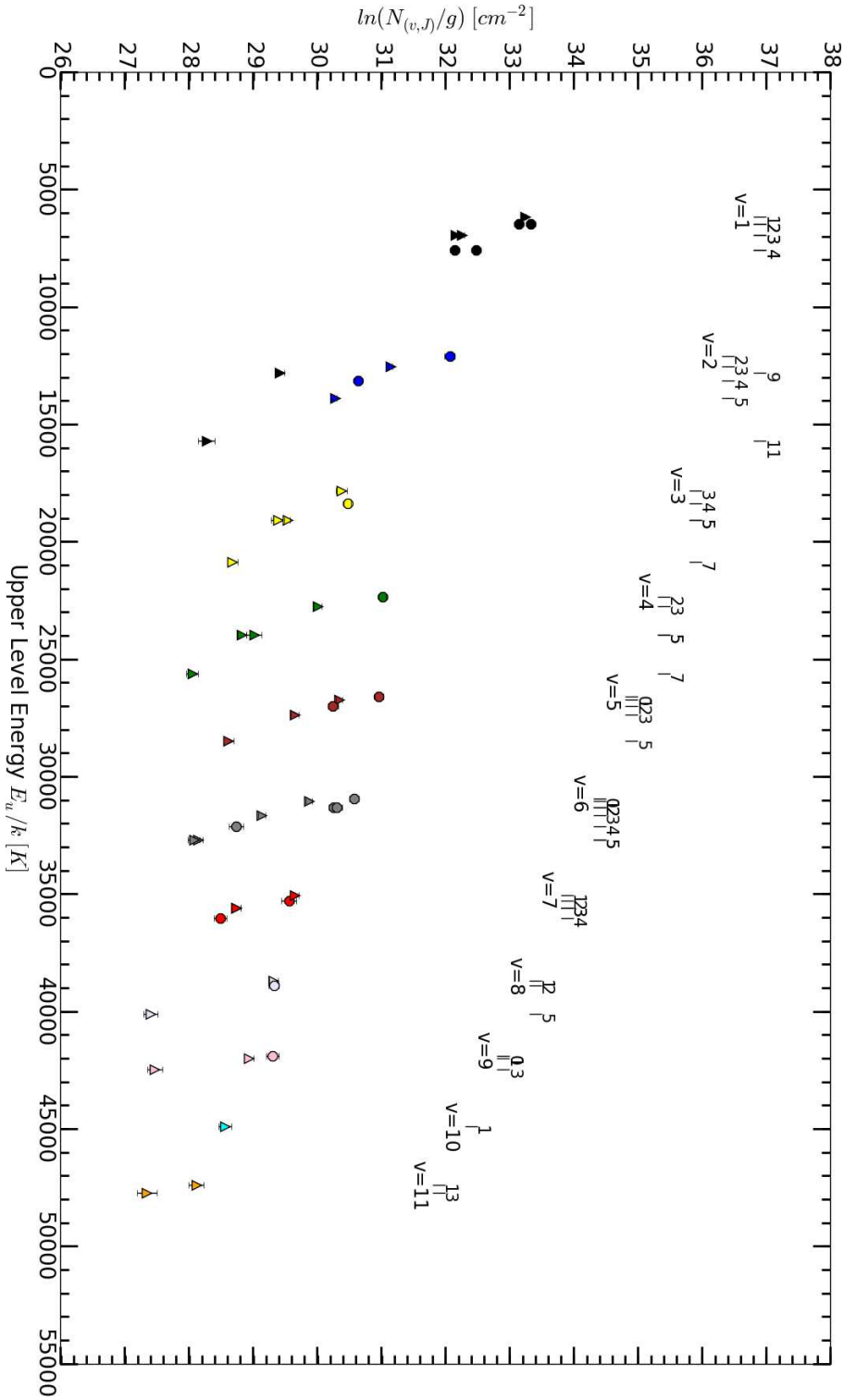

Fig. 26: Same as Figure 25, except for spectra in region B.

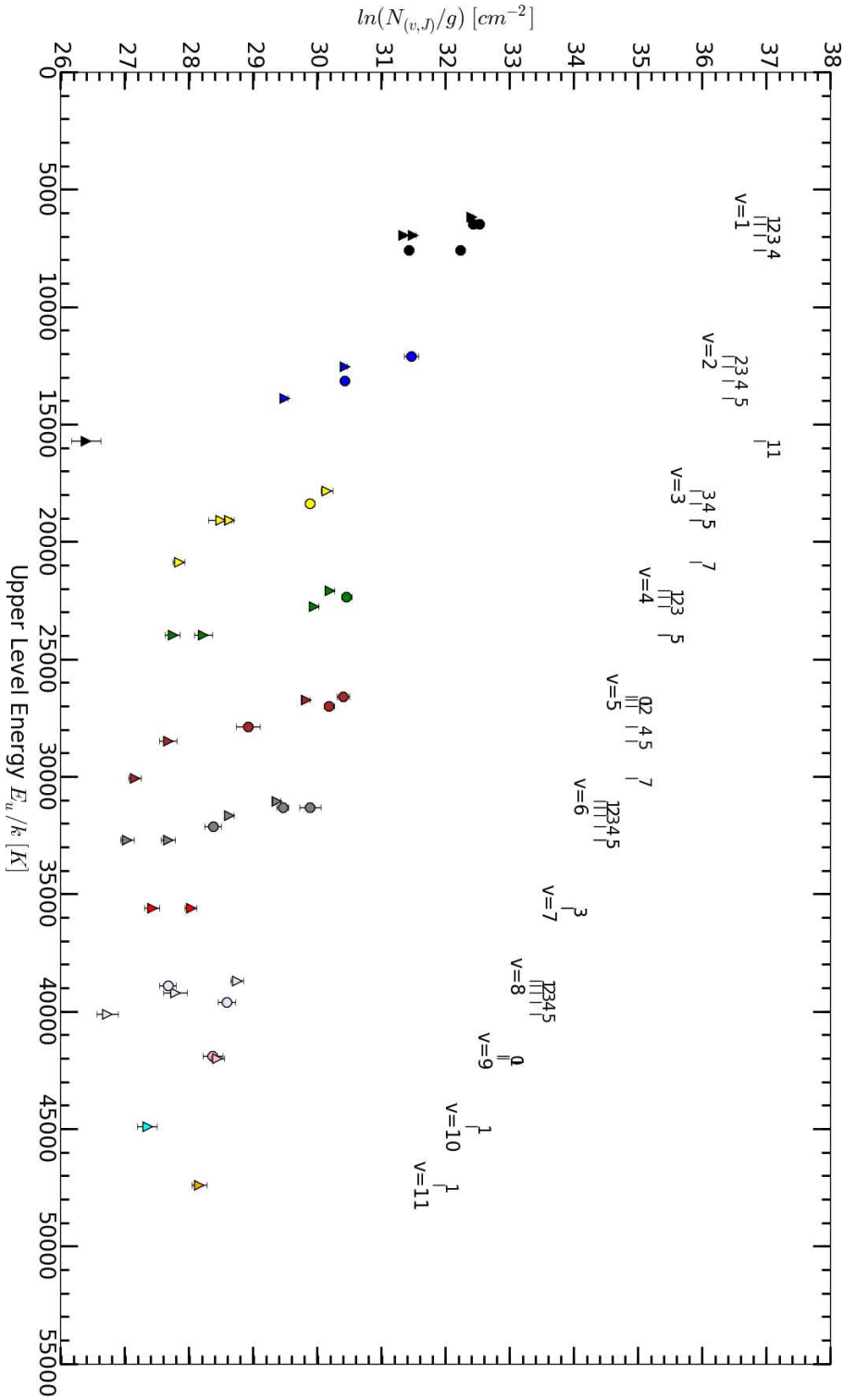

Fig. 27: Same as Figure 25, except for spectra in region C.

4.5.3 Ortho-to-Para Ratio

Ortho H_2 has total nuclear spin of 1 and presents only in the rotation quantum number states of odd J, and para H_2 has total nuclear spin of 0. Ortho-to-Para ratio (R_{OP}) of molecular hydrogen H_2 is the ratio of the total column density of ortho H_2 to that of para H_2, divided by the degeneracy g_J (Martini et al., 1997). This ratio reflects the physical condition of H_2 formation such as grain temperature (Hasegawa et al., 1987). When H_2 is formed on the grain surface, R_{OP} is initially to have value of 3 in case of local thermodynamic equilibrium (LTE). Over the time, R_{OP} can be altered by the exchange reaction of H_2 with other gas as atomic hydrogen and H^+ (Burton, 1992; Sternberg & Neufeld, 1999). The rates of this reaction are strongly dependent on the temperature. At high temperature T > 300 K, the value of R_{OP} is 3. Otherwise, in the case of lower temperature, T $< \sim$ 200 K, the R_{OP} has lower values (Burton, 1992).

The study in the literatures show that the R_{OPR} have values from 1-1.8 in the case of H_2 fluorescent excitations. The first evidence indicates that R_{OP} has different value from 3 is Hasegawa et al. (1987) by the observations of NGC 2023. They estimated the R_{OP} in range of 1.4−2.0. Tanaka et al. (1989) found similar results that R_{OP} has value less than 3 in PDRs. Chrysostomou et al. (1993) found that $R_{OP} = 1.8 \pm 0.5$ for the Omega nebulae M17. Habart et al. (2011) estimated the value of $R_{OP} = 1.8$ for NGC 2023. Fuente et al. (2000) found that R_{OPR} varies in 1.5−3 for NGC 7023.

By using the method described in Chrysostomou et al. (1993), we derive the R_{OP} ratio. Table 8 and Figure 28 show the variation of R_{OPR} as a function of the upper level energy. Figure 28 shows the R_{OP} values of the regions A, B, and C. The average of R_{OP} is 1.59 ± 0.48, 1.62 ± 0.28, and 1.56 ± 0.37 of regions A, B, and C, respectively.

Our derived R_{OP} values are consistent with previous studies from typical fluorescent sources, different from that of Martini et al. (1997) who presented the R_{OP} value of 2.5 ± 0.3 for the northern filament of NGC 7023. In the calculation of Martini et al. (1997),

they only use one pair of the vibrational level ν=1 and J=3−4. In our calculations, we have more lines to derive R_{OP} more accurately.

In addition, Figure 28 and Table 9 show that the R_{OP} values depend on the upper level energy. In case of the low upper energy level, $E_u/k < 25000$ K, the derived values of R_{OP} are decreased from the region A to the region C. On the other hand, when the upper energy level is high, $E_u/k > 25000$ K, the ratios are similar for all regions. When the H_2 molecules are excited by FUV field and jump into the excited electronic states, they cascade back to the ground electronic state with various ro-vibration levels. At low $E_u/k < 25000$ K, the spin exchange collisions of H_2 with other species as atomic H and H^+ occur dominantly. Through the processes of spin exchange collisions, the R_{OP} tends to approach to 3. This process explains that R_{OP} at $E_u/k < 25000$ K is increased as density increases. At the higher upper energy level, $E_u/k > 25000$ K, the spin exchange collisions do not affect R_{OP} (Chrysostomou et al., 1998).

Table 8: Ortho-to-Para ratio as a function of vibrational level

Upper energy level [K][a]	Ortho H_2	Para H_2	R_{OP} region A[b]	R_{OP} region B	R_{OP} region C
6310	1-0 Q(1)	1-0 Q(2)	2.23(0.09)	1.78(0.09)	1.72(0.13)
6310	1-0 Q(1)	1-0 S(0)	2.47(0.10)	2.14(0.11)	1.91(0.14)
6711	1-0 S(1)	1-0 Q(2)	2.23(0.06)	1.78(0.06)	1.72(0.09)
7268	1-0 S(1)	1-0 S(2)	1.34(0.06)	1.30(0.07)	1.19(0.09)
7268	1-0 S(1)	1-0 Q(4)	1.20(0.14)	0.93(0.11)	0.53(0.08)
12322	2-1 S(1)	2-1 S(0)	1.54(0.16)	1.59(0.19)	1.45(0.24)
12850	2-1 S(1)	2-1 S(2)	2.07(0.08)	...	...
12992	2-1 S(3)	2-1 S(0)	...	1.59(0.16)	...
13520	2-1 S(3)	2-1 S(2)	2.07(0.07)	...	...
18102	3-1 O(5)	3-2 S(2)	1.72(0.10)	1.75(0.11)	1.86(0.19)

Upper energy level [K][a]	Ortho H_2	Para H_2	R_{OP} region A[b]	R_{OP} region B	R_{OP} region C
18736	3-1 O(7)	3-2 S(2)	...	1.75(0.04)	1.86(0.04)
22216	4-2 O(3)	4-2 O(4)	1.84(0.18)		1.61(0.24)
22556	4-2 O(5)	4-2 O(4)	1.85(0.10)	1.63(0.09)	...
26670	5-3 O(3)	5-3 O(2)	1.70(0.17)	1.86(0.20)	...
27745	5-3 Q(5)	5-3 O(4)	...	...	1.52(0.09)
28188	5-3 Q(5)	5-3 Q(4)	1.62(0.16)	...	1.83(0.23)
27183	5-3 O(5)	5-3 O(4)	2.16(0.13)	...	...
27626	5-3 O(5)	5-3 Q(4)	1.66(0.22)	...	...
31002	6-4 Q(1)	6-4 O(2)	1.41(0.14)	1.73(0.20)	...
31183	6-4 Q(1)	6-4 Q(2)	1.00(0.09)	1.44(0.16)	...
31482	6-4 Q(3)	6-4 Q(2)	1.00(0.06)	1.44(0.12)	1.32(0.20)
35169	7-5 Q(1)	7-5 Q(2)	0.81(0.08)	...	...
35169	7-5 Q(1)	7-5 Q(2)	0.81(0.08)	...	...
35447	7-5 O(5)	7-5 Q(2)	0.81(0.04)	...	...
39421	8-6 S(1)	8-6 O(6)	2.83(0.93)	...	...
39869	8-6 S(3)	8-6 O(6)	1.48(0.33)	...	...

[a]The average value of the upper energy level of ortho and para H_2.

[b]Uncertainties are written in parentheses.

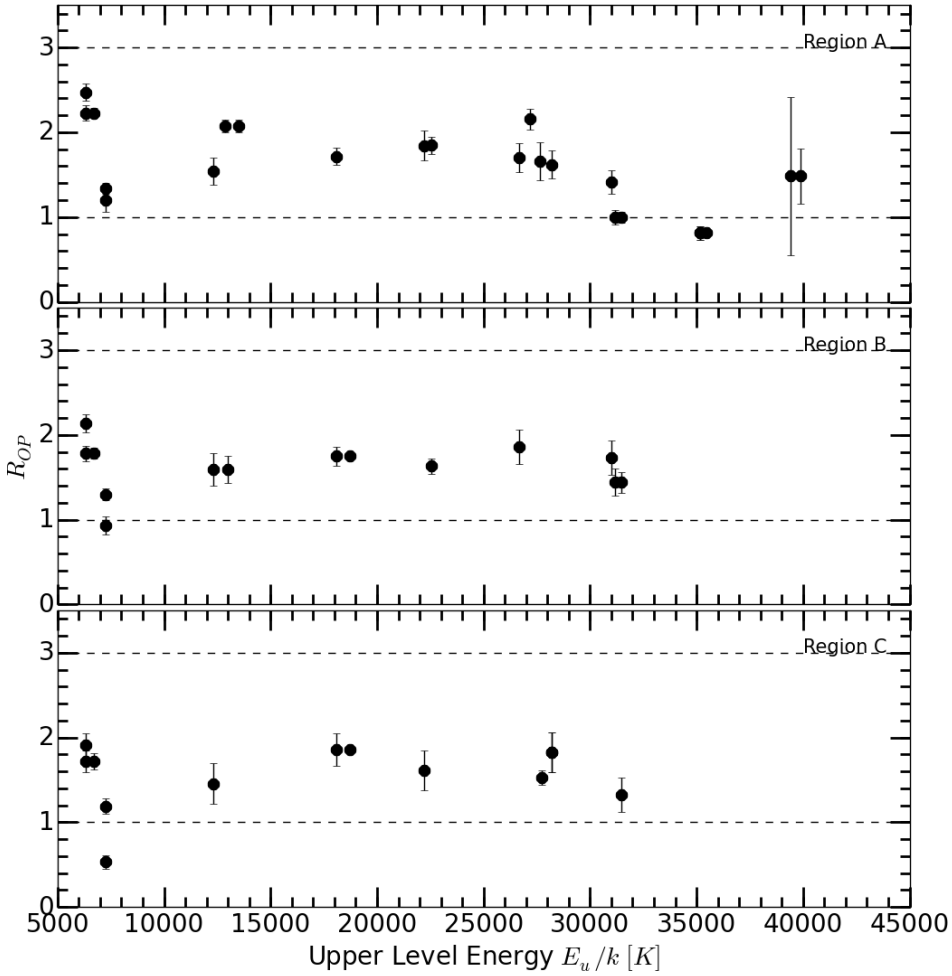

Fig. 28: Plots of orthor-to-para ratio (OPR) as a function of vibrational levels of regions A, B, and C.

Table 9: Ortho-to-Para ratio for regions of A, B, and C

R_{OP}	Region A	Region B	Region C
$5000 < E_u/k < 50000$	1.59±0.48	1.62±0.28	1.57±0.37
$E_u/k < 25000$	1.87±0.38	1.62±0.32	1.53±0.44
$E_u/k > 25000$	1.33±0.42	1.62±0.16	1.62±0.19

4.5.4 Comparison of the H_2 spectra to Photodissociation Models

Comparison of 2-1 S(1)/1-0 S(1) ratio to a PDR model

To investigate the physical condition of the observed region, we now compare the observed emission lines to PDR models in the literatures. Sternberg & Dalgarno (1989) (hereafter SD89) predicts H_2 emission lines in NIR in a wide range of gas density and incident UV field strength. We use our observed line ratio of 2-1 S(1)/1-0 S(1) to estimate the gas density. Figures 11 and 12 in ST89 provides that this line ratio is insensitive to the incident UV field strength. If the UV field strength is larger than 10^2 Habing units ($G_0 = 1.6 \times 10^{-3}$ erg cm^{-2} s^{-1}, Habing, 1968), the ratio only vary as a function of hydrogen gas density $n_T = n_H + n_{H_2}$. Table 10 shows estimated hydrogen density from the comparison of the 2-1 S(1)/1-0 S(1) ratio to that of the model predictions. We find that the hydrogen density in regions of A, B, and C are $10^{4.40}$ cm^{-3}, $10^{4.33}$ cm^{-3}, and $10^{4.30}$ cm^{-3}, respectively. The UV field strength in the north filament of NGC 7023 is in a range of 10^{3-4} G_0 (Chokshi et al., 1988;Fuente et al., 1999). Those estimate densities indicate that the observed H_2 emission lines are in the region which is dense and warm PDR. We see that the densities in regions A, B, and C are different.

We have adopted a visual extinction of $A_V = 2.2$ mag, derived from Mathis (1990) and Witt & Cottrell (1980) to correct the line ratios. This value is the stellar extinction value, and the nebulae extinction value maybe different from that. Martini et al. (1997, 1999) discussed that this variation of this assuming extinction value by a factor of 2 does not affect to their results. We also test to change the assuming extinction value of A_V by $\Delta A_V = \pm 2$ mag. Table 11 shows the ratios of 2-1 S(1)/1-0 S(1), corrected with different A_V values. This test shows that the variations of this extinction value of A_V do not have significant effects to our calculations.

Table 10: Gas density from the comparison with model of Sternberg & Dalgarno (1989)

Region	2-1 S(1)/1-0 S(1)	Temperature T_{12}[a] [K]	$n_T = n_H + n_{H_2}$ [cm^{-3}]	UV field strength [Habing]
A	0.39±0.01	(4.5±1.1) × 10^3	$10^{4.40\pm0.10}$	10^{3-4}
B	0.49±0.02	(5.5±1.3) × 10^3	$10^{4.33\pm0.10}$	10^{3-4}
C	0.54±0.03	(6.1±1.4) × 10^3	$10^{4.30\pm0.10}$	10^{3-4}

[a]The derived temperature from the line ratio 2-1 S(1)/1-0 S(1).

Table 11: The line ratio 2-1 S(1)/1-0 S(1) for regions A, B, and C with different A_V by $\Delta A_V = \pm 2$ mag

A_V	Region A	Region B	Region C
0.2	0.401±0.011	0.497±0.017	0.553±0.027
1.2	0.397±0.011	0.492±0.017	0.548±0.027
2.2	0.394±0.011	0.488±0.017	0.542±0.027
3.2	0.390±0.011	0.483±0.017	0.537±0.027
4.2	0.386±0.011	0.478±0.017	0.532±0.027

Comparison of the H_2 spectra to a PDR model

Obtaining of plentiful H_2 emission lines allows us to compare in detail the observed line strengths with that of the PDR models. We compare the line ratios of all observed H_2 emission lines to that of the PDR model of Draine & Bertoldi (1996) (hereafrer DB96). DB96 provides H_2 emission lines at density in range of 10^2−10^6 cm^{-3} and UV field intensity of 1−10^4 G_0. The observed line strengths are corrected for extinction value as discussed in Section 4.5.4.

The best fits are determined from the minimum chi-square value of the differences between the line ratio of the model and the data. Table 12 shows the derived chi-square values between the observed data and the models. The best fits are found at $n_H = 10^{4.79}$ cm^{-3} for region A and $10^{3.58}$ cm^{-3} for region B. In the case of region C, the best fit is found at $10^{3.45}$ cm^{-3}. Figure 29 shows how we derive the densities from the minimum chi-square values.

The estimated densities by using all line ratios from the PDR model of DB96 are consistent from that of the comparison from SD89 in region A. For region B and C, the different estimate densities between both models is $\sim$ 1 dex. In case of the estimation of densities by the model of SD89, the determined densities are based only on line ratio of 2-1 S(1)/1-0 S(1), while we have more line ratios for DB96 models.

Turn to the variations of the density of regions A, B, and C. We see here the different density structures within the slit-length observation of $15''$. The gas density is high in region A and reduce toward region B and C. Figure 30 shows the density profiles of regions A, B, and C which are estimated from ST89 and DB96. By this different density structures, we may see here clumps with high density of $n_H \sim 10^5$ cm^{-3}, embedded in lower density regions of $n_H = 10^3$−10^4 cm^{-3}. Based on the variations of the density profile, we see that the size of a clump is $\sim$ 0.01 pc.

Table 12: Gas density from the comparison of line ratios with the PDR model of Draine & Bertoldi (1996)

Model	n_H [cm^{-3}]	UV field strength [Habing]	χ^{2a}	χ^{2b}	χ^{2c}
aw3o	10^2	1	154	34	23
bw3d	10^2	10	184	42	26
Bw3o	10^3	10	104	21	18
Cw3o	10^3	10^2	109	22	18
Gw3o	10^4	10^2	52	11	14
Hw3o	10^4	10^3	50	12	15
Lw3o	10^5	10^3	36	28	22
Mw3o	10^5	10^4	62	44	30
Qw3o	10^6	10^4	73	74	49

[a]chi-square χ^2 of region A.

[b]chi-square χ^2 of region B.

[c]chi-square χ^2 of region C.

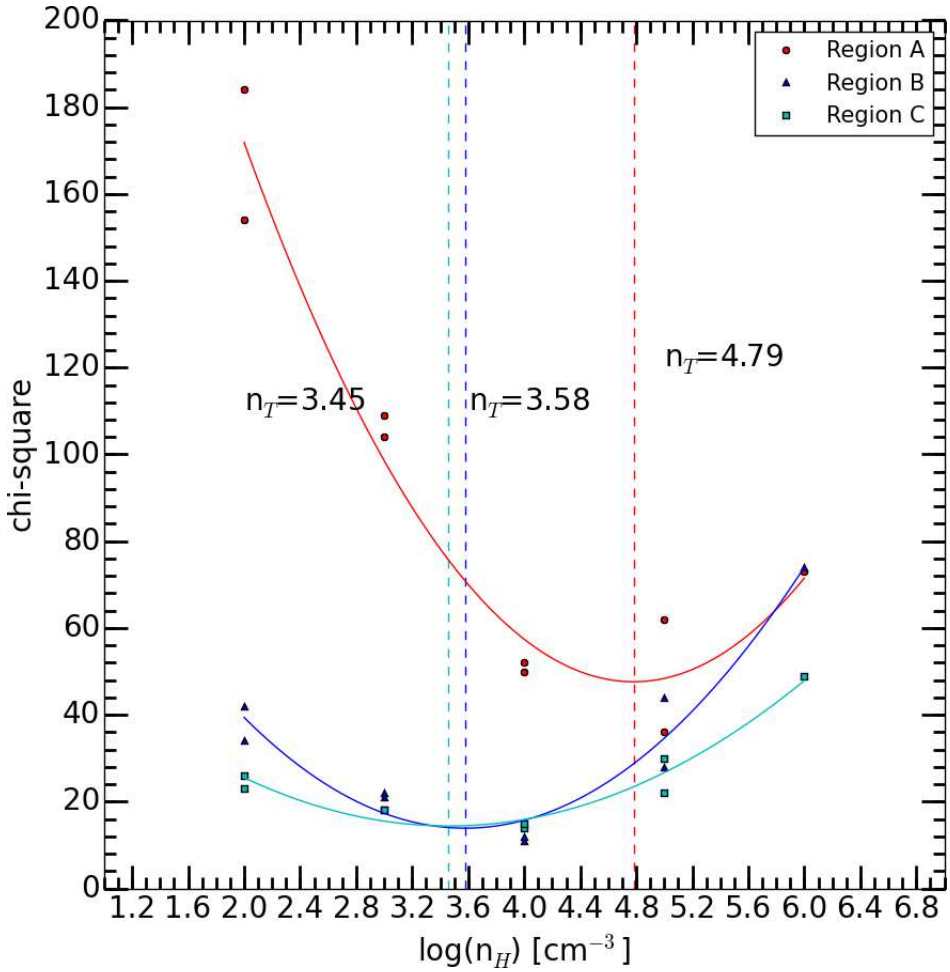

Fig. 29: The estimate densities of regions A (Red), B (Blue), and C (Cyan) from DB96. The solid lines display the fitting of chi-square values of regions A, B, and C. The dash lines show the minimum chi-square values from the fitting.

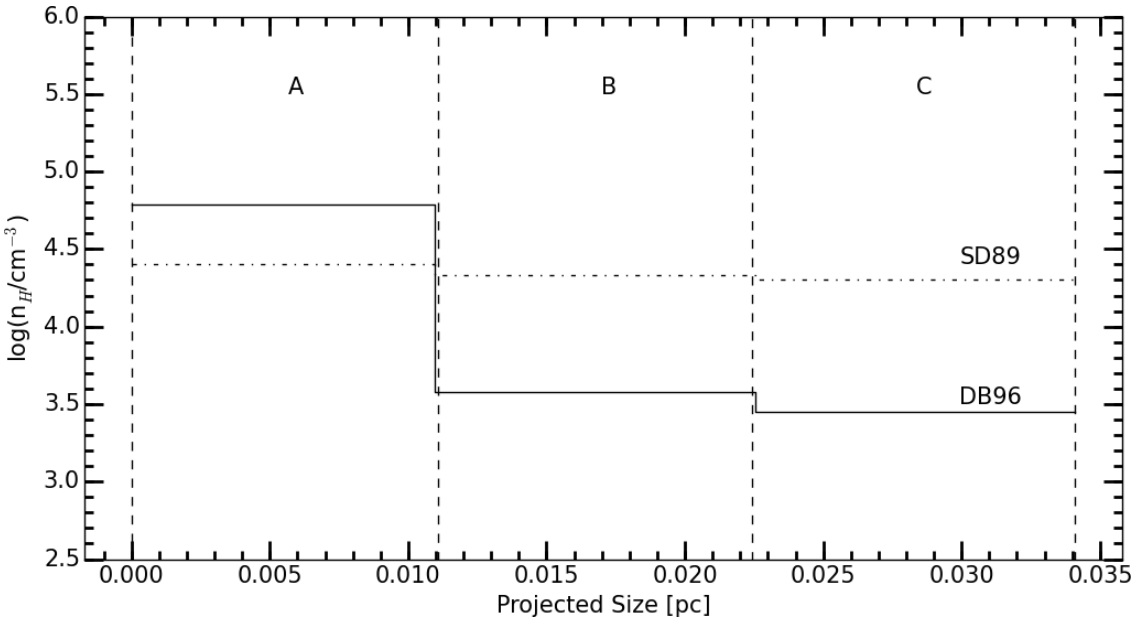

Fig. 30: The estimate densities of regions A, B, and C from the PDR models of SD89 and DB96. The solid line displays the estimate densities by DB96. The dash-dot line shows the determined densities by SD89.

4.6 Conclusions

The H_2 level column density distribution of regions A, B, and C has been calculated. The distributions of the excitation diagrams show that most of the observed H_2 emission lines are UV excited from FUV photons. In addition, the calculations of the diagnostic ratio of 2-1 S(1)/1-0 S(1) are 0.39−0.54 for regions A, B, and C. The ratios indicate that the fluorescent excitation are dominant in regions B and C, while the excitation mechanism in region A is partially thermalized.

The derived R_{OP} is 1.57−1.62. The R_{OP} lower than 3 indicate that the observed H_2 lines are mostly UV excited. We see the variation of R_{OP} in the observed regions A, B, and C as a function of the upper energy level. At the low upper energy level, $E_u/k <$ 25000 K, the density affects to the variations of R_{OP}. At higher upper energy level, E_u/k $>$ 25000 K, the determined R_{OP} values are same for regions A, B, and C. Those derived values are consistent with previous determinations.

The comparisons of the observed H_2 emission lines to the PDR models suggest the variations in density distribution in the NW filament of NGC 7023. These are high density clumps, $n_H \sim 10^5$ cm^{-3} embedded in lower density regions $n_H = 10^3$−10^4 cm^{-3}. Our estimated densities are consistent with other determines in the literatures. By using low resolution NIR H_2 emission lines, Martini et al. (1997, 1999) found that the NW filament of NGC 7023 has high density clump of $n_H \sim 10^6$ cm^{-3} in a diffuse filament with density of 10^4−10^5 cm^{-3}. By using radio emission lines from ISO observations, Fuente et al. (2000) found that the NW has high density filament of $n_H \sim 10^6$ cm^{-3} immersed in a diffuse interfilament of $n_H \sim 10^4$ cm^{-3}. Kohler et al. (2014) estimated the density values for the NW of $n_H = 10^4$−10^6 cm^{-3} by using CO emission from Spitzer observations.

We see here the variation density distribution within small scale observation of $15''$. The large changes in densities from region A to region B and C may indicate clumpy structure in this region. We may see here a high density clump or a part of clump.

The estimate size of this clump may be $\sim$ 0.01 pc. This density variation within small scale structure has important connections to the star-formation process. The increases of density within small scale may indicate the evidence of local turbulence in the region.

For future works, we may need to divide the observed region within $15''$ to higher spatial scale to see in detail the density distribution in the region. Then we can inspect more the size of the clump by the more detailed variation of the density distribution. We suggest future observations with more extended regions in this NW filament of NGC 7023 to investigate the density distributions and clumpy size structures. In the current state, we compare our data with the PDR model of DB96 (Draine & Bertoldi, 1996). A comparison with Cloudy model may also necessary to do to confirm the derived gas densities and UV field strength in the region.

Bibliography

Allers, K. N., Jaffe, D. T. & Lacy, J. H. 2005, ApJ, 630, 368

An, J. H. & Sellgren, K. 2003, ApJ, 599, 312

Alecian, E., Catala, C., Wade, G. A., et al. 2008, MNRAS, 385, 391

Alecian E., Wade, G. A., Catala, C. et al., 2013, MNRAS, 429, 1001

Baschek, B., Beltrametti, M., Kóppen, J., & Traving, G. 1982, A & A, 105, 300

Bertoldi, F., Timmermann, R., Rosenthal, D., Drapatz, S., & Wright, C. M. 1999, A & A, 346, 267

Black, J. H., & Van Dishoeck, E. F. 1987, Flourescent Excitation of Interstellar H_2, ApJ, 322, 412

Burton, M. G., Brand, P. W. J. L., Geballe, T. R., & Webster, A. S. 1989, MNRAS, 236, 409

Burton, M. G., Hollenbach, D. J., & Tielens, A. G. G. M. 1990, ApJ, 365, 620

Burton, M. G. 1992, Australian J. Phys., 45, 463

Burton, M. G., Howe, J. E., Geballe, T. R., & Brand, J. L. 1998, PASA, 15, 194

Chrysostomou, A., Brand, P. W. J. L., Burton, M. G., & Moorhouse, A. 1992, MRAS, 256, 528

Chrysostomou, A., Brand, P. W. J. L., Burton, M. G., & Moorhouse, A. 1993, MRAS, 265, 329

Chrysostomou A., Brand P. W. J. L., Ramsay-Howat S. K. R., Burton M. G. 1998, in Yuh J. L, Liseau R., eds, ASP Conf. Ser., Star Formation with ISO. Astron. Soc. Pac., San Francisco, p. 326

Chokshi, A., Tielens, A. G. G. M., Werner, M. W., & Castelaz, M. W. 1988, ApJ, 334, 803

Cox, A. N. 2011, Allens Astrophysical Quantities (4th ed.; New York:Springer)

Draine, B. T. & Bertoldi, F. 1996, ApJ, 468, 269

Evens, N. J. II. 1999, ARA&A, 37, 311

Ferland, G. J., Korista, K. T., Verner, D. A., Ferguson, J. W., Kingdon, J. B., & Verner, E. M. 1998, PASP, 110, 761

Fleming, B., France, K., Lupu, R. E., & McCandliss, S. R. 2010, ApJ, 725, 159

Fuente, A., Martín-Pintado, J., Cernicharo, J., & Bachiller, R. 1993, A & A, 276, 473

Fuente, A., Martín-Pintado, J., Neri, R., Rogers, C., & Moriarty-Schieven, G. 1996, A & A, 310, 286

Fuente, A., Martín-Pintado, J., Rodriguez-Fernandez, N. J., et al. 1999, ApJ, 518, L45

Fuente, A., Martín-Pintado, J., Cernicharo, J., & Gerin, M. 2000, A & A, 354, 1053

Gatley, I., et al. 1987, ApJ, 318, L73

Habing, H. J. 1968, Bull. Astron. Inst. Netherlands, 19, 421

Habart, E., Boulanger, F., Verstraete, L., Walmsley, C. M., & Pineau des Forêts, G. 2004, A & A, 414, 531

Habart, E., Abergel, A., Boulanger, F. et al. 2011, A & A, 527, A122

Hasegawa, T., Gatley, I., Garden, R. P., Brand, W. J. L., Ohisi, M., Hayashi, M., & Kaifu, N. 1987, ApJ, 318, 77

Hayashi, M., Hasegawa, T., Gatley, I. et al. 1985, MNRAS, 215, 31P

Hollenbach, D. J., & Tielens, A. G. G. M. 1999, Rev. Mod. Phys., 71, 173

Hora, J. L., & Latter, W. B. 1996, ApJ, 461, 288

Köhler, M. , Habart, E., Arab, H. et al. 2014, A & A, 569, 109

Le, H. A. N., Pak, S., Myungshin, I. et al. 2014, JASR, 54, 6

Le, H. A. N., Pak, S., Jaffe, D. T. et al. 2015, JASR, 55, 11

Lee, H. I. et al. 2015, in preparation

Lee, S., Pak, S., Lee, S-. G. et al. 2005, MNRAS, 361, 1273

Lee, S. & Pak, S. 2006, JKAS, 39, 151

Lemaire, J. L., Field, D., Gerin, M., Leach, S., Pinneau des Forets, G., Falgarone, E., Rostas, F., & Rouan, D. 1996, A & A, 308, 895

Lemaire, J. L., Field, D., Maillard, J. P., Pinneau des Forets, G., Falgarone, E., Pijpers, F. P., Gerin, M., & Rostas, F. 1999, A & A, 349, 253

Luhman, M. L., & Jaffe, D. T. 1996, ApJ, 463, 191

Luhman, K. L. & Rieke, G. H. 1996, ApJ, 461, 298

Luhman, K. L., Engelbracht, C. W., & Luhman, M. L. 1998, ApJ, 499, 799

Luhman, M. L., Jaffe, D. T., Sternberg, A., Herrmann, F., & Poglitsch, A. 1997, ApJ, 482, 298

Marquez-Lugo, R. A., Guerrero, M. A., Ramos-Larios, G. & Miranda, L. F. 2015, MNRAS, 453, 1888

Martini, P., Sellgren, K., & Hora, J. L. 1997, ApJ, 484, 296

Martini, P., Sellgren, K. & Depoy D. L. 1999, ApJ, 526, 772

Mathis, J. S. 1990, ARA&A, 28, 37

McCartney, M. S. K., Brand, P. W. J. L., Burton, M. G., & Chrysostomou, A. 1999, MNRAS, 307, 315

Pak S., Jaffe, D. T., van Dishoeck E. F., Johansson L. E. B., Booth R. S. 1998, ApJ, 498, 735

Pak S., Jaffe, D. T., Stacey G. J., Bradford C. M., Klumpe E. W., Keller L. D. 2004, ApJ, 609, 692

Park, C., Jaffe, D. T., Yuk, I.-S. et al. 2014, Proc SPIE, 9147, 91471D-1

Pilleri, P., Montillaud, J., Berne, O., & Joblin, C. 2012, A & A, 542, 69

Pilleri, P., Joblin, C., Boulanger, F., & Onaka, T. 2012, A & A, 577, A16

Ramsay, S. K., Chrysostomou, A., Geballe, T. R., Brand, P. W. J. L., & Mountain, M. 1993, MNRAS, 263, 695

Rieke, G. H., & Lebofsky, M. J. 1985, ApJ, 288, 618

Rosenthal, D., Bertoldi, F. & Drapatz, S. 2000, A & A, 356, 705

Sellgren, K. 1986, ApJ, 305, 399

Sellgren, K., Werner, M. W., & Dinerstein, H. L. 1992, ApJ, 400, 238

Shaw, G., Ferland, G. J., Abel, N. P., Stancil, P. C., & van Hoof, P. A. M. 2004, ApJ, 624, 794

Shaw, G., Ferland, G. J., Henney,W. J., Stancil, P. C., Abel, N. P., Pellegrini, E. W., Baldwin, J. A., & van Hoof, P. A. M. 2009, ApJ, 701, 677

Sheffer, Y., Wolfire, M. G., Hollenbach, D. J., Kaufman, M. J., & Cordier, M. 2011, ApJ, 741, 45

Sheffer, Y. & Wolfire, M. G. 2013, ApJ, 774, L14

Sim, C. K., Le, H. A. N., Pak, S. et al. 2014, JASR, 53, 11

Sternberg, A. & Dalgarno, A. 1989, ApJ, 338, 197

Sternberg, A., & Neufeld, D. A. 1999, ApJ, 516, 371

Takami, M., Usada, T., Sugai, H., Kawabata, H., Suto, H., & Tanaka, M. 2000, ApJ, 529, 268

Tanaka, M., Hasegawa, T., Hayashi, S. S., Brand, P. W. J. L., & Gatley, I. 1989, ApJ, 336, 207

Tielens, A. G. G. M., & Hollenbach, D. J. 1985a, ApJ, 291, 772

Tielens, A. G. G. M., & Hollenbach, D. J. 1985b, ApJ, 291, 747

Tokunaga, A. T. 2000, Allen's astrophysical quantities, ed. Cox, A. N. et al. (4th ed.; New York: AIP press), 143

van den Ancker, M. E., Thé, P. S., Tjin A Djie, H. R. E., Catala, C., de Winter, D., Blondel, P. F. C., & Waters, L. B. F. M. 1997, A & A, 324, L33

Watt, G. D., Burton,W. B., Choe, S.-U., & Liszt, H. S. 1986, A & A, 163, 194

Witt, A. N., Gordon, K. D., Vijh, U. P., et al. 2006, ApJ, 636, 303

Witt, A. N., & Cottrell, M. J. 1980, ApJ, 235, 899

Yuk, I.-S., Jaffe, D. T., Barns, S. et al. 2010, Proc SPIE, 7735, 77351M-9

Appendix A

List of Publications

References

[1] Le, H. A. N., Kang, W., Pak, S., Im, M. et al. 2011, Medium Resolution Spectral Library of Late-Type Stellar Templates in Near-Infrared Band, JKAS, 44, 125.

[2] Le, H. A. N., Pak, S., Im, M., Kim, M., Sim, C. K., & Ho, L. C. 2014, Medium Resolution Near-Infrared Spectra of the Host Galaxies of Nearby Quasars, JASR, 54, 6.

[3] Le, H. A. N., Pak, S., Jaffe, D. T., Kaplan, K., Lee, J. J., Im, M., & Seifahrt. 2015, Exposure Time Calculator for Immersion Grating Infrared Spectrograph: IGRINS, JASR, 55, 11.

[4] Le, H. A. N., Pak, S., Jaffe, D. T. et al. 2016, High-Resolution Spectroscopy of NGC 7023, in preparation.

[5] Oh, H., Pyo, T. -S., Yuk, I. -S., Park, B. -G. , Park, C., Chun, M. -Y., Pak, S., Kim, K. -M. , Oh, J. S., Jeong, U., Yu, Y. S., Lee, J. -J., Kim, H., Hwang, N., Kaplan, K., Pavel, M., Mace, G., Lee, H. -I., Le, H. A. N., Lee, S., & Jaffe, D. T. 2016, ApJ, in press.

[6] Park, C., Jaffe, D. T., Yuk, I.-S., Chun, M.-Y., Pak, S., Kim, K.-M., Pavel, M., Lee, H., Oh, H., Jeong, U., Sim, C. K., Lee, H.-I., Le, H. A. N., Strubhard, J., Gully-Santiago,

M., Oh, J. S., Cha, S.-M., Moon, B., Park, K., Brooks, C., Ko, K., Han, J.-Y., Nah, J., Hill, P. C., Lee, S., Barnes, S., Yu, Y. S., Kaplan, K., Mace, G., Kim, H., Lee, J.-J., Hwang, N., Park, B.-G. in the Proc. of Ground-based and Airborne Instrumentation for Astronomy V, Eds., S. K. Ramsay, I. S. McLean, H. Takami, SPIE, 9147, 91471D-1/12

[7] Park, W., Pak, S., Shim, H., Le, H. A. N., Im, M., Chang, S., Yu, J. 2015, Photometric transformation from RGB Bayer filter system to Johnson-Cousins BVR filter system, JASR, 57, 1.

[8] Sim, C. K., Le, H. A. N., Pak, S. et al. 2014, Comprehensive data reduction package for the Immersion GRating INfrared Spectrograph: IGRINS, JASR, 53, 11.

Lời Cảm Ơn

Tất cả những gì gặt hái được ngày hôm nay đối với tôi thực sự không dể dàng. Yêu thích thiên văn học là một thách thức lớn đối với tôi. Thiên văn cho tôi lý tưởng của cuộc sống nhưng cũng mang lại rất nhiều vất vã.

Khi tôi còn học cấp ba, những ngày tháng đi chợ vào sáng sớm tinh mơ đã mang cho tôi tình yêu thiên văn học. Ngấm nhìn các vì sao vào buổi sáng sớm là điều vô cùng kì diệu. Các vì sao đẹp đến lạ thường. Sao Kim lấp lánh trên bầu trời mổi sớm mai với vẽ đẹp đầy thách thức khiến con người như khát khao muốn vươn tới. Một cô bé như tôi ở tuổi mới lớn cũng đầy mong ước và khát khao để chạm tới những vì sao. Rồi tôi chọn Vật lý khi học đại học vì Việt Nam không có ngành thiên văn học lúc đó. Trong những năm tháng học đại học tôi luôn mong ước một điều đó là có thể thực sự được học về thiên văn. Được đến đài thiên văn và được quan sát bầu trời.

Rồi sau đó tôi được đến Korea. Cuộc đời tôi thực sự bước sang trang mới. Thầy Soojong Pak đóng vai trò rất quan trọng trong cuộc sống của tôi. Thầy đã biến ước mơ của tôi thành sự thật. Tôi được học về thiên văn học, được đến đài quan sát. Và thực sự tôi đã chạm tới những vì sao. Tôi làm việc gì cũng khó khăn. Và tôi thầm cảm ơn thầy Soojong đã luôn thông cảm và khoan dung giúp đở tôi. Để tôi có thể gặt hái được những thành quả như ngày hôm nay.

Cám ơn ba mẹ đã để con chọn con đường con đi ngày hôm nay. Cám ơn ba mẹ đã luôn động viên và giúp đỡ con trong việc học và đã luôn cầu nguyện cho con những lúc khó khăn nhất.

Cám ơn Thùy Dung đã luôn bên cạnh và giúp đỡ chị những năm tháng học ở Korea. Em vừa là người em, vừa là người bạn tri kỷ.

Cuối cùng tôi hiểu một đều rằng: chúng ta có ước mơ, và hãy gìn giữ ước mơ. Đôi khi tưỡng chừng như những khó khăn đã có thể đánh gục tôi. Nhưng những lúc khó khăn nhất, là lúc năng lực con người trỗi dậy nhiều nhất … Và chúng ta sẽ vượt qua nếu như chúng ta vẫn còn “hi vọng”. Cũng như câu nói của nhà nữ khoa học Marie Curie:

“Cuộc sống không dể dàng đối với mỗi chúng ta. Nhưng không sao hãy tin ở chính mình. Hãy tin rằng chúng ta có một năng khiếu nào đó và quyết đạt đến cho bằng được. Có thể là mọi việc sẽ trơn tru ngay khi ta ít ngờ đến nhất.”

Korea, 2016.01.07

Lê Nguyễn Huỳnh Anh